



저작자표시-비영리-변경금지 2.0 대한민국

이용자는 아래의 조건을 따르는 경우에 한하여 자유롭게

- 이 저작물을 복제, 배포, 전송, 전시, 공연 및 방송할 수 있습니다.

다음과 같은 조건을 따라야 합니다:



저작자표시. 귀하는 원저작자를 표시하여야 합니다.



비영리. 귀하는 이 저작물을 영리 목적으로 이용할 수 없습니다.



변경금지. 귀하는 이 저작물을 개작, 변형 또는 가공할 수 없습니다.

- 귀하는, 이 저작물의 재이용이나 배포의 경우, 이 저작물에 적용된 이용허락조건을 명확하게 나타내어야 합니다.
- 저작권자로부터 별도의 허가를 받으면 이러한 조건들은 적용되지 않습니다.

저작권법에 따른 이용자의 권리는 위의 내용에 의하여 영향을 받지 않습니다.

이것은 [이용허락규약\(Legal Code\)](#)을 이해하기 쉽게 요약한 것입니다.

[Disclaimer](#)

**Ph.D. DISSERTATION**

***Ab initio* Study on  
the Atomic Configuration-dependent  
Electronic Properties of Pseudobinary systems**

**by  
Gyuseung Han**

**August 2021**

**DEPARTMENT OF MATERIALS SCIENCE AND ENGINEERING**

**COLLEGE OF ENGINEERING**

**SEOUL NATIONAL UNIVERSITY**

***Ab initio* Study on  
the Atomic Configuration-dependent  
Electronic Properties of Pseudobinary systems**

**Advisor : Prof. Cheol Seong Hwang**

**by  
Gyuseung Han**

A thesis submitted to the Graduate Faculty  
of Seoul National University in partial fulfillment of the requirements  
for the Degree of Doctor of Philosophy  
Department of Materials Science and Engineering

**August 2021**

**Approved  
by**

**Chairman of Advisory Committee : Miyoung Kim**

**Vice-chairman of Advisory Committee : Cheol Seong Hwang**

**Advisory Committee : Seungwu Han**

**Advisory Committee : Jung-Hae Choi**

**Advisory Committee : Sangtae Kim**

# ABSTRACT

---

The pseudobinary systems have been widely used to obtain the desired properties. The property tuning has been usually conducted by controlling the composition for solid solution state. Recently, the methods to control the configuration have been developed, and thus it is attractive to investigate the pseudobinary system in the scope of configuration because many properties such as energy, bandgap, and dielectric constant vary according to the configuration. In this dissertation, configuration- and composition-dependent properties of the candidate materials to be used in transistor such as Ga(As,Sb), (In,Ga)As and (Be,Mg)O are theoretically investigated in terms of configuration.

However, it is hard to theoretically investigate pseudobinary systems, especially the solid solutions, because of its enormous number of configurations, which is called configurational problem. To overcome the configurational problem, this dissertation proposes the efficient and accurate framework to calculate the properties of solid solution systems: (i) calculating the properties including energy of numerous configurations using density functional theory (DFT); (ii) making cluster expansion models for the each property based on DFT results to explore a wide range of composition and configuration space outside DFT

capability; (iii) calculating average property using the statistical thermodynamics, in which a system is consist of the large number of microstates. In the statistical thermodynamics part, the grand canonical ensemble is used to simulate more realistically, which allows the compositional fluctuation and continuous composition.

To ensure that the proposed methodology can be applied to other new materials, the methodology is validated by comparing the calculated phase diagrams of Ga(As,Sb) and (In,Ga)As, and the calculated average bandgap of Ga(As,Sb) with experimental literature. In the process, it is found and proved mathematically that strain induced by lattice mismatch between microstates which comes from local compositional fluctuation, called local strain, is necessary to describe the phenomenon when using grand canonical ensemble. The calculated bandgaps of Ga(As,Sb) configurations show that the wider range of Ga(As,Sb) bandgap can be obtained by controlling both configuration and composition than by composition control alone. In addition, the negative proportional relationship between bandgap and energy is found for Ga(As,Sb) and expected for several pseudobinary systems from effective cluster interaction coefficient (ECI) in literature.

The calculation on (Be,Mg)O is performed to obtain high dielectric constant and high bandgap, as a new candidate for high-k materials. By DFT calculation for unitcell, (Be,Mg)O with Be atom

which is deviated in rocksalt structure, called modified-rocksalt structure (m-RS), become more stable than rocksalt structure. By DFT calculation for various configurations, it is found that the dielectric constant of m-RS (Be,Mg)O varies a lot according to the configuration while the bandgap keeps high value regardless of configuration. The large variation of (Be,Mg)O dielectric constant according to configuration becomes driving force for searching configurations with high dielectric constant rather than calculating the average dielectric constant. As a result, it is found that the configurations with superlattice-like structure, which can be deposited using ALD, have a high dielectric constant over 300 K, which can be explained by long apical Be-O bond length.

The method for simulating a pseudobinary system proposed in this dissertation can be utilized in predicting and controlling the properties of other pseudobinary systems. Confirming that the range of possible properties is broadened through controlling both composition and configuration will be a foundation for the study of pseudobinary system's properties.

---

**Keywords:** *ab initio* thermodynamics, configuration, Ga(As,Sb), (In,Ga)As, (Be,Mg)O, superlattice, phase diagram, bandgap, dielectric constant

**Student Number:** 2016-20842

# TABLE OF CONTENTS

---

Abstract .....	i
Table of Contents .....	iv
List of Figures .....	vii
List of Tables .....	xii
<b>CHAPTER 1 Introduction .....</b>	<b>1</b>
1.1 Overview of pseudobinary systems in electronic devices .....	1
1.2 Challenges in calculating pseudobinary systems.....	2
1.3 Outline of the dissertation .....	3
<b>CHAPTER 2 Theoretical Background .....</b>	<b>5</b>
2.1 Introduction.....	5
2.2 Density functional theory (DFT).....	6
2.3 Cluster expansion.....	8
2.4 Statistical thermodynamics .....	9
2.5 Dielectric constant.....	12

## **CHAPTER 3 Methodology for Average Property. 15**

3.1 Introduction .....	15
3.2 Density functional theory (DFT).....	16
3.3 Cluster expansion .....	21
3.4 Statistical thermodynamics .....	21
3.4.1 Ensemble average .....	21
3.4.2 Number of samples .....	23

## **CHAPTER 4 Phase diagram of III-V Semiconductor**

### **Solid Solution ..... 25**

4.1 Introduction .....	25
4.2 Computation details .....	29
4.3 Phase diagrams of Ga(As,Sb) and (In,Ga)As .....	31
4.4 Upper critical solution temperature.....	46
4.5 Conclusion.....	49
4.6 Appendix .....	50

## **CHAPTER 5 Bandgap of III-V Semiconductor Solid**

### **Solution ..... 55**

5.1 Introduction .....	55
------------------------	----

5.2 Computation details .....	57
5.3 Bandgaps and energies of configurations .....	60
5.4 Average bandgap of Ga(As,Sb).....	70
5.5 Conclusion.....	77
<b>CHAPTER 6 (Be,Mg)O Solid Solution .....</b>	<b>79</b>
6.1 Introduction .....	79
6.2 Computation details .....	82
6.3 Energetics and structure stability .....	84
6.4 Bandgap.....	91
6.5 Temperature-dependent dielectric constant .....	93
6.6 Conclusion.....	104
6.7 Appendix .....	105
Bibliography .....	107
Abstract in Korean .....	130

# LIST OF FIGURES

---

- Figure 3.1** Schematic of the grand canonical ensemble with (a) freely relaxed microstates, (b) microstates under strain induced by local compositional fluctuation at  $x = 0.5$ . The side length of the square refers to the lattice constant in each microstate. .... 17
- Figure 3.2** (a) Lattice constant of 236 configurations of  $(\text{GaAs})_x(\text{GaSb})_{1-x}$  and (b) lattice constant of 297 configurations of  $(\text{InAs})_x(\text{GaAs})_{1-x}$  in  $2 \times 2 \times 2$  supercell. The solid line follows the Vegard's rule. .... 20
- Figure 4.1** ECIs of (a)  $(\text{GaAs})_x(\text{GaSb})_{1-x}$  and (b)  $(\text{InAs})_x(\text{GaAs})_{1-x}$ . (c) Cluster corresponding to  $J_{k,m}^{\Delta E}$ . The set of numbers (k,m) denotes m-th k-site cluster. .... 32
- Figure 4.2** Strain energy induced by local compositional fluctuation as a function of the relative volume  $V/V_0$  for various compositions of (a)  $(\text{GaAs})_x(\text{GaSb})_{1-x}$  and (b)  $(\text{InAs})_x(\text{GaAs})_{1-x}$ . The black curves were fitted to the B-M EOS. .... 35
- Figure 4.3** Mixing energy of (a)  $(\text{GaAs})_x(\text{GaSb})_{1-x}$  and (b)  $(\text{InAs})_x(\text{GaAs})_{1-x}$ . The green bar symbol represents  $\Delta E\sigma$  calculated by the CE. The black bold line and red line correspond to  $\overline{\Delta E^{total}}$  calculated with and without considering the strain energy at 300, 600, and 900 K, respectively. .... 37
- Figure 4.4**  $P_{n/N}$  of (a)  $(\text{GaAs})_{0.5}(\text{GaSb})_{0.5}$  and (b)  $(\text{InAs})_{0.5}(\text{GaAs})_{0.5}$  at 300,

600 and 900 K. The dotted line represents  $n/N = x = 0.5$ . ..... 39

**Figure 4.5**  $\Delta F$  of (a)  $(\text{GaAs})_x(\text{GaSb})_{1-x}$  and (b)  $(\text{InAs})_x(\text{GaAs})_{1-x}$  at 300, 600, and 900 K calculated with strain energy (black line) and without strain energy (red line). ..... 42

**Figure 4.6** Phase diagrams of (a)  $(\text{GaAs})_x(\text{GaSb})_{1-x}$  and (b)  $(\text{InAs})_x(\text{GaAs})_{1-x}$ . The black solid and black dotted lines are the calculated binodal and spinodal curves. The gray area is above the experimental solidus line. The colored lines are the previous calculation results, while the colored symbols denote the previous experimental data. .... 45

**Figure 4.7** Experimental (a)  $a_0$ , (b)  $B_0$ , and (c)  $V_0 B_0$  of nine III–V zinc-blende structure materials. (d) Matrix diagram of  $T_c$ . The  $a_0$  ratio and  $B_0$  ratio are indicated using red and green scale bars, respectively. The  $T_c$  with an asterisk indicates that the  $T_c$  is above the solidus line. All data are obtained from the experimental literature, except  $T_c$  with a triangle. .... 47

**Figure 5.1** Calculated ECIs and corresponding clusters. ECIs of (a) bandgap, (b) mixing energy of  $\text{GaAs}_x\text{Sb}_{1-x}$ , and (c) corresponding clusters. The set of numbers (k,m) denotes m-th k-site cluster. .... 61

**Figure 5.2** Configuration-dependent bandgap. (a) Bandgap versus mixing energy graph. Crystal structure of (b) chalcopyrite and (c) CuPt. Each point represents a configuration, and the color of each point

denotes the composition  $x$ . The open black circles represent the results obtained by DFT calculations.  $2N$  is the total number of atoms in a  $2 \times 2 \times 2$  supercell. .... 64

**Figure 5.3**  $E_{g,\sigma}$  (upper panel) and  $\Delta E_{\sigma}$  (lower panel) of 10,000 configurations as a function of  $SRO_{(2,m)}$ .  $x_{\sigma} =$  (a) 0.25 (yellow), (b) 0.5 (green), and (c) 0.75 (blue) The shaded area indicates the forbidden range of  $SRO_{(2,m)}$ . .... 66

**Figure 5.4** Partial density of states (DOS) projected on atoms. (a) GaSb, (b) chalcopyrite structure, (c) CuPt structure, and (d) GaAs. Zero energy denotes the Fermi level. For CuPt structure, Ga1 indicates Ga atom having three bonds with As atoms and one bond with Sb atom, and Ga2 indicates Ga atom having one bond with As atom and three bonds with Sb atoms. .... 69

**Figure 5.5** Strain energy as a function of the relative volume  $V/V_0$ . The symbols denote the unit cell of  $GaAs_xSb_{1-x}$  with various relative volumes, and the black curve is fitted to the Birch-Murnaghan equation of state. .... 71

**Figure 5.6** Probability mass function (PMF) of  $x_{\sigma}$  and bandgap under strain. PMFs at 300, 600, and 900 K for (a)  $GaAs_{0.1}Sb_{0.9}$ , (b)  $GaAs_{0.5}Sb_{0.5}$ , and (c)  $GaAs_{0.9}Sb_{0.1}$ . (d) Sum of the PMFs in the shaded area where the deviation of  $x_{\sigma}$  from  $x$  is less than 0.1. (e) Bandgap of a hydrostatically strained unit cell with a local composition  $x_{\sigma} = 0, 0.25, 0.5, 0.75,$  and  $1$  as a function of  $x-x_{\sigma}$ . .... 74

- Figure 5.7** Bandgap of  $\text{GaAs}_x\text{Sb}_{1-x}$  as a function of composition  $x$ . Bar symbols represent the bandgap of each configuration calculated using the cluster expansion method. The solid line denotes the calculated average bandgap at various temperatures, and the dashed line denotes the conventional experimental bandgap. ... 76
- Figure 6.1**  $\kappa_{zz}$  (black filled square with solid line) and Be–O bond length (green open square with dotted line) of RS BeO with respect to the pressure. .... 86
- Figure 6.2** Atomic structures and phonon dispersion of the 8-atom cell of (a) WZ, (b) RS and (c) m-RS structures of  $\text{Be}_{0.25}\text{Mg}_{0.75}\text{O}$ . Be–O bond is indicated by the thick black line. .... 89
- Figure 6.3** Calculated  $\Delta E$  of WZ, RS, m-RS  $\text{Be}_x\text{Mg}_{1-x}\text{O}$  in 8-atom cell. . 97
- Figure 6.4** Calculated (a)  $\Delta E$  and (b)  $E_g$  of WZ and m-RS  $\text{Be}_x\text{Mg}_{1-x}\text{O}$  in 64-atom cells. .... 92
- Figure 6.5** (a) Side views of all possible configurations in  $1 \times 1 \times 2$  supercell composed of 16 atoms of m-RS  $\text{Be}_{0.25}\text{Mg}_{0.75}\text{O}$ . The last three configurations with a gray background have a negative frequency at  $\Gamma$ -point. (b)  $\kappa_{zz}$  vs. apical bond length (c)  $\kappa_{zz}$  vs.  $dE$ .  $dE$  is the relative energy of a certain configuration with respect to the lowest energy configuration (configuration #11). The symbols for configurations with superlattice-like structure are colored. .... 96
- Figure 6.6** Top view, side view, and phonon dispersion of  $\text{Be}_{0.25}\text{Mg}_{0.75}\text{O}$  in

2×2×2 supercell of (a) HZ, (b) HA, (c) R, (d) LZ, and (e) LA. (f) Be–O bond length and  $\kappa_{zz}$  for each configuration. Solid triangle indicates the apical bond length, while the open triangle indicates the equatorial bond length. .... 99

**Figure 6.7** Side views of the atomic configuration at 0 K and the average atomic position at 100, 200, 300, 400, 500, and 600 K calculated by AIMD calculations for (a) zigzag, (b) armchair and (c) rhombus-type. .... 101

**Figure 6.8** Temperature dependency of  $\kappa_{zz}$  for Be<sub>0.25</sub>Mg<sub>0.75</sub>O superlattices calculated using (a) phonon frequency extracted with phq, and (b) fluctuation method. .... 103

# LIST OF TABLES

---

<b>Table 5.1</b> Correlations between pairs of bandgap, energy, and $SRO_{(2,m)}$ of 10,000 configurations at $x_\sigma = 0.25, 0.5,$ and $0.75.$ .....	67
---	----

# CHAPTER 1

## INTRODUCTION

---

### 1.1 Overview of pseudobinary systems in electronic devices

One of the traditional method to obtain an innovative property is mixing the materials which has a notable advantage to adjust properties. Among the mixtures, a pseudobinary system refers a material which is a mixture of two materials, at least one of which is compound materials. There are various field that the pseudobinary systems are used, but this study focused on the materials in the electronic devices.

The metal-oxide-semiconductor field-effect transistor (MOSFET) is the most produced component in history [1]. Both semiconductor and dielectric in the first semiconductor devices were made of single crystals of elemental or compound materials. However, these materials could not provide the desired properties. Since the pseudobinary semiconductor materials  $\text{GaAs}_{1-x}\text{P}_x$  was

developed, many II-VI and III-V pseudobinary semiconductors have been developed for the materials in semiconductor devices, such as CMOS, HEMT, and so on. The pseudobinary systems for the dielectric materials have been studied to obtain desired value [2].

The properties of pseudobinary systems have been usually tuned by controlling the composition which is easy to control. However, the methods to control have been developed such as atomic layered deposition (ALD) [3,4], precipitation [5], and catalyst [6–8] even when the equilibrium state of the material is solid solution. Considering that many properties such as energy, bandgap, and dielectric constant depend on configuration, the configuration control will make it possible to obtain properties beyond the range of properties that can be obtained only through composition control.

## **1.2 Challenges in calculating pseudobinary systems**

Pseudobinary systems form the ordered structure or disordered structure, called solid solution, according to the composition and temperature. Because the solid solution does not have the translational symmetry, solid solution is defined in infinite cell and it is hard to simulate the solid solution using DFT.

There are some methods to simulate solid solution such as virtual crystal approximation (VCA) [9], coherent potential approximation (CPA) [10], Monte Carlo (MC) simulation, and multi-configurational supercell approach

[11]. Among the methods, the MC simulation and the multi-configurational supercell approach are based on statistical distribution of configurations in a system. The multi-configurational supercell approach considers the solid solution as the sum of the microstates, which is defined in relatively small cell, while the MC simulation uses sufficiently large cell to simulate solid solution. The multi-configurational supercell approach needs to calculate tremendous number of possible configurations, called configurational problem, and the large cell for MC simulation also requires a great amount of computational cost to simulate.

### **1.3 Outline of the dissertation**

The main topic of this dissertation is to examine various properties of the pseudobinary system. The dissertation is organized as follows. The first chapter is an introduction to the pseudobinary systems. Chapter 2 shows the theoretical backgrounds which are used in the dissertation. This chapter suggests the need to consider the strain energy induced by the compositional fluctuation, which is called local strain energy. Chapter 3 elucidates the methodology to calculate the properties of a pseudobinary system. Although the methodology in this chapter is mostly based on the theories in the chapter 2, it also contains explanations of additional theories to overcome challenges. Chapter 4 describe the phase diagrams of Ga(As,Sb) and (In,Ga)As obtained by analyzing the energies of configurations of the materials using the methodology presented in the chapter 3 [12]. In addition, it is proved that the

local strain energy must be considered in the grand canonical ensemble for the solid solutions by comparing the cases with and without the strain energy induced by local fluctuation. Chapter 5 shows the calculated average bandgap of Ga(As,Sb) which expands the area where the methodology from the energetics to other configuration-dependent property, bandgap [13]. Chapter 6 shows the analysis on the properties of (Be,Mg)O such as energetics, bandgap and dielectric constant [14]. It is found that the dielectric constant of (Be,Mg)O varies a lot depending on the configuration. Thus, the calculations are focused on searching the configurations having high dielectric constant which is the desired property. the unlike previous chapters.

# CHAPTER 2

## THEORETICAL BACKGROUND

---

### 2.1. Introduction

Studying a solid solution system including pseudobinary system in atomic-scale is difficult because of its non-periodicity and tremendous possible configurations. This problem is called a configurational problem.

Some methods have been adopted to examine properties of pseudobinary systems such as special quasi-random structures (SQS), special quasi-ordered structures (SQoS), and Monte Carlo simulation. However, the SQS oversimplifies a solid solution as a fully random state, which is different from reality. The Monte Carlo simulation needs a large calculation cost, although it produces more accurate energy and entropy. The SQoS requires an

atomic structure obtained by pre-run Monte Carlo simulation. Hence an accurate and efficient computational method to deal with solid solution systems is demanding.

The method used in this work is usually based on the generalized quasi-chemical approximation (GQCA) [15]. However, GQCA has an inefficiency which occurs when the method is applied to a large number of configurations. Thus, we eliminate the inefficiency resulting in a new method that combining first principle calculation, cluster expansion method, and statistical thermodynamics.

## 2.2. Density functional theory (DFT)

This section refers to the book written by Giustino [16], which gave a detailed description of DFT and related theories. The quantum mechanical behavior can be described by the Schrödinger equation. However, the Schrödinger equation can be solved only by numerical analysis except for some systems [17], and numerical analysis for the Schrödinger equation usually has high computational complexity. The Born-Oppenheimer approximation successfully reduces computational complexity by treating nuclei whose mass is thousands of times of electronic mass as stationary.

$$\left[ -\frac{1}{2}\sum_i \nabla_i^2 - V_n(r) + \frac{1}{2}\sum_{i\neq j} \frac{1}{|r_i-r_j|} \right] \Psi = E\Psi \quad (2.1)$$

, where  $r$  indicates coordinate of an electron,  $E$  is ground state energy of

electrons,  $\Psi$  indicates a wavefunction of the electron coordinates, and  $V_n(r)$  is the external potential (potential of the nuclei) which is defined as follows:

$$V_n(r) = -\sum_{i,j} \frac{Z_j}{|r_i - R_j|} \quad (2.2)$$

, where  $R$  and  $r$  are coordinates of nucleus and electron,  $Z$  is a charge of the nucleus. However, the complexity of Eq. (2.1) increases tremendously as the number of electrons increases.

Density functional theory is the successful numerical method to solve the Schrödinger equation based on the Kohn-Sham equation [18].

$$\left[ -\frac{1}{2}\nabla^2 + V_n(r) + V_H(r) + V_{XC}(r) \right] \phi_i(r) = \varepsilon_i \phi_i(r) \quad (2.3)$$

, where  $V_H(r)$  is the Hartree (electrostatic) potential,  $V_{XC}(r)$  is the exchange-correlation potential, and  $\varepsilon_i$  is the orbital energy of the corresponding Kohn-Sham orbital (wave function)  $\phi_i(r)$  for a single electron  $i$ .  $V_H(r)$  is defined as follows:

$$V_H(r) = \frac{1}{2} \int \frac{\rho(r')}{|r-r'|} dr' \quad (2.4)$$

, where

$$\rho(r) = \sum_i |\phi_i(r)|^2 \quad (2.5)$$

is electron density.

$V_n(r)$  and  $V_H(r)$  are known exactly as Eq. (2.2) and (2.4), but there is no exact form of  $V_{XC}(r)$ . To approximate  $V_{XC}(r)$ , the local density

approximation (LDA) [19] and generalized gradient approximations (GGA) such as Perdew-Burke-Erzerhof (PBE) functionals [20] are widely used.

### 2.3. Cluster expansion

Because DFT is an expensive calculation, it is hard to explore the vast configurational space using DFT. Cluster expansion is one of the machine learning to efficiently calculate the configuration-dependent properties (such as energy and bandgap) of numerous configurations without sacrificing accuracy. Cluster expansion is based on the assumption that properties come from the interaction of atoms. Thus, the property of a specific configuration is described as the sum of contributions from various clusters, which refer to a group of interacting atoms. In the scope of cluster expansion, the configuration-dependent property  $Y$  of configuration  $\sigma$  is expressed as the following equation:

$$Y_{\sigma} = \sum_k \sum_m J_{k,m}^Y \overline{\prod_{\{i\} \in (k,m)} \theta(\sigma_i)} \quad (2.6)$$

, where  $J_{k,m}^Y$  is effective cluster interaction coefficient (ECI),  $\{i\}$  is the symmetrically identical set of sites that make up the  $m^{\text{th}}$   $k$ -site cluster  $(k,m)$ , and  $\theta(\sigma_i)$  is a function that returns -1 for atom A and 1 for atom B according to an element occupying site  $i$ ,  $\sigma_i$ , of a pseudobinary system  $A_x B_{1-x} C$ . Equation (2.6) can be applied to a supercell-size-independent (intensive) property. However, the unit of energy of a configuration in this study is per microstate (per supercell) which is cell-size-dependent. Thus, Eq. (2.6) for energy is rewritten as:

$$\Delta E_{\sigma} = \sum_k \sum_m J_{k,m}^{\Delta E} \overline{\prod_{\{i\} \in (k,m)} \theta(\sigma_i)} \quad (2.6-1)$$

whereas bandgap of a configuration is calculated as:

$$\Delta E_{g,\sigma} = \sum_k \sum_m J_{k,m}^{E_g} \overline{\prod_{\{i\} \in (k,m)} \theta(\sigma_i)} \quad (2.6-2)$$

For multi-component system, the discrete Chebyshev polynomials are usually adopted to define  $\theta(\sigma_i)$  [21,22]. ECI represents the contribution of the cluster (k,m) and  $\prod_{\{i\} \in (k,m)} \theta(\sigma_i)$  represents the clusters of the configuration.  $J_{k,m}^Y$  is obtained from some configuration's DFT results. After  $J_{k,m}^Y$  is obtained, the property of any configuration can be predicted.

## 2.4. Statistical thermodynamics

Although the property of any configuration can be predicted using cluster expansion, studying a solid solution system including a pseudobinary system on the atomic scale is difficult because of its non-periodicity. No matter what large and random configuration, the configuration is hard to represent the solid solution. A breakthrough was found in the grand canonical ensemble, which regards the macroscopic system as a collection of small microstates. When configurations calculated using cluster expansion are considered as microstates, the solid solution can be described with the probabilities of configurations. According to the grand canonical ensemble, the ensemble average of property of a system ( $\bar{Y}$ ) is given by

$$\bar{Y} = \sum_{\sigma} Y_{\sigma} P_{\sigma} \quad (2.7)$$

, where  $P_\sigma$  is the probability that each configuration will occur. In the equilibrium state of a pseudobinary system  $A_xB_{1-x}C$ ,  $P_\sigma$  at a given composition ( $x$ ) and temperature ( $T$ ) is calculated according to the following equations:

$$\mathbb{Z}(x, T) = \sum_{\sigma} \exp\left(\frac{n_{\sigma}\Delta\mu - \Delta E_{\sigma}^{total}}{k_B T}\right) \quad (2.8)$$

$$P_{\sigma} = \frac{\exp\left(\frac{n_{\sigma}\Delta\mu - \Delta E_{\sigma}^{total}}{k_B T}\right)}{\mathbb{Z}(x, T)} \quad (2.9)$$

, where  $\mathbb{Z}(x, T)$  indicates the grand partition function,  $n_{\sigma}$  is the number of atoms A in a configuration  $\sigma$ ,  $k_B$  is the Boltzmann constant, and  $\Delta E_{\sigma}^{total}$  is total mixing energy of configuration. The equation  $\Delta\mu = \mu(A) - \mu(B)$  represents the difference of the chemical potential between atoms A and B, which is determined by the following equation to satisfy self-consistency:

$$x = \sum_{\sigma} x_{\sigma} P_{\sigma} = \frac{1}{N} \sum_{\sigma} n_{\sigma} P_{\sigma} = \frac{1}{N} \sum_{\sigma} n_{\sigma} \frac{\exp\left(\frac{n_{\sigma}\Delta\mu - \Delta E_{\sigma}^{total}}{k_B T}\right)}{\mathbb{Z}(x, T)} \quad (2.10)$$

, where  $x_{\sigma}$  is the composition of configuration,  $N$  denotes the sum of the number of atoms A and B. Grand canonical ensemble is often called  $\mu VT$  ensemble because microstates in the grand canonical ensemble are described in the fixed  $\mu$ , volume ( $V$ ), and  $T$ . Thus, the volume must be fixed. However, the configurations that consist of solid solutions usually have different free relaxed volumes. Thus,  $\Delta E_{\sigma}^{total}$  is the sum of free relaxed energy and strain energy to match a given volume.

$$\Delta E_{\sigma}^{total} = \Delta E_{\sigma} + E^{strain} \quad (2.11)$$

, where  $\Delta E_\sigma$  denotes the mixing energy of configuration, and  $E^{strain}$  indicates the difference of energies under free relaxed state and strained state.

For pseudobinary system  $A_xB_{1-x}C$ ,  $\Delta E_\sigma$  is defined as follows:

$$\Delta E_\sigma = E_\sigma - [x_\sigma E_{AC} + (1 - x_\sigma)E_{BC}] \quad (2.12)$$

, where  $E_{AC}$  and  $E_{BC}$  are the energy of AC and BC.

When  $Y$  is total energy, thermodynamic properties such as average total mixing energy ( $\overline{\Delta E^{total}}$ ), configurational entropy ( $S(x)$ ), and free energy ( $\Delta F$ ) of the system are calculated as follows:

$$\overline{\Delta E^{total}} = \sum_\sigma \Delta E_\sigma^{total} \frac{\exp\left(\frac{n_\sigma \Delta \mu - \Delta E_\sigma^{total}}{k_B T}\right)}{\mathbb{Z}(x, T)} \quad (2.13)$$

$$S(x) = -k_B \sum_\sigma P_\sigma \ln(P_\sigma) \quad (2.14)$$

$$\Delta F = \overline{\Delta E^{total}} - T\Delta S = Nx\Delta\mu - k_B T \ln(\mathbb{Z}(x, T)) \quad (2.15)$$

, where  $\Delta S$  indicates the mixing entropy which is defined as

$$\Delta S = S(x) - (1 - x)S(0) - xS(1) \quad (2.16)$$

The main concern in the field of pseudobinary systems is phase separation. Many pseudobinary systems mix its component well and form a single phase, but there are also a lot of pseudobinary systems whose phase is separated. The phase separation induces inhomogeneity in the electrical and optical properties as well as the nano- and micro-scale structures [23–28]. Fortunately, it is well known that the phase separation can be predicted from the  $\Delta F$ - $x$  graph. In  $\Delta F$  curve as a function of  $x$ , when the second derivative of

the mixing Helmholtz free energy ( $\partial^2\Delta F/\partial x^2$ ) is negative implying the concave curve, local compositional separation is energetically favored, while convex curve disallows local separation, which means metastable at least. Thus, the points where the second derivative of the mixing Helmholtz free energy is zero ( $\partial^2\Delta F/\partial x^2 = 0$ ) divide the metastable state and unstable state, called spinodal points. For the range of composition between the contact points of the common tangent in  $\Delta F$ - $x$  graph in a given temperature,  $\Delta F$  must be higher than  $\Delta F$  of contact points of common tangent which is averaged according to labor rule. Therefore, contact points of common tangent divide the stable state and the metastable state, called the binodal points. Then the phase diagram is obtained by collecting binodal points and spinodal points for various temperatures.

## 2.5. Dielectric constant

The dielectric constant is composed of multiple factors, which include electronic polarization, ionic polarization, dipolar polarization, interfacial polarization. However, each contributor is frequency-dependent. The electronic and ionic polarizations are two main contributors in the frequency regime of interest. It is well known that ionic contribution to dielectric constant can be calculated from phonon mode [29]. As a result, the static permittivity tensor  $\epsilon_{\alpha\beta}^0$  can be calculated as:

$$\epsilon_{\alpha\beta}^0 = \epsilon_{\alpha\beta}^{\infty} + \frac{4\pi}{V} \sum_m \frac{Z_{m\alpha}^* Z_{m\beta}^*}{\omega_m^2} \quad (2.17)$$

, where the subscripts  $\alpha$  and  $\beta$  indicate the direction of the applied electric field and the resulting polarization, respectively;  $\varepsilon_{\alpha\beta}^{\infty}$  denotes the electronic permittivity tensor;  $V$  denotes the cell volume; the subscript  $m$  denotes the phonon mode; and  $Z_{m\alpha}^*$ ,  $Z_{m\beta}^*$  and  $\omega_m$  are the mode-effective charge along the direction  $\alpha$  and  $\beta$ , and the frequency of phonon mode  $m$  at the  $\Gamma$  point in the Brillouin zone, respectively. The mode-effective charge is defined as:

$$Z_{m\alpha}^* = \sum_{\kappa,\beta} Z_{i,\alpha\beta}^* U_{i,m\beta} \quad (2.18)$$

$$U_{i,m\beta} = \frac{v_{\kappa,m\beta}}{\sqrt{M_i}} \quad (2.19)$$

, where  $i$  denotes the atom;  $Z_{i,\alpha\beta}^*$  denotes the Born effective charge tensor of atom  $i$ ;  $U_{i,m\beta}$  denotes the Eigen-displacement vector along  $\beta$  of the phonon mode  $m$ ;  $v_{i,m\beta}$  denotes the eigenvector along  $\beta$  of the atom  $i$  in the phonon mode  $m$ ; and  $M_i$  denotes the atomic mass of  $i$ . Then, the dielectric constant tensor  $\kappa_{\alpha\beta}$  was calculated as:

$$\kappa_{\alpha\beta} = \varepsilon_{\alpha\beta}^0 / \varepsilon_0 \quad (2.20)$$

, where  $\varepsilon_0$  is the permittivity of the vacuum. The electronic dielectric constant, Born effective charge, and phonon mode which are required to calculate dielectric constant tensor  $\kappa_{\alpha\beta}$  can be calculated using density functional perturbation theory (DFPT). DFPT is the powerful technique to compute response properties directly arising from the perturbations of atomic displacement, and electric field by linear response theory, based on the Sternheimer equation to calculate the variation of the Kohn-Sham orbital under

a given perturbing potential [30–34].

$$\begin{aligned} & \left( -\frac{1}{2}\nabla^2 + V_n(r) + V_H(r) + V_{XC}(r) - \epsilon_i \right) |\Delta\phi_i\rangle \\ &= -(\Delta V_n(r) + \frac{1}{2} \int \frac{\Delta\rho(r')}{|r-r'|} dr' + \left. \frac{dV_{XC}(\rho)}{d\rho} \right|_{\rho=\rho(r)} - \Delta\epsilon_i) |\phi_i\rangle \end{aligned} \quad (2.21)$$

In this dissertation, the temperature-dependent  $\kappa_{\alpha\beta}$  is calculated from the temperature-dependent phonon. Some programs have been introduced to calculate the phonon dispersion in a given temperature [35–37]. In this dissertation, the temperature-dependent  $\kappa_{\alpha\beta}$  is calculated from the the temperature-dependent phonon using Eq. (2.17).

The fluctuation method is another method to calculate temperature-dependent  $\kappa$ . Fluctuation method is based on the following equation [38,39]:

$$\kappa = \frac{1}{\epsilon_0 V k_B T} \left[ \langle \vec{M}^2 \rangle - \langle \vec{M} \rangle^2 \right] \quad (2.22)$$

, where  $\vec{M}$  indicates dipole moment. Using statistical mechanics, Eq. (2.22) can be derived from [40]:

$$F_i = U_i - V \vec{P}_i \vec{E} \quad (2.23)$$

, where  $F$  is free energy,  $U$  is internal energy,  $\vec{P}$  is polarization,  $\vec{E}$  is external field, and  $i$  indicate the microstate.

External field method is the method that calculating  $\kappa$  from the molecular dynamics under the external field as [41]:

$$\kappa = 1 + \frac{\vec{P}}{\epsilon_0 \vec{E}} \quad (2.24)$$

## CHAPTER 3

# METHODOLOGY FOR AVERAGE PROPERTY

---

### 3.1. Introduction

Although the theory is explained in chapter 2, researchers will face many obstacles when the theories are applied in practice. For example, it is impossible to calculate the strain energy in Eq. 2.11 for all configurations under various strains, and the pseudobinary system with  $2 \times 2 \times 2$  supercell of zincblende structure generates  $2^{32}$  configurations, which are too many to calculate even when cluster expansion is used. So, here is useful information which is used when conducting research applying the methodology to  $\text{GaAs}_x\text{Sb}_{1-x}$  and  $\text{In}_x\text{Ga}_{1-x}\text{As}$ . Note that the statistic thermodynamics part in methodology is coded and the program is available at <https://5pg.readthedocs.io/en/latest/>

## 3.2. Density functional theory (DFT)

Figure 3.1 shows the reason why  $E^{strain}$  in  $\Delta E_{\sigma}^{total}$  is mandatory to calculate the probability of a configuration  $P_{\sigma}$ . Figure 3.1 (a) depicts the schematics of the grand canonical ensemble where all the microstates are freely relaxed, hence, the strain energy is zero. In Fig. 3.1 (b), in contrast, all microstates have the uniform lattice constant of the average composition, implying that each microstate is under a local strain condition.

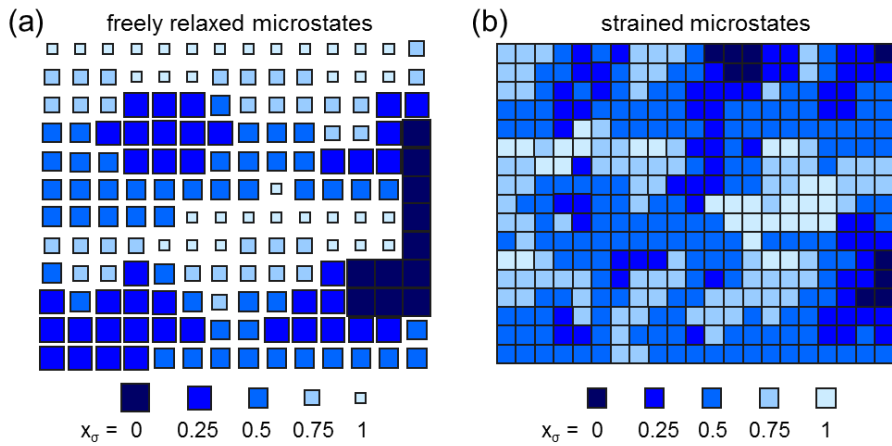


**Figure 3.1** Schematic of the grand canonical ensemble with (a) freely relaxed microstates, (b) microstates under strain induced by local compositional fluctuation at  $x = 0.5$ . The side length of the square refers to the lattice constant in each microstate.

Thus, to calculate the probability of a configuration  $P_{\sigma}$ , it is mandatory to calculate  $E_{\sigma}^{strain}$  to obtain  $\Delta E_{\sigma}^{total}$ . There are two methods to account for this strain energy. One is the calculation of the  $J_{k,m}^{\Delta E}$  under strain from the data sets obtained by the DFT calculations as in the previous study [42], and the other is the post-addition of the average strain energy to the mixing energy in the freely relaxed state,  $\Delta E_{\sigma}$ . The former needs DFT calculations for all configurations under strain. Therefore, it does not meet the primary purpose of using the CE, which is a reduction in the computational cost without sacrificing accuracy. If the  $E_{\sigma}^{strain}$  is independent of the configuration, then the latter is valid.

To confirm whether the configuration affects the  $E_{\sigma}^{strain}$  or not, the  $E_{\sigma}^{strain}$  at two relative volumes  $V/V_0$  of 0.9 and 1.1 were tested assuming an isostatic strain at  $x = 0.5$ .  $V$  and  $V_0$  are the strained volume and the freely relaxed volume, respectively. The  $E_{\sigma}^{strain}$  of 20 arbitrary configurations for  $(\text{GaAs})_{0.5}(\text{GaSb})_{0.5}$  and 11 configurations for  $(\text{InAs})_{0.5}(\text{GaAs})_{0.5}$  were calculated. The standard deviation of  $E_{\sigma}^{strain}$  were evaluated to be below 0.6 meV/atom for  $(\text{GaAs})_{0.5}(\text{GaSb})_{0.5}$  and 0.7 meV/atom for  $(\text{InAs})_{0.5}(\text{GaAs})_{0.5}$ , respectively. This implies that  $E_{\sigma}^{strain}$  does not depend on the configuration [15] and can thus be estimated using a small number of configurations for a given local composition  $x_{\sigma}$  and given volume  $V$ .

It is obvious that  $E_{\sigma}^{strain}$  depends on target volume and the volume

of configuration in the free relaxed state also varies. Because calculating  $E^{strain}$  for all configurations takes a huge amount of calculation cost, a simple method to obtain strain energy must be found for the efficiency of methodology. Thus, the author focus on the Birch-Murnaghan equation of state, the well-known equation that describing the strain energy [43].

$$E^{strain} = \frac{9V_0B_0}{16} \left\{ \left[ \left( \frac{V_0}{V} \right)^{\frac{2}{3}} - 1 \right]^3 B'_0 + \left[ \left( \frac{V_0}{V} \right)^{\frac{2}{3}} - 1 \right]^2 \left[ 6 - 4 \left( \frac{V_0}{V} \right)^{\frac{2}{3}} \right] \right\} \quad (3.1)$$

, where  $B_0$  and  $B'_0$  are the bulk modulus and its derivative, and  $V_0$  and  $V$  are the volume without strain and with strain. Because  $B_0$  depends on materials, only target volume and volume of free relaxed configuration are required to calculate strain energy. Though the difference in lattice constant between GaAs and GaSb, and between InAs and GaAs is large, both  $\text{GaAs}_x\text{Sb}_{1-x}$  and  $\text{In}_x\text{Ga}_{1-x}\text{As}$  follows substitutional Hume-Rothery rules [44], and lattice constants ( $a_0$ ) of  $\text{GaAs}_x\text{Sb}_{1-x}$  and  $\text{In}_x\text{Ga}_{1-x}\text{As}$  follow Vegard's law well as in the experimental literature [45–48] and in the calculation of this work in Fig. 3.2, fortunately. Therefore the target volume is determined according to average composition  $x$ , and the volume of configuration is determined by local composition  $x_\sigma$ . The  $B_0$  values calculated by fitting the  $E^{strain}$  show feasible agreements with the experimental  $B_0$  value.

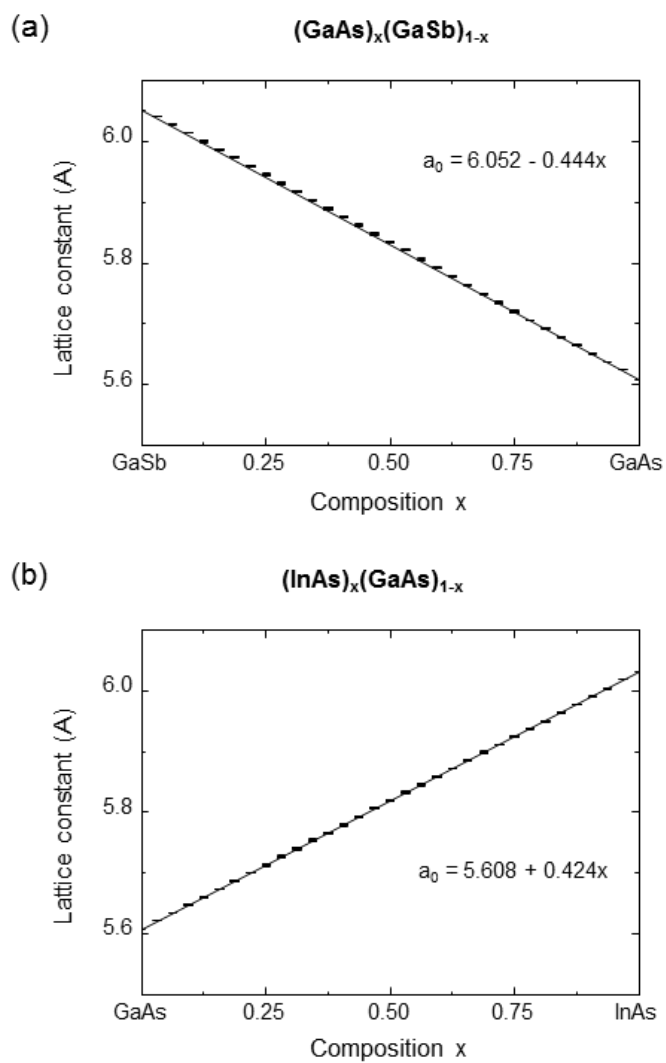


**Figure 3.2** (a) Lattice constant of 236 configurations of  $(\text{GaAs})_x(\text{GaSb})_{1-x}$  and (b) lattice constant of 297 configurations of  $(\text{InAs})_x(\text{GaAs})_{1-x}$  in  $2 \times 2 \times 2$  supercell. The solid line follows Vegard's rule.

### 3.3. Cluster expansion

The pseudobinary system  $A_xB_{1-x}C$  has the fixed atom C, which corresponds to Ga in  $GaAs_xSb_{1-x}$  and As in  $In_xGa_{1-x}As$ . When atom C participates in performing cluster expansion, the computational amount increases by at least 2 times. Thus, it is better to ignore the fixed atom C. It should be noted that symmetry should be preserved. When atom C is ignored, a zinc-blende structure becomes a face-centered cubic (FCC) structure. The space group of zinc-blende structure ( $F\bar{4}3m$ ) and FCC ( $Fm\bar{3}m$ ) is different, some clusters which are distinct in a zinc-blende structure become symmetrically identical in FCC structure. Fig. 3.3.1 shows an example of clusters in the case. When the clusters that distinct in zinc-blende structure are maintained after atom C is ignored, calculation efficiency is improved more than twice without loss of accuracy. The validity of ignoring atom C can be confirmed by comparing the equations of the cluster expansion method for the cases with and without atom C.

### 3.4. Thermodynamic statistics

#### 3.4.1 Ensemble average

The desired properties vary depending on the application, but the bandgap of pseudobinary semiconductors is always important, and Ga(As,Sb) and (In,Ga)As bandgaps are calculated in this dissertation. Considering the

pseudobinary systems including Ga(As,Sb) and (In,Ga)As are utilized in a solid solution state, not in an ordered structure, it is quite weird to discuss the bandgap because band theory assumes a periodic system. However, there is the experiment literature which observes the band structure of the solid solution system [49] and theoretical evidence that periodicity can be restored by choosing proper effective particles [50].

Even though the bandgap can be defined in the solid solution, it is another problem whether calculating the bandgap of a system as an ensemble average of the bandgap is valid or not. It is hard to prove where bandgap can be calculated using ensemble average. Nevertheless, we try to explain the validity. One literature explains it by the fact that the VBM and CBM states of solid solution are delocalized as ordered structures when the valence state of atom A and atom B in  $A_xB_{1-x}C$  is the same [51]. From an empirical point of view, there are literature which calculates the bandgap of system as average of canonical ensemble [11,52,53]. From a mathematical point of view, average property calculated using grand canonical ensemble is one of the weighted arithmetic mean for microstates as Eq. (2.7) and the cluster expansion is also the weighted arithmetic mean for clusters as Eq. (2.6). Thus, the grand canonical ensemble average for the cluster expansion results is in principle the same as the cluster expansion result for the infinite cell. Thus, if the cluster expansion on bandgap is acceptable, ensemble averaging for bandgap can also be adopted. Although the cluster expansion is usually applied to energy, bandgap is also a property which can be computed using the cluster expansion and there are literatures that cluster expansion is applied to bandgap [54–58].

### 3.4.2 Number of samples

To calculate grand partition function  $\mathbb{Z}(x, T)$ , properties of all microstates are required. When the number of configurations is small enough to simulate all configurations, it is reasonable to reduce the computational cost by adopting the weight according to the number of symmetrically equivalent configurations. However, zinc-blende  $\text{GaAs}_x\text{Sb}_{1-x}$  and  $\text{In}_x\text{Ga}_{1-x}\text{As}$  in  $2 \times 2 \times 2$  supercell generate  $2^{32} \approx 4.3 \times 10^9$  configurations, which are too many to calculate, although cluster expansion enables fast prediction of properties of configurations. Thus, random sampling was used. According to ‘the law of large numbers’, the average energy obtained from a sufficiently large number of configurations should be close to the true average value. Besides, the number of possible configurations at each local composition,  $K$ , greatly varies depending on the local composition,  $n/N$ , as follows

$$K = {}_N C_n = \frac{N!}{n!(N-n)!} \quad (3.2)$$

$K_{n/N=0}$  and  $K_{n/N=1}$  is only one, and  $K_{n/N=1/32}$  and  $K_{n/N=31/32}$  (the second-lowest or the second-highest local composition in the  $2 \times 2 \times 2$  supercell) is 32. These  $K$  values are too small compared to  $K_{n/N=0.5}$  ( $= 32!/16!/16! = \sim 6.0 \times 10^8$ ). This means that the local composition near 0 or 1 cannot be selected in a fully random manner among all possible configurations,  $2^{32}$ . This may result in insufficient accuracy near both ends of the composition range. In this dissertation, for the even sampling for each  $n/N$ , the number of configurations

calculated using CE,  $K'$ , for each discrete  $n/N$  was set to 10,000. This means that a total of 330,000 configurations spanning 33 local compositions were calculated using CE.  $K' = 10,000$  was found to be large enough to converge the average mixing energy for  $n/N = 0.5$  within 1 meV/atom. ‘Simple random sampling with replacement’ was conducted to select configurations for  $K'$ . Thus, sampling more than the real possible configurations ( $K < K'$ ) for some local compositions near both ends of the composition range is not a problem.

The canonical partition function, which does not allow the local compositional fluctuation,  $z(n/N, T)$  for  $K' = 10,000$  was calculated as in the previous study using the correction term  $K/K'$  [59].

$$z\left(\frac{n}{N}, T\right) = \sum_{\sigma(n_{\sigma}=n)} \exp\left(\frac{-\Delta E_{\sigma}}{k_B T}\right) \frac{K}{K'} \quad (3.3)$$

Then, the grand canonical partition function  $\mathbb{Z}(x, T)$  can be described as a function of the canonical partition function  $z(n/N, T)$ .

$$\mathbb{Z}(x, T) = \sum_{n=0}^N \exp\left(\frac{n\Delta\mu - E_{\sigma(n_{\sigma}=n)}^{strain}}{k_B T}\right) z\left(\frac{n}{N}, T\right) \quad (3.4)$$

where  $E_{\sigma(n_{\sigma}=n)}^{strain}$  is the strain energy of configurations whose  $n_{\sigma}$  is  $n$ .

Note that the  $E_{\sigma(n_{\sigma}=n)}^{strain}$  can be calculated using DFT as the section 3.2, and  $z(n/N, T)$  can be calculated with  $\Delta E_{\sigma}$  according to Eq. (3.3).

# CHAPTER 4

## PHASE DIAGRAM OF

## III-V SEMICONDUCTOR SOLID SOLUTION

---

### 4.1. Introduction

III-V compound semiconductor materials have been extensively studied due to their tunability in properties as well as lattice constant [60,61]. In particular, pseudobinary systems composed of III-V compounds such as Ga(As,Sb) and (In,Ga)As are of interest in semiconductor devices and optoelectronic applications [62–64]. However, some of these systems have phase separation, which induces many disadvantages as discussed in chapter 2. Therefore, it is crucial to understand the atomic scale local fluctuations, which will improve the performance of applications. The phase diagram is useful as a critical guide to phase separation. However, experimental phase diagrams for some III-V pseudobinary systems are not available, which is partly due to an

excessively large amount of experimental work to obtain phase diagrams. For instance, phase diagrams of Al(P,Sb) [65] and Al(As,Sb) [66] were reported only by calculations, not by experiments yet. In this regard, theoretical means using *ab initio* calculations could be a viable alternative to obtain the necessary phase diagrams.

Among several calculation methods developed for the phase diagrams, we focus on a non-empirical method because a non-empirical method can be also applicable to new materials. In general, the calculation methods are mainly composed of two parts: a calculation of the energy, and a calculation of the entropy. A previous study on Ga(As,Sb) using the special quasi-random structure (SQS) oversimplified the energy calculations by selecting one representative configuration for only five compositions [67] whereas the number of viable atomic configurations should be much higher. The sampling of configurations was insufficient to take into account the characteristic randomness of a solid solution, which resulted in a large error in the energy calculation. On the other hand, this previous report treated the entropy as the ideal entropy of mixing [67], which may differ from the actual entropy at a low temperature. Another study used a more statistical method to calculate the phase diagrams of Ga(As,Sb) and (In,Ga)As by introducing generalized quasi-chemical approximation (GQCA) [15]. Although the GQCA method is theoretically accurate, that work also used only one configuration for each of the five compositions. As a result, the phase diagrams of Ga(As,Sb) calculated by using SQS and GQCA showed a large discrepancy in the binodal line and the upper critical solution temperature ( $T_c$ ) when compared to experimental

results [68–71].

The more configurations and corresponding energies are calculated, the higher statistical accuracy can be achieved. However, it is impossible to calculate all the energetics of countless configurations using first-principles calculations due to the enormously high computational cost. To solve this problem, Wei *et al.* introduced a cluster expansion (CE) method that enables rapid predictions of the energies for a large number of configurations based on the results obtained using first-principles calculations [42]. To estimate the average energy for all configurations, they used a relatively small system composed of 8 configurations in a  $1 \times 1 \times 2$  supercell. Many studies using CE calculated energy and entropy by assuming an entirely random structure [72–74]. In these studies, the configuration-dependent energetic stability was neglected, therefore, the probability of each configuration to occur was considered the same. However, it is different from reality [75]. Meanwhile, a Monte Carlo simulation is another approach to calculate the energy and entropy more realistically using CE. Such methods have been used to predict the phase diagrams of III-V compound semiconductors [42,73–77]. However, they demand more computational resources than CE. Therefore, it is still necessary to introduce an accurate and efficient computational method to predict phase diagrams.

This chapter presents an accurate and efficient prediction of the phase diagrams of Ga(As,Sb) and (In,Ga)As using a combined methodology composed of: density functional theory (DFT) calculations to guarantee

accurate energy; CE to properly account for the innumerable configurations; and grand canonical ensemble to consider the local compositional fluctuation, for obtaining the accurate average energy and entropy efficiently. Recently, a similar method has been called multi-configurational supercell approach [11] while the method has been used for a long time [59,78], but it uses the canonical ensemble which prohibits compositional fluctuation and treats discrete composition. The methodology in this chapter using grand canonical ensemble allows compositional fluctuation which is more realistic and enables to treat continuous composition range. In addition, the effect of the local strain induced by the local compositional fluctuation on the prediction of phase diagram is thoroughly investigated, which has not been focused despite its importance in the grand canonical ensemble to date. Although a previous study already considered the local strain [42], it treated the local strain within the DFT calculations by changing the volume of all configurations calculated, which demands further excessive computational cost. In contrast, this chapter separately calculates the local strain energy and then added it to the energy of a freely relaxed configuration obtained by DFT calculations and CE, which significantly diminished the computational cost without losing accuracy. By applying this method to Ga(As,Sb) whose phase diagram has been intensively studied in experiments [68–71], it is confirmed that the calculated phase diagram accurately reproduced the experimental binodal points. Then, the phase diagram of (In,Ga)As is also predicted by this method, and the prediction for the miscibility gap is compared to the experimental value, which is the only result found in the experimental report [79]. They show a feasible agreement,

suggesting the accuracy and efficiency of the present method. The overall calculations can be transferable to other III-V pseudobinary systems to obtain the phase diagram efficiently. Finally, an intuitive prediction of the phase separation is suggested by a simple estimation of the strain energy using the ratio of lattice parameters between the III-V semiconductor materials.

## 4.2. Computational details

### 4.2.1 Density functional theory

Density functional theory calculations were performed using the Vienna Ab-initio Simulation Package (VASP) [80,81]. Blöchl's projector augmented wave (PAW) approach [82,83] was used to describe the electron-core interaction. DFT calculations were performed for the configurations in  $2 \times 2 \times 2$  supercells which were generated by DBmaker in the Lattice Configuration Simulation (LACOS) package [84]. The local density approximation (LDA) [19,85] was used for the exchange-correlation potential. The energy cutoff for the plane-wave basis function was 500 eV and all the atomic positions and cell parameters were relaxed until the Hellmann-Feynman forces were below  $0.02 \text{ eV}/\text{\AA}$  using  $\Gamma$ -centered  $3 \times 3 \times 3$  k-points. Strain energies were calculated by changing  $V/V_0$  for randomly selected configurations, which were at least three for each composition at regular intervals in the entire composition. The calculated strain energies were fitted to Birch-Murnaghan EOS in Eq. (3.1).

### 4.2.2 Cluster expansion

The cluster expansion (CE) method was performed using the LACOS package [84]. The CE method efficiently calculates the configuration-dependent properties of numerous configurations without sacrificing accuracy. In the CE method, the particular property of a configuration is described as the sum of contributions from various clusters, where a cluster refers to a group of interacting atoms. In this dissertation, a cluster composed of  $k$  atoms is called a  $k$ -site cluster, and  $m$ -th  $k$ -site cluster is expressed as  $(k,m)$ . Using the properties of configurations calculated by DFT as training data, the effective cluster interaction coefficient (ECI) of each cluster is iteratively evaluated. The ECI indicates the contribution of each cluster. Then, the ECIs enable the prediction of the properties of any arbitrary configurations without expensive electronic calculations. The ECIs were calculated using the genetic algorithm implemented in the LACOS package from the energies of configurations calculated with LDA. The genetic algorithm implemented in the LACOS package was used to calculate ECI for the database using LDA. After obtaining ECI, the properties of 10,000 configurations for every possible composition at interval 0.03125 ( $= 1/32$ ) in the  $2 \times 2 \times 2$  supercell were evaluated, for a total of 330,000 configurations. The properties of configurations were used to obtain the average properties using Eq. (2.7).

### 4.3. Phase diagrams of Ga(As,Sb) and (In,Ga)As

The ensemble size of the pseudobinary  $(AC)_x(BC)_{1-x}$  in CE is set to the  $2 \times 2 \times 2$  supercell having 32 sites for  $A$  and  $B$  atoms. It generates  $2^{32}$  ( $= \sum_{n=0}^{32} {}_N C_n \sim 4.3 \times 10^9$ ) possible configurations, that are too many configurations for which to calculate all properties. Thus, DFT calculation and CE method are combined to improve the calculation efficiency. At first, the mixing energy,  $\Delta E_\sigma$ , is calculated by DFT calculation. Then,  $\Delta E_\sigma$  is calculated by CE method. Figure 4.1 (a) and (b) show the calculated  $J_{k,m}^{\Delta E}$  for the freely relaxed  $(\text{GaAs})_x(\text{GaSb})_{1-x}$  and  $(\text{InAs})_x(\text{GaAs})_{1-x}$ , respectively. The corresponding cluster for each  $J_{k,m}^{\Delta E}$  are represented in Fig. 4.1 (c). Among 240 candidate clusters, 28 and 17 effective clusters are selected for  $(\text{GaAs})_x(\text{GaSb})_{1-x}$ , and 17 effective clusters are selected for  $(\text{InAs})_x(\text{GaAs})_{1-x}$  by genetic algorithm.

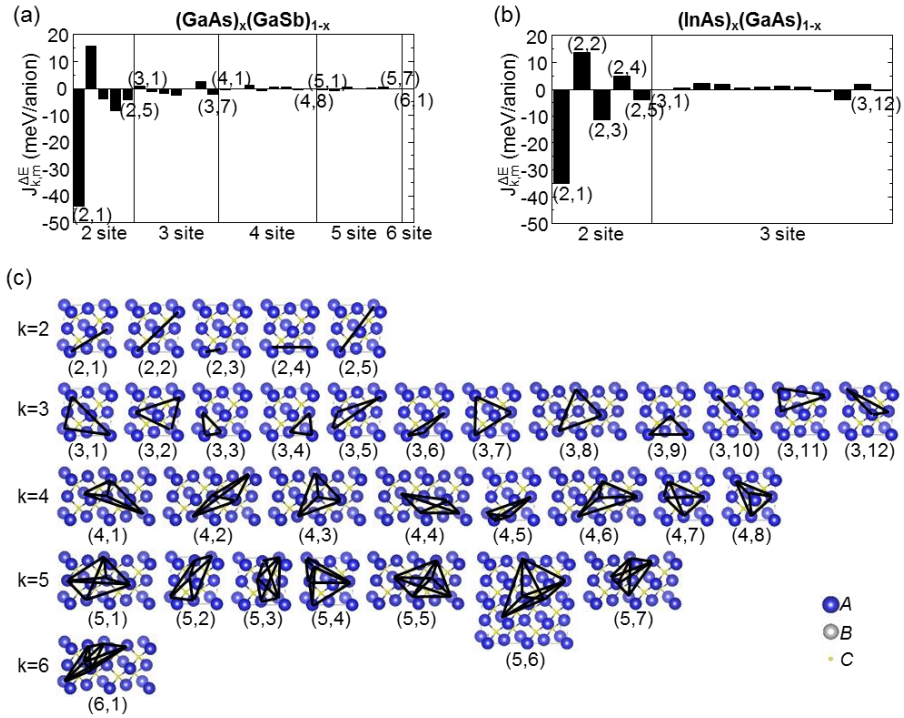


**Figure 4.1** ECIs of (a)  $(\text{GaAs})_x(\text{GaSb})_{1-x}$  and (b)  $(\text{InAs})_x(\text{GaAs})_{1-x}$ . (c)

Cluster corresponding to  $J_{k,m}^{\Delta E}$ . The set of numbers (k,m) denotes m-th k-site cluster.

As discussed in chapter 3, it is verified that the  $E_{\sigma}^{strain}$  depends only on the local composition regardless of configuration. But for further verification, at least three configurations for each of the nine compositions at regular intervals in the entire composition range are randomly selected and the strain energies are calculated by changing  $V/V_0$ . Figure 4.2 (a) and (b) show the strain energies of  $(\text{GaAs})_x(\text{GaSb})_{1-x}$  and  $(\text{InAs})_x(\text{GaAs})_{1-x}$  as a function of the  $V/V_0$  calculated in  $2 \times 2 \times 2$  supercell and the data are fitted to the Birch-Murnaghan equation of state (B-M EOS) in Eq. (3.1) [43] as the black curves. It is confirmed that the B-M EOS curve can reproduce the strain energy per atom when  $E_{\sigma}^{strain}$  is calculated in  $2 \times 2 \times 2$  supercell for  $(\text{GaAs})_x(\text{GaSb})_{1-x}$ .

The left y-axis is the strain energy of the system, while the right y-axis is the strain energy per atom. Note that the  $V/V_0$  range in Fig. 4.2 covers all possible strain ranges from dilute  $AC$  in  $BC$  to dilute  $BC$  in  $AC$  for  $(AC)_x(BC)_{1-x}$ . For  $(\text{GaAs})_x(\text{GaSb})_{1-x}$ , dilute  $AC$  in  $BC$  refers to the microstate of GaAs ( $a = 5.653 \text{ \AA}$ ) under an isostatic strain condition induced by the matrix GaSb ( $a = 6.118 \text{ \AA}$ ), and so on. All strain energies are fitted by a single B-M EOS curve irrespective of the configuration and composition, indicating  $V_0 B_0$  is almost constant within a range that maintains accuracy. Therefore,  $E_{\sigma}^{strain}$  can be easily estimated by these graphs for any  $V/V_0$  hence is separately added as the second term in Eq. (2.11). Note that  $V$  is determined by the local composition  $x_{\sigma}$ , while  $V_0$  is determined by the average composition  $x$ . In addition, Fig. 3.2 already shows the calculated lattice constants ( $a_0$ ) of these systems which

follow Vegard's law well as in the experimental literatures [45–48]. The  $a_0$  of  $(\text{GaAs})_x(\text{GaSb})_{1-x}$  and  $a_0$  of  $(\text{InAs})_x(\text{GaAs})_{1-x}$  are 0.7–0.8% and 0.4–0.8% smaller than the experimental values. From the fitted B-M EOS in Fig. 4.2,  $B_0$  is calculated:  $B_0$  for GaAs is calculated as 71.9 GPa from Fig. 4.2 (a) and 73.6 GPa; 57.2 GPa for GaSb from Fig. 4.2 (a); and 59.1 GPa for InAs from Fig. 4.2 (b). They all show good agreement with the experiment  $B_0$  values [86], as the difference from the experimental values are within 1.6 and 3.8 % for GaAs, - 0.4 % for GaSb, and 1.4 % for InAs, respectively.

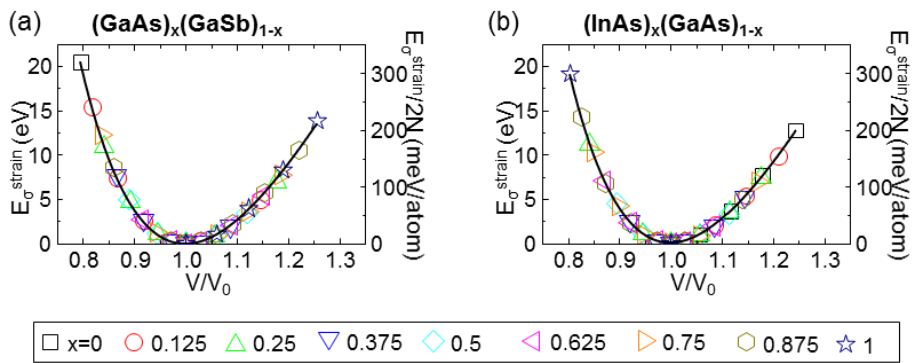


**Figure 4.2** Strain energy induced by local compositional fluctuation as a function of the relative volume  $V/V_0$  for various compositions of (a)  $(\text{GaAs})_x(\text{GaSb})_{1-x}$  and (b)  $(\text{InAs})_x(\text{GaAs})_{1-x}$ . The black curves were fitted to the B-M EOS.

Figure 4.3 (a) and (b) show the mixing energy,  $\Delta E_\sigma$ , for  $(\text{GaAs})_x(\text{GaSb})_{1-x}$  and  $(\text{InAs})_x(\text{GaAs})_{1-x}$ . The left y-axis is the mixing energy of the system, while the right y-axis is the mixing energy per atom. The green bar symbols are the individual  $\Delta E_\sigma$  values of 330,000 configurations calculated by CE with  $K' = 10,000$ . From these individual  $\Delta E_\sigma$  values, the average mixing energy,  $\overline{\Delta E^{total}}$  for a given  $x$  and  $T$  were obtained at 300, 600, and 900 K from Eq. (2.13). To investigate the effect of the strain energy, the  $\overline{\Delta E^{total}}$  with (black bold lines) and without (red lines) the strain energy are calculated. For the case without strain energy, the  $E_{\sigma(n_\sigma=\mathbf{n})}^{strain}$  is set as zero. The  $\overline{\Delta E^{total}}$  increases as the temperature increases and it tends to be more apparent when the strain energy is not taken into account.

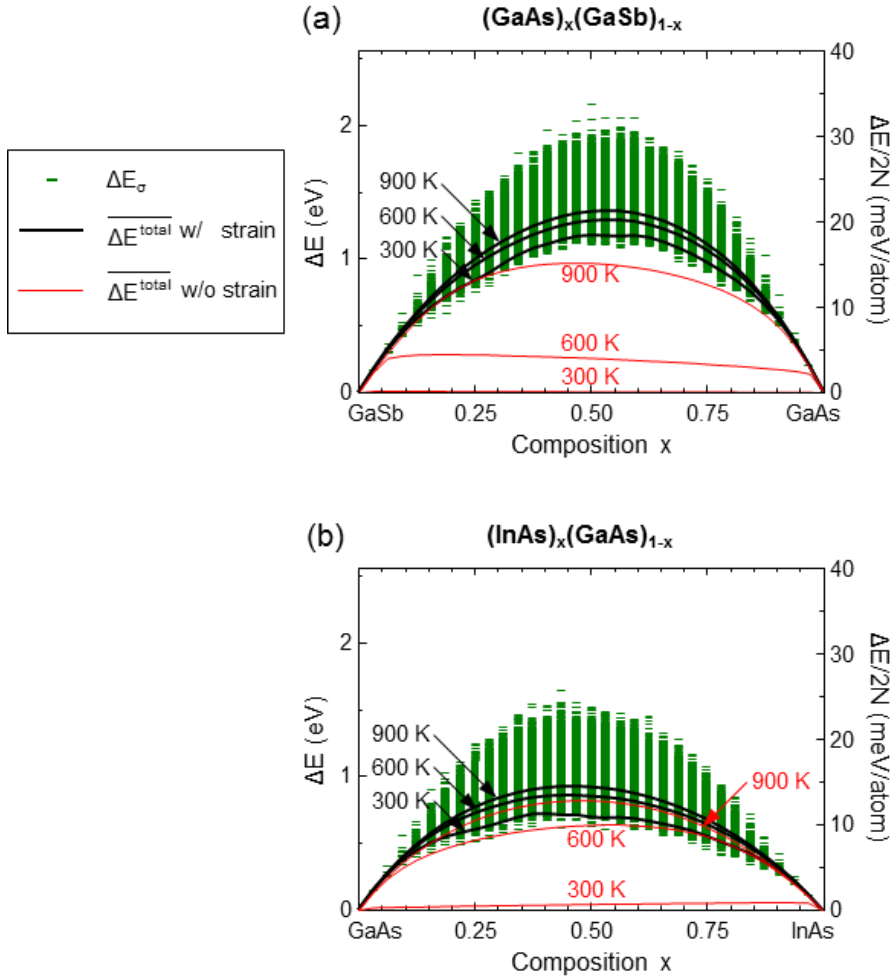


**Figure 4.3** Mixing energy of (a)  $(\text{GaAs})_x(\text{GaSb})_{1-x}$  and (b)  $(\text{InAs})_x(\text{GaAs})_{1-x}$ . The green bar symbol represents  $\Delta E_\sigma$  calculated by the CE. The black bold line and red line correspond to  $\overline{\Delta E^{total}}$  calculated with and without considering the strain energy at 300, 600, and 900 K, respectively.

The difference between  $\overline{\Delta E^{total}}$  for the cases with and without strain energy can be explained by the probability of configurations whose local composition is  $n/N$  to occur,  $P_{n/N}$ .

$$P_{n/N} = \sum_{\sigma(n_{\sigma}=n)} P_{\sigma} = \sum_{\sigma(n_{\sigma}=n)} \frac{\exp\left(\frac{n_{\sigma}\Delta\mu - \Delta E_{\sigma}^{total}}{k_B T}\right)}{\mathbb{Z}(x,T)} \quad (4.1)$$

Figure 4.4 (a) and (b) show the  $P_{n/N}$  for the average composition  $x = 0.5$  at 300, 600, and 900 K in the case of  $(\text{GaAs})_{0.5}(\text{GaSb})_{0.5}$  and  $(\text{InAs})_{0.5}(\text{GaAs})_{0.5}$ . The red line denotes  $P_{n/N}$  calculated without strain energy, while the black bold line denotes  $P_{n/N}$  calculated with the strain energy. Without considering the strain energy, the configurations whose local compositions are near both ends appear dominantly due to their low  $\Delta E_{\sigma}$ . In contrast, when the strain energy is considered,  $P_{n/N}$  shows a peak where  $n/N$  is the same as  $x = 0.5$  because the  $E_{\sigma}^{strain}$  in Fig. 4.2 is one order larger than the  $\Delta E_{\sigma}$  in Fig. 4.3. It seems to be more plausible that the black line in Fig. 4.4 is closer to the real situation that the local composition of each microstate slightly deviates from the average composition. The discrepancy between the red line and the black line in Fig. 4.3 becomes less distinct as the temperature increases because the  $P_{n/N}$  distribution becomes broader for both cases. Therefore, the difference between the black line and red line at a given temperature in Fig. 4.3 decreases along with the increase in temperature.

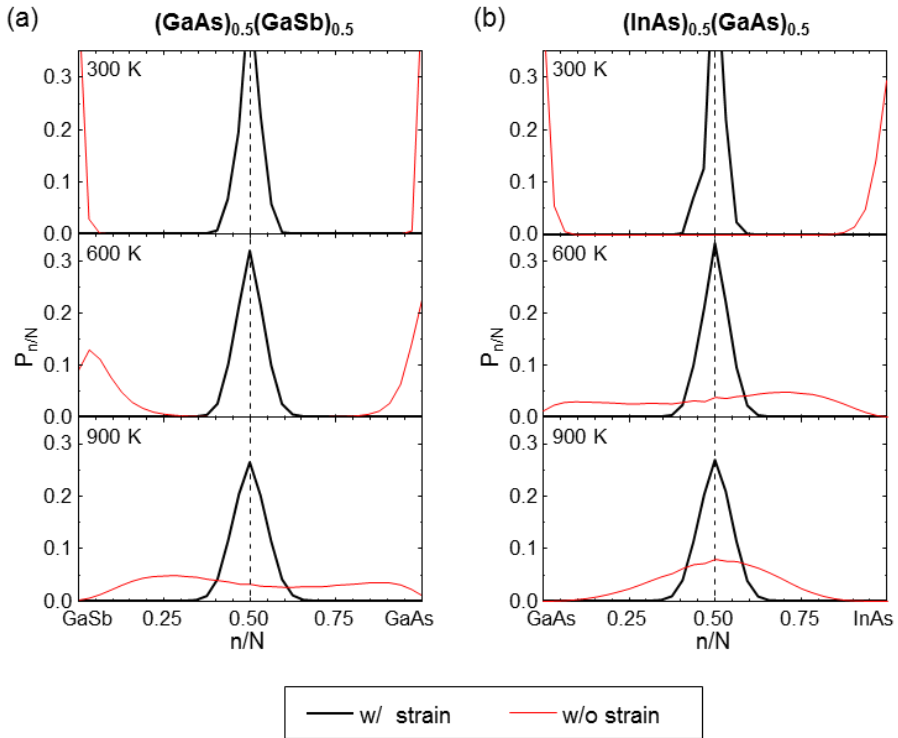


**Figure 4.4**  $P_{n/N}$  of (a)  $(\text{GaAs})_{0.5}(\text{GaSb})_{0.5}$  and (b)  $(\text{InAs})_{0.5}(\text{GaAs})_{0.5}$  at 300, 600 and 900 K. The dotted line represents  $n/N = x = 0.5$ .

Figure 4.5 (a) and (b) show the calculated mixing Helmholtz free energies,  $\Delta F$ , as a function of the composition at 300, 600, and 900 K for  $(\text{GaAs})_x(\text{GaSb})_{1-x}$  and  $(\text{InAs})_x(\text{GaAs})_{1-x}$ . In Fig. 4.5 (a) and (b), the left y-axis is the  $\Delta F$  of the system, and the right y-axis is the  $\Delta F$  per atom. The black bold lines and red lines correspond to the  $\Delta F$  calculated with and without the strain energy, respectively. Both  $\Delta F$  of Fig. 4.5 (a) and (b) are convex downward in the whole composition range. It can be mathematically proved that the  $\Delta F$  without strain energy is always convex downward by developing the double differentiation of the general expression of  $\Delta F$  without strain with respect to the composition.

$$\frac{\partial^2 \Delta F}{\partial x^2} = N \frac{\partial \Delta \mu}{\partial x} = N^2 \frac{k_B T}{n^2 - \bar{n}^2} \geq 0 \quad (4.2)$$

Equation (4.2) shows that the double differentiation of  $\Delta F$  is always positive or zero. This means that phase separation never occurs in any solid solution if the strain energy is not considered in the grand canonical ensemble.

In contrast, if the strain energy is considered, the second derivative of  $\Delta F$  is developed as:

$$\frac{\partial^2 \Delta F}{\partial x^2} = \frac{1}{k_B T} (\bar{n}^2 - \bar{n}^2) \left( \frac{\partial \Delta \mu}{\partial x} \right)^2 + \frac{\partial^2 \bar{E}}{\partial x^2} + \frac{1}{k_B T} \left( \frac{\partial \bar{E}^2}{\partial x} - \overline{\left( \frac{\partial E}{\partial x} \right)^2} \right) \quad (4.3)$$

where  $\frac{\partial \bar{E}}{\partial x}$  and  $\overline{\left( \frac{\partial E}{\partial x} \right)^2}$  are defined as

$$\frac{\partial \bar{E}}{\partial x} = \sum_{\sigma} \frac{\partial \Delta E_{\sigma}^{\text{total}}}{\partial x} P_{\sigma} = \sum_{\sigma} \frac{\partial E_{\sigma}^{\text{strain}}}{\partial x} P_{\sigma} \quad (4.4)$$

$$\overline{\left(\frac{\partial E}{\partial x}\right)^2} = \sum_{\sigma} \left(\frac{\partial \Delta E_{\sigma}^{total}}{\partial x}\right)^2 P_{\sigma} \quad (4.5)$$

In Eq. (4.3), the first term is always positive. The second term in Eq. (4.3) is also positive because  $\frac{\partial^2 E}{\partial x^2}$  is the same as  $\frac{\partial^2 E_{\sigma}^{strain}}{\partial x^2}$ , and  $E_{\sigma}^{strain}$  has a convex downward curve in the  $x$  range of interest, as shown in Fig. 4.2. On the other hand, the last term in Eq. (4.3) is always negative mathematically, because it is the negative value of the deviation of the strain energy over  $k_B T$ . Therefore, Eq. (4.3) can be either positive or negative, which means  $\Delta F$  may have inflection points, as shown in the black lines in Fig. 4.5, where phase separation occurs. Thus, for solid solutions with wide-range-tunable lattice constants as materials in this work having approximately 7% lattice change, the strain energy must be considered in the grand canonical partition function to calculate the correct thermodynamic properties. Detailed proofs on Eq. (4.2) and (4.3) are provided in section 4.6

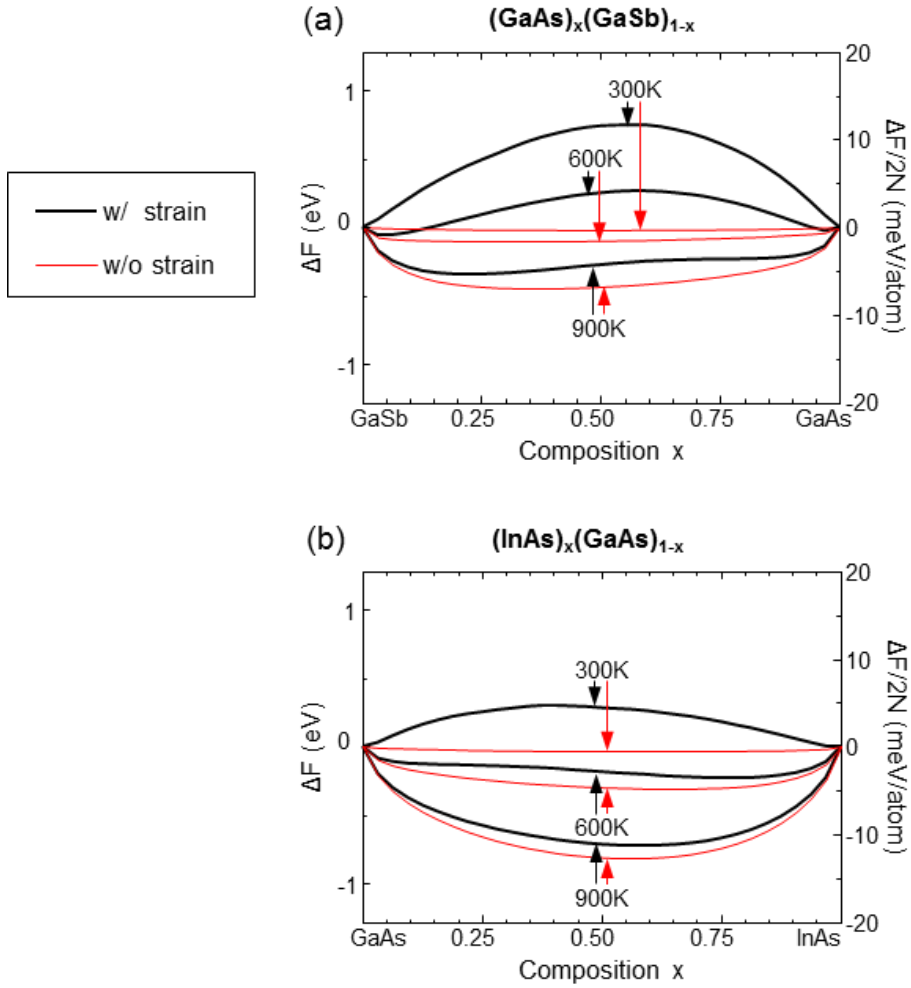


**Figure 4.5**  $\Delta F$  of (a)  $(\text{GaAs})_x(\text{GaSb})_{1-x}$  and (b)  $(\text{InAs})_x(\text{GaAs})_{1-x}$  at 300, 600, and 900 K calculated with strain energy (black line) and without strain energy (red line).

Finally, the phase diagrams of  $(\text{GaAs})_x(\text{GaSb})_{1-x}$  and  $(\text{InAs})_x(\text{GaAs})_{1-x}$  are calculated from  $\Delta F$  considering the strain (black lines in Fig. 4.5), using the grand canonical ensemble, as shown in Fig. 4.6 (a) and (b). The black solid and black dotted lines are the calculated binodal and spinodal lines, respectively. The gray area above the solidus curve indicates the region where the liquid phase of  $(\text{GaAs})_x(\text{GaSb})_{1-x}$  [46,71] and  $(\text{InAs})_x(\text{GaAs})_{1-x}$  [87] appear experimentally.

The colored symbols in Fig. 4.6 indicates the experimental results measured by x-ray diffraction [68,69], electron probe microanalyzer [68,70,71] and transmission electron microscopy [79]. The calculated binodal line for  $(\text{GaAs})_x(\text{GaSb})_{1-x}$  in this chapter shows good agreement with the experimental results. In this calculation,  $T_c$  is 1040 K for  $(\text{GaAs})_{0.58}(\text{GaSb})_{0.42}$ . However, this  $T_c$  is located slightly above the solidus curve in the experimental literature [46], which means that  $(\text{GaAs})_x(\text{GaSb})_{1-x}$  is expected to melt before reaching the  $T_c$  as the temperature increases. The colored thin lines are the calculated results reported by using SQS with 5 samples ignoring the local strain energy (green) [67]; using GQCA with 5 samples considering the local strain energy (blue) [15]; using CE with 10 DFT samples considering local strain energy (red) [42]. The red thin line is the closest to our results, which demonstrates the independence of the strain energy on the configuration and the importance of the local strain energy. However, this red thin line is obtained by using ECIs as a function of volume, which requires a much larger amount of DFT calculations compared to our method. In the calculated  $(\text{InAs})_x(\text{GaAs})_{1-x}$  phase diagram in

Fig. 4.6 (b), on the other hand,  $T_c$  is predicted to be 716 K at  $(\text{InAs})_{0.35}(\text{GaAs})_{0.65}$ . Therefore, it is in agreement with the experimental report that phase separation occurs at 623 K [79]. However, the  $(\text{InAs})_x(\text{GaAs})_{1-x}$  has been usually grown over 720 K [88–91], which is above the calculated  $T_c$ . This could be one of the reasons why the phase diagram of this system has not been a crucial issue in experiments. Meanwhile, the  $T_c$  of the phase diagrams reported in theoretical literature varies greatly depending on the literature. Several previous studies calculated  $T_c$  to be 550 K using SQS with an ideal entropy [92]; 750–817 K using the CALPHAD method with experimental liquidus-solidus line [93–96]; and 312–380 K using a Monte Carlo simulation with ideal entropy [97]. Several other studies considered the strain energy and predicted  $T_c$  to be 520 K using GQCA (blue line) [15] and 630 K using CE with 10 DFT samples (red line) [42]. Among those, the red line is the closest to our result. Nonetheless, its spinodal line (dotted red) shows an unusual curve, which is presumably due to the small number of configurations considered. From these results, the consideration of the strain energy induced by the lattice parameter variation is found to be essential to predict the phase diagrams of  $(\text{GaAs})_x(\text{GaSb})_{1-x}$  and  $(\text{InAs})_x(\text{GaAs})_{1-x}$ .

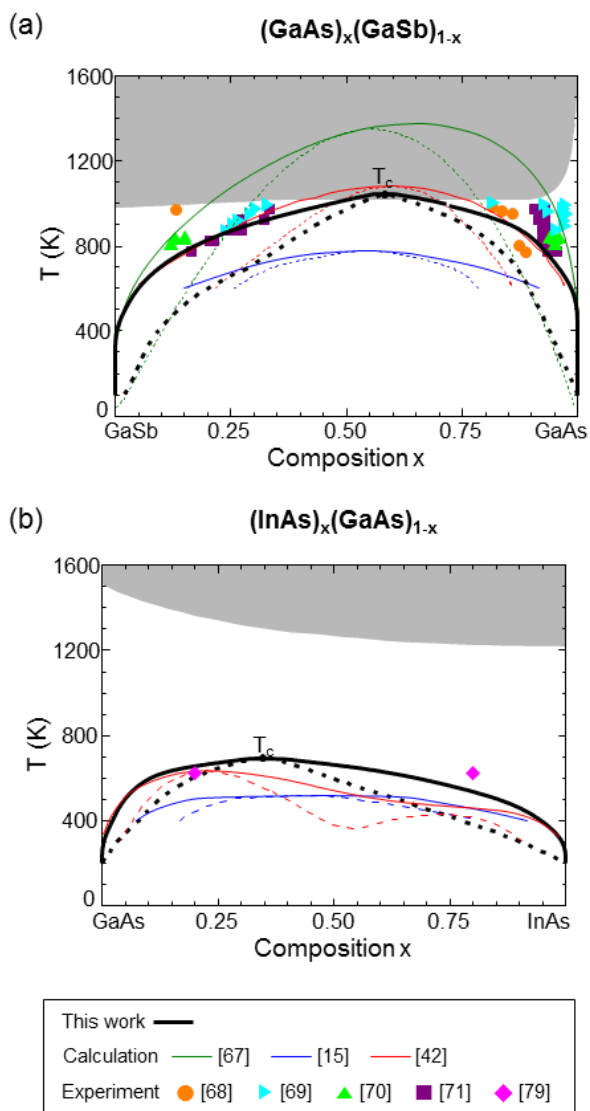


**Figure 4.6** Phase diagrams of (a)  $(\text{GaAs})_x(\text{GaSb})_{1-x}$  and (b)  $(\text{InAs})_x(\text{GaAs})_{1-x}$ .

The black solid and black dotted lines are the calculated binodal and spinodal curves. The gray area is above the experimental solidus line. The colored lines are the previous calculation results, while the colored symbols denote the previous experimental data.

## 4.4. Upper critical solid temperature

To further investigate the general effect of the strain energy on  $T_c$ , the experimental values of  $a_0$ ,  $B_0$ ,  $V_0B_0$  of nine III-V semiconductor materials of zinc-blende structures are shown in Fig. 4.7 (a-c), respectively [86]. Figure 4.7 (d) shows the matrix diagram of  $T_c$  of the various III-V solid solution systems in terms of  $a_0$  ratio and  $B_0$  ratio. These ratios are defined as the larger value divided by the smaller value for  $AC$  and  $BC$ . The maximum value of the  $a_0$  ratio is 1.19 and that of the  $B_0$  ratio is 1.84. On the other hand, the maximum ratio of  $V_0B_0$  is only 1.10 because the  $B_0$  usually decreases as the  $a_0$  increases. This is the reason why  $E_{\sigma}^{strain}$  can be fitted by a single B-M EOS curve irrespective of the configuration and composition in Fig. 4.2. Thus, for a given  $V_0B_0$ , the strain energy in Eq. (3.1) is primarily determined by the relative volume, which is directly affected by the  $a_0$  ratio.

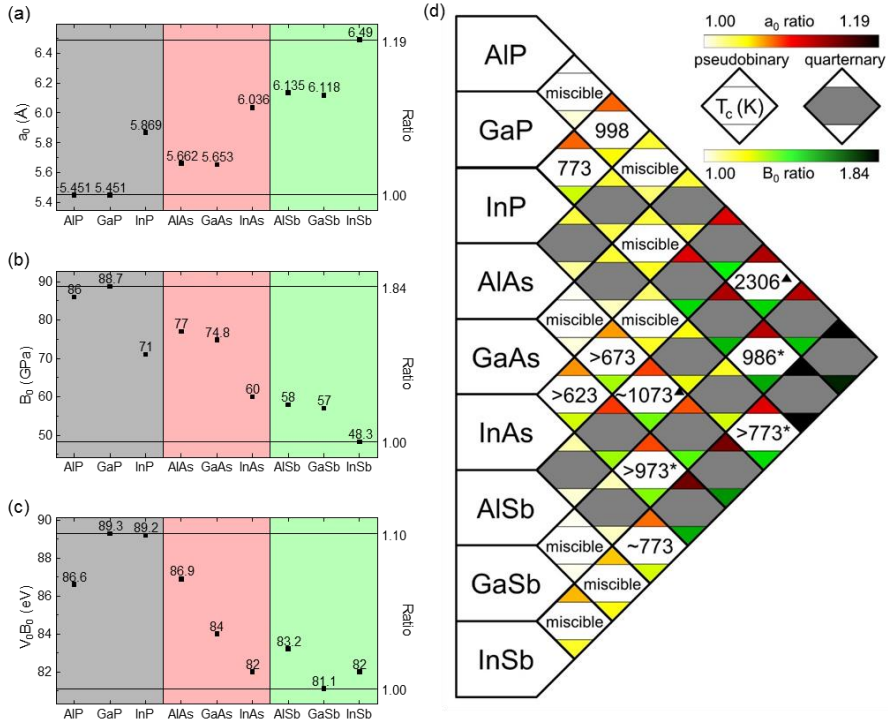


**Figure 4.7** Experimental (a)  $a_0$ , (b)  $B_0$ , and (c)  $V_0 B_0$  of nine III–V zinc-blende structure materials. (d) Matrix diagram of  $T_c$ . The  $a_0$  ratio and  $B_0$  ratio are indicated using red and green scale bars, respectively. The  $T_c$  with an asterisk indicates that the  $T_c$  is above the solidus line. All data are obtained from the experimental literature, except  $T_c$  with a triangle.

There are three types of rhombus cells in Fig. 4.7 (d); a cell with a value, a cell with the word “miscible”, a cell with a gray center. The value at the center of each cell denotes the  $T_c$  of the pseudobinary system which is found in experimental studies [45,71,79,98–101], except for  $(AlP)_x(AlSb)_{1-x}$  and  $(AlAs)_x(AlSb)_{1-x}$ , for which the values were reported through calculations [96]. The calculated  $T_c$  are marked by a small triangle at the right position of the numbers. The asterisk at the same position indicates that  $T_c$  is above the solidus line. The cells for quaternary systems have a gray center and are excluded from this chapter. The “miscible” in the center indicates that the phase separation has not been observed yet. For each cell, the colors of the upper and lower corners denote the  $a_0$  ratio and  $B_0$  ratio which are indicated by red and green scale bars. In general, phase separation does not occur for the cell with pale-colored corners. In contrast,  $T_c$  becomes higher for a cell with darker colored corners. For example, phase separation has not been observed for  $(InSb)_x(GaSb)_{1-x}$  whose  $a_0$  ratio is 1.06 while  $(InAs)_x(GaAs)_{1-x}$  with an  $a_0$  ratio of 1.07 has  $T_c$  above 623 K. Thus, the  $a_0$  ratio of 1.06–1.07 is the critical value that determines the phase separation in these III-V solid solution systems. It is slightly less than 1.08, which is the corresponding value reported in the literature in the 1970s that considered six III-V pseudobinary systems [102]. The reason for such a small difference is that the phase separations of  $(InP)_x(GaP)_{1-x}$  with an  $a_0$  ratio of 1.08 and  $(InAs)_x(GaAs)_{1-x}$  with an  $a_0$  ratio of 1.07 were reported after that work was published. Since the  $a_0$  ratio of all (Al,Ga)-V solid solutions and III-(P,As) solid solutions are smaller than this critical value, phase separation in these systems has not been observed. Due to the similar values of  $V_0B_0$  among

the III-V materials investigated and the opposite tendency in the  $V_0$  ratio to the  $B_0$  ratio, the critical value of the  $B_0$  ratio to determine the phase separation is determined to be  $\sim 1.21$ . The  $a_0$  ratio and  $B_0$  ratio of  $(\text{GaAs})_x(\text{GaSb})_{1-x}$  are 1.08 and 1.31, which implies that phase separation would occur. On the other hand, those of  $(\text{InAs})_x(\text{GaAs})_{1-x}$  are 1.07 and 1.24, which are slightly higher than the critical values, indicating a phase separation at a low temperature. These simple estimations using the  $a_0$  and  $B_0$  ratios are consistent with the calculated phase diagram in Fig. 4.6. The absence of the phase separation with a small  $a_0$  ratio results from the fact that a small variation in  $a_0$  and consequent small range of  $V/V_0$  results in a small absolute value of the third term in Eq. (4.3)

The methodology for *ab initio* thermodynamics suggested in this chapter is expected to be valuable to the fine-tuning of the process and homogeneity of III-V pseudobinary systems, which are required to achieve smaller feature sizes for next-generation transistors. Furthermore, this methodology is also useful for metallurgical alloy systems where strain is an important issue at room temperature and moderate temperatures.

## 4.5. Conclusion

A novel methodology is proposed to efficiently and accurately predict the phase diagrams of alloys applying *ab initio* thermodynamics by taking into account the local strain energy induced by the local compositional fluctuation. The proposed method adopts the CE method in conjunction with DFT

calculations to obtain the freely relaxed energies ( $E_\sigma$ ) of a sufficient number of configurations ( $\sigma$ ). Then, the average energy ( $\overline{\Delta E^{total}}$ ), the mixing Helmholtz energy ( $\Delta F$ ), and the phase diagram are calculated in the framework of the grand canonical ensemble. The local strain energy ( $E_\sigma^{strain}$ ) induced by this local compositional fluctuation is separately calculated and then summed with the mixing energy of the freely relaxed condition ( $\Delta E_\sigma$ ) to calculate the total mixing energy ( $\Delta E_\sigma^{total}$ ). The calculation relies on the fact that the local strain energy is independent of the configuration. The proposed method is applied to  $(\text{GaAs})_x(\text{GaSb})_{1-x}$  and  $(\text{InAs})_x(\text{GaAs})_{1-x}$  in comparison with experimental results. The calculated phase diagram of  $(\text{GaAs})_x(\text{GaSb})_{1-x}$  shows a good agreement with the experiments in the binodal line as well as the upper critical solution temperature ( $T_c$ ). On the other hand, the phase diagram of  $(\text{InAs})_x(\text{GaAs})_{1-x}$  is also predicted and the calculated  $T_c$  is found to be lower than the usual growth temperature in the experiments. Finally, a prediction on  $T_c$  is suggested by an estimation of the strain energy using the ratio of lattice parameters between the nine zinc-blende structure III-V materials composed of combinations of the three cations (Al, Ga, In) and three anions (P, As, Sb), which is relevant to experimental reports.

## 4.6. Appendix

With the mixing Helmholtz free energy ( $\Delta F$ ) in Eq. (2.15), it is obvious that  $\frac{\partial \Delta \mu}{\partial x}$  and  $\frac{\partial Z}{\partial x}$  are needed to differentiate  $\Delta F$ . At first, we focus on

$\frac{\partial Z}{\partial x}$ . When ignoring the strain energy,  $E_{\sigma}^{strain} = 0$  and  $\Delta E_{\sigma}^{total} = \Delta E_{\sigma}$  in Eq.

(2.11). It means that all microstates in the grand canonical ensemble are freely relaxed. Therefore, they have their lattice constants, as shown in the schematic in figure 2 (a). The grand canonical partition function in Eq. (2.8) can be rewritten as follows.

$$Z(x, T) = \sum_{\sigma} \exp\left(\frac{n_{\sigma}\Delta\mu - \Delta E_{\sigma}^{total}}{k_B T}\right) = \sum_{\sigma} \exp\left(\frac{n_{\sigma}\Delta\mu - \Delta E_{\sigma}}{k_B T}\right) \quad (4.6)$$

The mixing energy of the configuration ( $\Delta E_{\sigma}$ ) has no dependency on parameters  $x$  and  $\Delta\mu$ . Thus the grand canonical partition function is relatively simple to be differentiated as follows.

$$\begin{aligned} \frac{\partial Z}{\partial x} &= \frac{\partial Z}{\partial \Delta\mu} \frac{\partial \Delta\mu}{\partial x} = \frac{\partial}{\partial \Delta\mu} \left( \sum_{\sigma} \exp\left(\frac{n_{\sigma}\Delta\mu - \Delta E_{\sigma}}{k_B T}\right) \right) \frac{\partial \Delta\mu}{\partial x} = \frac{\partial \Delta\mu}{\partial x} \sum_{\sigma} \frac{n_{\sigma}}{k_B T} \exp\left(\frac{n_{\sigma}\Delta\mu - \Delta E_{\sigma}}{k_B T}\right) = \\ &= \frac{Z \bar{n}}{k_B T} \frac{\partial \Delta\mu}{\partial x} \end{aligned} \quad (4.7)$$

To calculate  $\frac{\partial \Delta\mu}{\partial x}$ , we calculate  $\frac{\partial x}{\partial \Delta\mu}$  which is the reciprocal of  $\frac{\partial \Delta\mu}{\partial x}$ . By

assigning  $P_{\sigma} = \frac{\exp\left(\frac{n_{\sigma}\Delta\mu - \Delta E_{\sigma}^{total}}{k_B T}\right)}{Z(x, T)}$  in Eq. (2.9) to  $x = \frac{\bar{n}}{N} = \frac{1}{N} \sum_{\sigma} n_{\sigma} P_{\sigma}$  in Eq.

(2.10),  $x$  is transformed to  $\frac{1}{N} \frac{\sum_{\sigma} n_{\sigma} \exp\left(\frac{n_{\sigma}\Delta\mu - \Delta E_{\sigma}^{total}}{k_B T}\right)}{Z}$ .

$$\begin{aligned} \frac{\partial x}{\partial \Delta\mu} &= \frac{\partial \left[ \frac{1}{N} \frac{\sum_{\sigma} n_{\sigma} \exp\left(\frac{n_{\sigma}\Delta\mu - \Delta E_{\sigma}}{k_B T}\right)}{Z} \right]}{\partial \Delta\mu} = \frac{1}{NZ} \sum_{\sigma} \frac{n_{\sigma}^2}{k_B T} \exp\left(\frac{n_{\sigma}\Delta\mu - \Delta E_{\sigma}}{k_B T}\right) - \\ &= \frac{1}{NZ^2} \frac{\partial Z}{\partial \Delta\mu} \sum_{\sigma} n_{\sigma} \exp\left(\frac{n_{\sigma}\Delta\mu - \Delta E_{\sigma}}{k_B T}\right) = \frac{\bar{n}^2}{Nk_B T} - \frac{\bar{n}}{Nk_B T} \bar{n} = \frac{1}{Nk_B T} (\bar{n}^2 - \bar{n}^2) \end{aligned} \quad (4.8)$$

Now, the mixing Helmholtz free energy ignoring the local strain energy is

differentiated twice with Eq. (4.7) and (4.8) as follows.

$$\begin{aligned}\frac{\partial^2 \Delta F}{\partial x^2} &= \frac{\partial}{\partial x} \left( N \Delta \mu + N x \frac{\partial \Delta \mu}{\partial x} - \frac{k_B T}{Z} \frac{\partial Z}{\partial x} \right) = \frac{\partial}{\partial x} \left( N \Delta \mu + \bar{n} \frac{\partial \Delta \mu}{\partial x} - \frac{k_B T}{Z} \frac{Z \bar{n}}{k_B T} \frac{\partial \Delta \mu}{\partial x} \right) = \\ &= \frac{\partial}{\partial x} \left( N \Delta \mu + \bar{n} \frac{\partial \Delta \mu}{\partial x} - \bar{n} \frac{\partial \Delta \mu}{\partial x} \right) = N \frac{\partial \Delta \mu}{\partial x} = N^2 \frac{k_B T}{n^2 - \bar{n}^2} \geq 0\end{aligned}\quad (4.9)$$

Note that the double differentiation of the mixing Helmholtz free energy is always positive or zero because the mean of the square values is always greater than the square of the mean value.

Unlike the case ignoring the strain energy, it is the situation that each microstate in the grand canonical ensemble is constrained by the lattice constant of the average composition  $x$ , as shown in the schematic in Fig. 3.1 (b) and it induces  $E_\sigma^{strain}(x)$  in Eq. (2.11) when local strain energy is considered. Since  $E_\sigma^{strain}$  depends on  $x$ ,  $\Delta E_\sigma^{total}$  has a dependency on  $x$  through  $E_\sigma^{strain}$ . This makes the difference in the derivative of the grand canonical partition function in Eq. (2.8).

$$\begin{aligned}\frac{\partial Z}{\partial x} &= \sum_\sigma \frac{1}{k_B T} \frac{\partial (n_\sigma \Delta \mu - \Delta E_\sigma^{total})}{\partial x} \exp \left( \frac{n_\sigma \Delta \mu - \Delta E_\sigma^{total}}{k_B T} \right) = \sum_\sigma \frac{1}{k_B T} \left( n_\sigma \frac{\partial \Delta \mu}{\partial x} - \right. \\ &\left. \frac{\partial \Delta E_\sigma^{total}}{\partial x} \right) \exp \left( \frac{n_\sigma \Delta \mu - \Delta E_\sigma^{total}}{k_B T} \right) = \frac{Z}{k_B T} \left( \bar{n} \frac{\partial \Delta \mu}{\partial x} - \frac{\partial \bar{E}}{\partial x} \right)\end{aligned}\quad (4.10)$$

where,

$$\frac{\partial \bar{E}}{\partial x} = \sum_\sigma \frac{\partial \Delta E_\sigma^{total}}{\partial x} P_\sigma = \frac{1}{Z} \sum_\sigma \frac{\partial \Delta E_\sigma^{total}}{\partial x} \exp \left( \frac{n_\sigma \Delta \mu - \Delta E_\sigma^{total}}{k_B T} \right)\quad (4.11)$$

The double differential of free energy considering free energy is

$$\frac{\partial^2 \Delta F}{\partial x^2} = \frac{\partial}{\partial x} \left( N \Delta \mu + N x \frac{\partial \Delta \mu}{\partial x} - \frac{k_B T}{Z} \frac{\partial Z}{\partial x} \right) = \frac{\partial}{\partial x} \left( N \Delta \mu + \bar{n} \frac{\partial \Delta \mu}{\partial x} - \frac{k_B T}{Z} \frac{Z}{k_B T} \left( \bar{n} \frac{\partial \Delta \mu}{\partial x} - \right. \right.$$

$$\left. \frac{\partial \bar{E}}{\partial x} \right) = \frac{\partial}{\partial x} \left( N \Delta \mu + \frac{\partial \bar{E}}{\partial x} \right) = N \frac{\partial \Delta \mu}{\partial x} + \frac{\partial}{\partial x} \left( \frac{\partial \bar{E}}{\partial x} \right) \quad (4.12)$$

Both  $\frac{\partial \Delta \mu}{\partial x}$  and  $\frac{\partial}{\partial x} \left( \frac{\partial \bar{E}}{\partial x} \right)$  can be further expanded. At first, we calculated  $\frac{\partial x}{\partial \Delta \mu}$ ,

the reciprocal of  $\frac{\partial \Delta \mu}{\partial x}$ .

$$\begin{aligned} \frac{\partial x}{\partial \Delta \mu} &= \frac{1}{N} \frac{\partial}{\partial \Delta \mu} \left( \frac{\sum_{\sigma} n_{\sigma} \exp\left(\frac{n_{\sigma} \Delta \mu - \Delta E_{\sigma}^{total}}{k_B T}\right)}{Z} \right) = \\ &= \frac{1}{N} \frac{\sum_{\sigma} n_{\sigma} \left( n_{\sigma} - \frac{\partial \Delta E_{\sigma}^{total}}{\partial \Delta \mu} \right) \exp\left(\frac{n_{\sigma} \Delta \mu - \Delta E_{\sigma}^{total}}{k_B T}\right)}{k_B T Z} - \frac{1}{N Z^2} \frac{\partial Z}{\partial \Delta \mu} \sum_{\sigma} n_{\sigma} \exp\left(\frac{n_{\sigma} \Delta \mu - \Delta E_{\sigma}^{total}}{k_B T}\right) = \\ &= \frac{1}{N} \frac{\sum_{\sigma} n_{\sigma} \left( n_{\sigma} - \frac{\partial \Delta E_{\sigma}^{total}}{\partial \Delta \mu} \right) \exp\left(\frac{n_{\sigma} \Delta \mu - \Delta E_{\sigma}^{total}}{k_B T}\right)}{k_B T Z} - \frac{1}{N Z} \frac{\partial \sum_{\sigma} \exp\left(\frac{n_{\sigma} \Delta \mu - \Delta E_{\sigma}^{total}}{k_B T}\right)}{\partial \Delta \mu} = \frac{\bar{n}^2 - n \frac{\partial \bar{E}}{\partial \Delta \mu}}{N k_B T} - \\ &= \frac{\bar{n}}{N k_B T} \left( \bar{n} - \frac{\partial \bar{E}}{\partial \Delta \mu} \right) = \frac{1}{N k_B T} \left( \bar{n}^2 - n \frac{\partial \bar{E}}{\partial \Delta \mu} - \bar{n}^2 + \bar{n} \frac{\partial \bar{E}}{\partial \Delta \mu} \right) = \frac{1}{N k_B T} \left( \bar{n}^2 - n \frac{\partial \bar{E}}{\partial x} \frac{\partial x}{\partial \Delta \mu} - \right. \\ &\left. \bar{n}^2 + \bar{n} \frac{\partial \bar{E}}{\partial x} \frac{\partial x}{\partial \Delta \mu} \right) \quad (4.13) \end{aligned}$$

There is a term for  $\frac{\partial x}{\partial \Delta \mu}$  on both the left and right sides. Because the purpose is

deriving  $\frac{\partial \Delta \mu}{\partial x}$ , the Eq. (4.13) is rearranged to solve for  $\frac{\partial \Delta \mu}{\partial x}$ .

$$\therefore (\bar{n}^2 - \bar{n}^2) \frac{\partial \Delta \mu}{\partial x} = \left( N k_B T + n \frac{\partial \bar{E}}{\partial x} - \bar{n} \frac{\partial \bar{E}}{\partial x} \right) \quad (4.14)$$

The other term,  $\frac{\partial}{\partial x} \left( \frac{\partial \bar{E}}{\partial x} \right)$ , is expanded as follows.

$$\frac{\partial}{\partial x} \left( \frac{\partial \bar{E}}{\partial x} \right) = \frac{\sum_{\sigma} \left( \frac{\partial^2 \Delta E_{\sigma}^{total}}{\partial x^2} + \frac{\partial \Delta E_{\sigma}^{total}}{\partial x} \frac{\partial}{\partial x} \left( \frac{n_{\sigma} \Delta \mu - \Delta E_{\sigma}^{total}}{k_B T} \right) \right) \exp\left(\frac{n_{\sigma} \Delta \mu - \Delta E_{\sigma}^{total}}{k_B T}\right)}{Z} -$$

$$\frac{\sum_{\sigma} \frac{\partial \Delta E_{\sigma}^{total}}{\partial x} \exp\left(\frac{n_{\sigma} \Delta \mu - \Delta E_{\sigma}^{total}}{k_B T}\right)}{Z^2} \frac{\partial Z}{\partial x} =$$

$$\frac{\sum_{\sigma} \left( \frac{\partial^2 \Delta E_{\sigma}^{total}}{\partial x^2} + \frac{1}{k_B T} \frac{\partial \Delta E_{\sigma}^{total}}{\partial x} \left( n_{\sigma} \frac{\partial \Delta \mu}{\partial x} - \frac{\partial \Delta E_{\sigma}^{total}}{\partial x} \right) \right) \exp\left(\frac{n_{\sigma} \Delta \mu - \Delta E_{\sigma}^{total}}{k_B T}\right)}{Z} - \frac{1}{Z} \frac{\partial \bar{E}}{\partial x} \frac{\partial Z}{\partial x} \quad (4.15)$$

By applying Eq. (4.10) into Eq. (4.15),

$$\frac{\partial}{\partial x} \left( \frac{\partial \bar{E}}{\partial x} \right) = \frac{\partial^2 \bar{E}}{\partial x^2} + \frac{1}{k_B T} \left( \overline{n \frac{\partial \bar{E}}{\partial x} \frac{\partial \Delta \mu}{\partial x}} - \overline{\left( \frac{\partial \bar{E}}{\partial x} \right)^2} \right) - \frac{1}{k_B T} \frac{\partial \bar{E}}{\partial x} \left( \bar{n} \frac{\partial \Delta \mu}{\partial x} - \frac{\partial \bar{E}}{\partial x} \right) = \frac{\partial^2 \bar{E}}{\partial x^2} +$$

$$\frac{1}{k_B T} \frac{\partial \Delta \mu}{\partial x} \left( \overline{n \frac{\partial \bar{E}}{\partial x}} - \bar{n} \frac{\partial \bar{E}}{\partial x} \right) + \frac{1}{k_B T} \left( \overline{\frac{\partial \bar{E}}{\partial x}^2} - \overline{\left( \frac{\partial \bar{E}}{\partial x} \right)^2} \right) \quad (4.16)$$

, where

$$\frac{\partial^2 \bar{E}}{\partial x^2} = \frac{1}{Z} \sum_{\sigma} \frac{\partial^2 \Delta E_{\sigma}^{total}}{\partial x^2} \exp\left(\frac{n_{\sigma} \Delta \mu - \Delta E_{\sigma}^{total}}{k_B T}\right) \quad (4.17)$$

$$\overline{\left( \frac{\partial \bar{E}}{\partial x} \right)^2} = \frac{1}{Z} \sum_{\sigma} \left( \frac{\partial \Delta E_{\sigma}^{total}}{\partial x} \right)^2 \exp\left(\frac{n_{\sigma} \Delta \mu - \Delta E_{\sigma}^{total}}{k_B T}\right) \quad (4.18)$$

$$\bar{n} \frac{\partial \bar{E}}{\partial x} = \frac{1}{Z} \sum_{\sigma} n_{\sigma} \frac{\partial \Delta E_{\sigma}^{total}}{\partial x} \exp\left(\frac{n_{\sigma} \Delta \mu - \Delta E_{\sigma}^{total}}{k_B T}\right) \quad (4.19)$$

Applying Eq. (4.14) and Eq. (4.16) to Eq. (4.12) yields the equation:

$$\frac{\partial^2 \Delta F}{\partial x^2} = N \frac{\partial \Delta \mu}{\partial x} + \frac{\partial}{\partial x} \left( \frac{\partial \bar{E}}{\partial x} \right) = \frac{1}{k_B T} \frac{\partial \Delta \mu}{\partial x} \left( N k_B T + \overline{n \frac{\partial \bar{E}}{\partial x}} - \bar{n} \frac{\partial \bar{E}}{\partial x} \right) + \frac{\partial^2 \bar{E}}{\partial x^2} +$$

$$\frac{1}{k_B T} \left( \overline{\frac{\partial \bar{E}}{\partial x}^2} - \overline{\left( \frac{\partial \bar{E}}{\partial x} \right)^2} \right) = \frac{1}{k_B T} (\bar{n}^2 - \bar{n}^2) \left( \frac{\partial \Delta \mu}{\partial x} \right)^2 + \frac{\partial^2 \bar{E}}{\partial x^2} + \frac{1}{k_B T} \left( \overline{\frac{\partial \bar{E}}{\partial x}^2} - \overline{\left( \frac{\partial \bar{E}}{\partial x} \right)^2} \right) \quad (4.20)$$

# CHAPTER 5

## BANDGAP OF

## III-V SEMICONDUCTOR SOLID SOLUTION

---

### 5.1. Introduction

The pseudobinary III-V compound semiconductor Ga(As,Sb) has been widely used as a semiconductor channel and as an optoelectronic material with high carrier mobilities, high photon absorption coefficients, and easy tunability of the lattice constant and bandgap ( $E_g$ ) [61,62,64]. In zinc-blende structured Ga(As,Sb), both As and Sb atoms occupy the anion sites, resulting in a tremendous number of atomic arrangements, called configurations. Various properties, such as atomistic energy [12], Curie temperature [103], dielectric constant [14], and piezoelectric constants [56] depend on the atomic configuration, as does the bandgap [104,105]. The bandgap is the most crucial material parameter that determines most of the critical device's performance,

so controlling it is of utmost importance in the field. The bandgap of  $\text{GaAs}_x\text{Sb}_{1-x}$  has been adjusted mainly by tuning the composition ( $x$ ), but the achievable bandgap has been limited to values ranging from 0.68 to 1.43 eV [61,106]. Configuration could be another crucial knob by which to control the bandgap. However, it has been studied less than composition control due to the difficulties of controlling and characterizing configuration in experiments. Nonetheless, a few recent studies have demonstrated the possibility of bandgap engineering through configuration control: III-V pseudobinary superlattice structures using atomic layer deposition (ALD) [3,4] and ordered  $\text{Ga}(\text{As},\text{Sb})$  using Bi catalyst [7].

The methodology in chapter 3 could be expanded to other configuration-dependent properties such as bandgap although chapter 4 focuses on evaluating the energetics. The cluster expansion is usually applied to examine the energy. However, many studies have used the cluster expansion method to study the bandgap [54–58].

In this chapter, the composition- and configuration-dependent bandgaps of  $\text{Ga}(\text{As},\text{Sb})$  are examined. The bandgap and energy of numerous configurations are calculated using the DFT and CE methods. The relationship between the bandgaps and the energetic stability of configurations is characterized by the ECIs and confirmed through correlations with the short-range order parameters. Also, the bandgaps and energetics of individual configurations are combined within the grand canonical ensemble, with consideration for the compositional fluctuation, to examine the average

bandgap for a given composition and temperature. Bandgap engineering solely by compositional tuning in Ga(As,Sb) is found to be implausible due to limited tunability. The significant dependence of bandgaps on the atomic configuration shown in this chapter implies an unprecedented method of controlling the properties of multi-component materials.

## 5.2. Computational details

The calculation methods in this chapter are similar to chapter 4. Thus, this section focuses on the differences from section 4.2.

### 5.2.1 Density functional theory

Due to the well-known bandgap underestimation of LDA and PBE, DFT calculation was performed using the Heyd-Scuseria-Ernzerhof (HSE) hybrid functional [107] to calculate bandgaps. For Ga(As,Sb) bandgap calculation, spin-orbit coupling (SOC) was included to calculate Ga(As,Sb) bandgaps accurately [108,109], and the Hartree-Fock mixing parameter  $\alpha$  and screening parameter  $w$  were adjusted to match the experimental bandgap [110]. However, no parameter set was found to reproduce the experimental bandgaps of GaAs and GaSb simultaneously. Because this chapter focused on the GaSb-rich region for the intrinsic p-type semiconductor and the appropriate junction barrier [111–113],  $\alpha$  and  $w$  were set as 0.27 and  $0.2 \text{ \AA}^{-1}$  to preferentially match the experimental bandgap of GaSb. The  $\Gamma$ -centered grid scheme was used with

4×4×4 k-points for the zinc-blende unit cell. The cutoff energy for the plane-wave basis function was 500 eV. The  $\Delta E_\sigma$  and  $E_{g,\sigma}$  were calculated for 30 configurations in a 2×2×2 supercell of GaAs<sub>x</sub>Sb<sub>1-x</sub>. Strain energies were calculated by changing  $V/V_0$  for randomly selected configurations, which were at least three for each composition at regular intervals in the entire composition. The calculated strain energies were fitted to Birch-Murnaghan EOS in Eq. (3.1).

### 5.2.2 Cluster expansion

The cluster expansion (CE) method was performed using the LACOS package [84]. The CE method efficiently calculates the configuration-dependent properties of numerous configurations without sacrificing accuracy. In the CE method, the particular property of a configuration is described as the sum of contributions from various clusters, where a cluster refers to a group of interacting atoms. A cluster composed of k atoms is called a k-site cluster. The contribution of each cluster is called the effective cluster interaction coefficient (ECI). Using the properties of configurations calculated by DFT as training data, the ECI of each cluster is iteratively evaluated. Then, the ECIs enable the prediction of the properties of any arbitrary configurations without expensive electronic calculations. The orthogonal matching pursuit method implemented in the LACOS package was used to calculate ECI for the database [84]. After obtaining ECI, the properties of 10,000 configurations for every possible composition at interval 0.03125 (= 1/32) in the 2×2×2 supercell were evaluated, for a total of 330,000 configurations. The properties of configurations were

used to obtain the average properties using Eq. (2.7).

### 5.2.2 Short-range order parameters and correlations

The degree of ordering was quantified using the Warren-Cowley short-range order (SRO) parameter [114]. The SRO parameter of the  $m^{\text{th}}$  2-site cluster,  $\text{SRO}_{(2,m)}$ , in a particular configuration is defined as

$$\text{SRO}_{(2,m)} = 1 - \frac{P_{AB}}{x_{\sigma}(1-x_{\sigma})} \quad (5.1)$$

, where  $P_{AB}$  denotes the probability that the first site is occupied by atom A (As atom), and the second site is occupied by atom B (Sb atom) for a pair of sites forming the (2,m) cluster. The possible range of  $\text{SRO}_{(2,m)}$  is  $-1 \sim 1$  by Eq. (5.1). The geometry of the cell,  $x_{\sigma}$ , and cluster (2,m) further limits the possible  $\text{SRO}_{(2,m)}$  range. A positive SRO indicates clustering of atoms of the same kind, whereas a negative SRO indicates a pairing of different atoms. An SRO of zero describes a completely random state. It should be noted that  $\text{SRO}_{(2,m)}$  is related to  $\overline{\prod_{\{i\} \in (2,m)} \theta(\sigma_i)}$  in Eq. (2.6), as follows:

$$\overline{\prod_{\{i\} \in (2,m)} \theta(\sigma_i)} = 1 + 4x_{\sigma}(1-x_{\sigma})(\text{SRO}_{(2,m)} - 1) \quad (5.2)$$

The  $\text{SRO}_{(2,m)}$  for 10,000 configurations were calculated for  $x_{\sigma} = 0.25, 0.5,$  and  $0.75$ . Then, correlations between the pairs of  $E_{g,\sigma}$ ,  $\Delta E_{\sigma}$ , and  $\text{SRO}_{(2,m)}$  were measured by Pearson correlation coefficient [115].

### 5.3. Bandgaps and energies of configurations

$E_{g,\sigma}$ ,  $\Delta E_\sigma$  and  $E_\sigma^{strain}$  are required to predict  $\overline{E_g}$  using the grand canonical partition function. To achieve CE-based predictions of  $E_{g,\sigma}$  and  $\Delta E_\sigma$ , as derived in Eq. (2.6),  $J_{k,m}^{Eg}$  and  $J_{k,m}^{\Delta E}$  are calculated based on DFT results, as shown in Fig. 5.1 (a) and (b), respectively. The corresponding clusters are presented in Fig. 5.1 (c). They are relevant to the low cross-validation (CV) score for both  $E_g$  (18 meV) and  $\Delta E$  (1 meV/atom), which are less than 3% of their variation ranges ( $> 1$  eV for  $E_g$  and  $> 40$  meV/atom for  $\Delta E$ ). For both  $E_g$  and  $\Delta E$  in Fig. 5.1, the magnitude of ECIs of 2-site clusters are larger than those of many-body clusters except  $J_{2,3}^{Eg}$ . Thus, the effects of 2-site clusters are more dominant than those of many-body clusters on  $E_{g,\sigma}$  and  $\Delta E_\sigma$ , although  $\overline{\prod_{\{i\} \in (k,m)} \theta(\sigma_i)}$ , which is multiplied by ECIs in Eq. (2.6), is needed to quantify the exact contribution of each cluster. This tendency is also consistent with the  $J_{k,m}^{\Delta E}$  values calculated using local density approximation (LDA) in Fig. 4.1.

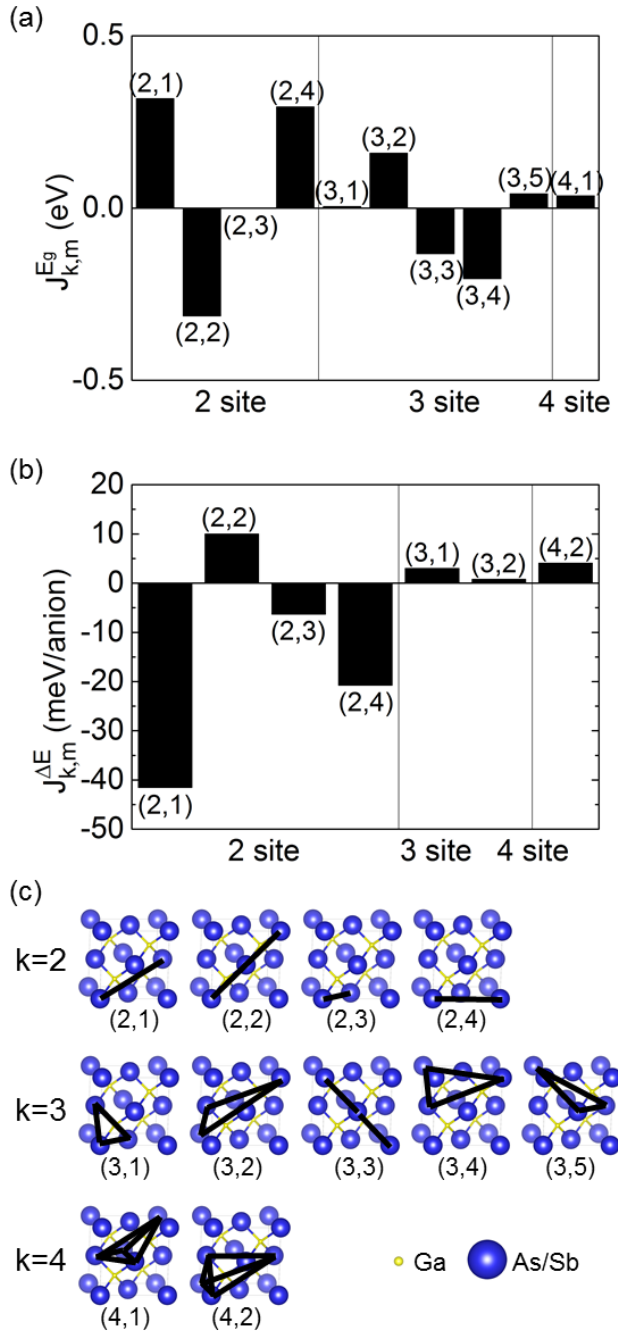


**Figure 5.1** Calculated ECIs and corresponding clusters. ECIs of (a) bandgap, (b) mixing energy of  $\text{GaAs}_x\text{Sb}_{1-x}$ , and (c) corresponding clusters. The set of numbers (k,m) denotes m-th k-site cluster.

To predict  $\overline{E_g}$  in the framework of the grand canonical partition function according to Eq. (2.7) and (3.4), both  $E_{g,\sigma}$  and  $\Delta E_\sigma$  should be calculated for an individual  $\sigma$ . With the ECIs obtained in Fig. 5.1 (a) and (b),  $E_{g,\sigma}$  and  $\Delta E_\sigma$  for 330,000 configurations are calculated, as shown in Fig. 5.2 (a). The x- and y- coordinates of each data point denote the set of  $\Delta E_\sigma/2N$  and  $E_{g,\sigma}$  for each configuration. Furthermore, the color of each dot indicates the composition from red for GaSb to violet for GaAs. On the other hand, the circles with a black edge indicate the results obtained by DFT calculations, where the inner color of each circle indicates the composition.  $\Delta E_\sigma$  and  $E_{g,\sigma}$  vary with different configurations even in a given composition. For GaAs<sub>0.5</sub>Sb<sub>0.5</sub>, which is represented by green dots, the chalcopyrite structure in Fig. 5.2 (b) interestingly has the highest  $E_{g,\sigma}$  of 0.93 eV and the lowest  $\Delta E_\sigma/2N$  of 16 meV/atom, while the CuPt structure in Fig. 5.2 (c) has the lowest  $E_{g,\sigma}$  of 0.02 eV and the highest  $\Delta E_\sigma/2N$  of 44 meV/atom. Even without the extreme example of the specific configurations, it is clear that a configuration with lower energy has a higher bandgap for a given composition, and this tendency is observed in all composition ranges. This tendency can be explained by the ECIs in Fig. 5.1, where the signs of  $J_{k,m}^{Eg}$  and  $J_{k,m}^{\Delta E}$  are opposite for all 2-site clusters. The inverse relationship between the bandgap and energetic stability is consistent with the general feature that a stable structure with a strong bond has a higher bandgap. In other words, the inverse or proportional relationship between a particular property and energetic stability can be estimated based on the sign and magnitude of ECIs. For

example, from the ECIs of both  $E_g$  and  $\Delta E$  for other II-VI and III-V compounds in the literature, such as (Cd,Zn)S, Zn(O,S), (GaN)<sub>1-x</sub>(ZnO)<sub>x</sub> [52], and GaInP<sub>2</sub> [116], the inverse relationship between the bandgap and energetic stability can be deduced although the literature did not focus on the sign of dominant clusters' ECI and the relationship between  $E_g$  and  $\Delta E$ .

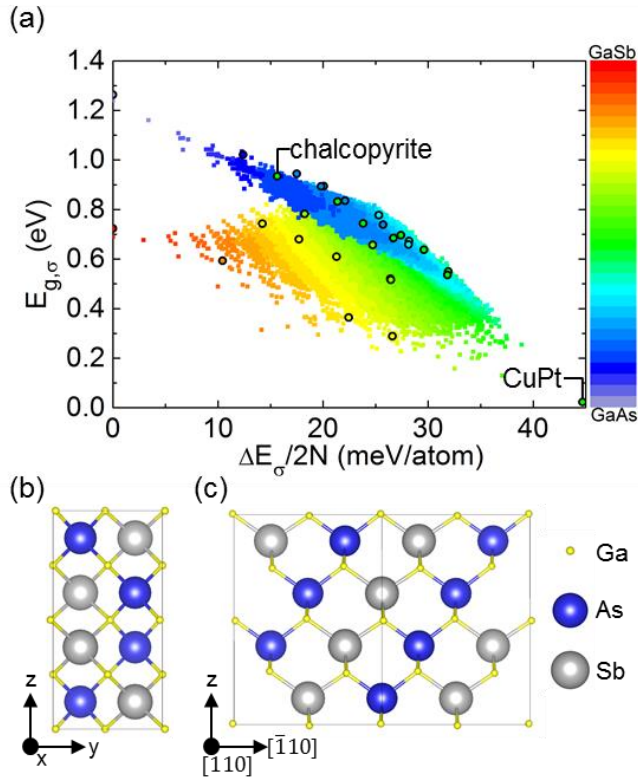


**Figure 5.2** Configuration-dependent bandgap. (a) Bandgap versus mixing energy graph. Crystal structure of (b) chalcopyrite and (c) CuPt. Each point represents a configuration, and the color of each point denotes the composition  $x$ . The open black circles represent the results obtained by DFT calculations.  $2N$  is the total number of atoms in a  $2 \times 2 \times 2$  supercell.

The  $SRO_{(2,m)}$  are calculated for more quantitative analysis. The calculated  $SRO_{(2,m)}$  is plotted in Fig. 5.3 as a function of  $E_{g,\sigma}$  and  $\Delta E_\sigma$ . Table 5.1 represents the Pearson correlation coefficients between the pairs of properties ( $E_{g,\sigma}$  and  $\Delta E_\sigma$ ) and  $SRO_{(2,m)}$  at  $x_\sigma = 0.25, 0.5,$  and  $0.75$ . The correlation does not change significantly with  $x_\sigma$ . The correlation between  $E_{g,\sigma}$  and  $\Delta E_\sigma$  shows a strong negative linear relationship, which is consistent with the relationship between  $E_{g,\sigma}$  and  $\Delta E_\sigma$  shown in Fig. 5.2 (a). In addition, the correlation between an  $SRO_{(2,m)}$  and a property has the same sign as the ECI of the (2,m) cluster in Fig. 5.1. This enhances the inference that the relationship between properties can be deduced from the signs of ECIs. It is also pointed out that the correlations between  $SRO_{(2,1)}$  and the examined properties are not apparent despite the large  $J_{2,1}^{Eg}$ , and  $J_{2,1}^{\Delta E}$ . In contrast,  $SRO_{(2,2)}$  shows a stark negative (positive) relationship with  $E_{g,\sigma}$  ( $\Delta E_\sigma$ ), and  $SRO_{(2,4)}$  shows a clear positive (negative) relationship with  $E_{g,\sigma}$  ( $\Delta E_\sigma$ ). This is because the possible ranges of  $SRO_{(2,2)}$  and  $SRO_{(2,4)}$  are more than twice that of  $SRO_{(2,1)}$  (see the unshaded area in Fig. 5.3). According to Eq. (5.2), the limited range of  $SRO_{(2,m)}$  indicates the confined range of  $\overline{\prod_{i \in (2,m)} \theta(\sigma_i)}$ , which is multiplied by ECIs in Eq. (2.6). Thus, the correlations of properties with  $SRO_{(2,1)}$  become weaker than the correlations of properties with  $SRO_{(2,2)}$  and  $SRO_{(2,4)}$ .

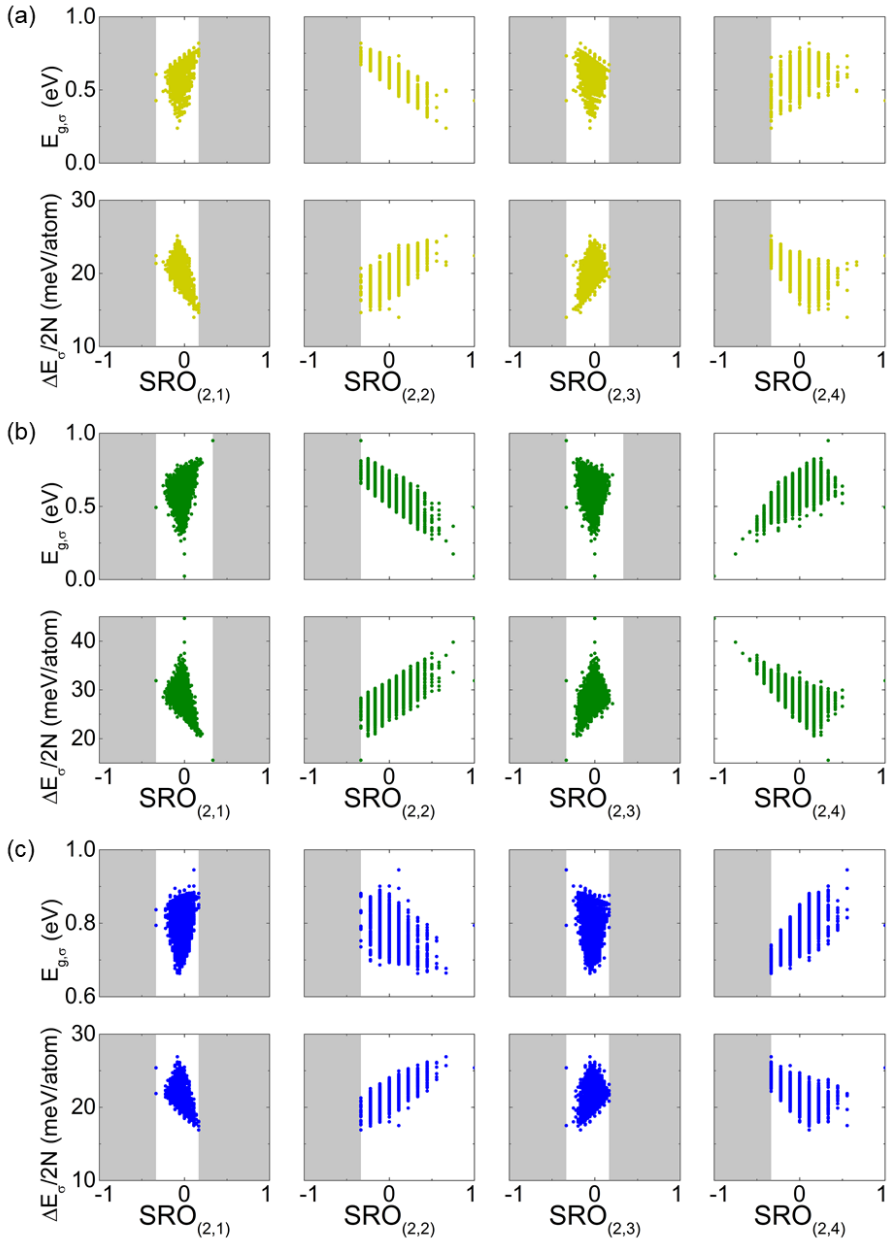


**Figure 5.3**  $E_{g,\sigma}$  (upper panel) and  $\Delta E_{\sigma}$  (lower panel) of 10,000 configurations as a function of  $SRO_{(2,m)}$ .  $x_{\sigma} =$  (a) 0.25 (yellow), (b) 0.5 (green), and (c) 0.75 (blue) The shaded area indicates the forbidden range of  $SRO_{(2,m)}$ .

**Table 5.1** Correlations between pairs of bandgap, energy, and  $\text{SRO}_{(2,m)}$  of 10,000 configurations at  $x_\sigma = 0.25, 0.5,$  and  $0.75$ .

$x_\sigma=0.25$	$E_{g,\sigma}$	$\Delta E_\sigma$	$\text{SRO}_{(2,1)}$	$\text{SRO}_{(2,2)}$	$\text{SRO}_{(2,3)}$	$\text{SRO}_{(2,4)}$
$E_{g,\sigma}$	1.000	-0.844	0.309	-0.853	-0.163	0.471
$\Delta E_\sigma$		1.000	-0.549	0.609	0.485	-0.579
$\text{SRO}_{(2,1)}$			1.000	-0.267	-0.627	-0.271
$\text{SRO}_{(2,2)}$				1.000	-0.261	-0.099
$\text{SRO}_{(2,3)}$					1.000	-0.254
$\text{SRO}_{(2,4)}$						1.000
$x_\sigma=0.5$	$E_{g,\sigma}$	$\Delta E_\sigma$	$\text{SRO}_{(2,1)}$	$\text{SRO}_{(2,2)}$	$\text{SRO}_{(2,3)}$	$\text{SRO}_{(2,4)}$
$E_{g,\sigma}$	1.000	-0.946	0.295	-0.804	-0.174	0.632
$\Delta E_\sigma$		1.000	-0.470	0.662	0.410	-0.648
$\text{SRO}_{(2,1)}$			1.000	-0.262	-0.630	-0.237
$\text{SRO}_{(2,2)}$				1.000	-0.247	-0.137
$\text{SRO}_{(2,3)}$					1.000	-0.274
$\text{SRO}_{(2,4)}$						1.000
$x_\sigma=0.75$	$E_{g,\sigma}$	$\Delta E_\sigma$	$\text{SRO}_{(2,1)}$	$\text{SRO}_{(2,2)}$	$\text{SRO}_{(2,3)}$	$\text{SRO}_{(2,4)}$
$E_{g,\sigma}$	1.000	-0.818	0.148	-0.501	-0.082	0.712
$\Delta E_\sigma$		1.000	-0.470	0.705	0.351	-0.579
$\text{SRO}_{(2,1)}$			1.000	-0.250	-0.628	-0.267
$\text{SRO}_{(2,2)}$				1.000	-0.276	-0.097
$\text{SRO}_{(2,3)}$					1.000	-0.259
$\text{SRO}_{(2,4)}$						1.000

To analyze the relationship between the configuration and  $E_{g,\sigma}$ , on the other hand, the partial density of states (PDOS) of several configurations including GaSb, chalcopyrite structure at  $\text{GaAs}_{0.5}\text{Sb}_{0.5}$ , CuPt structure at  $\text{GaAs}_{0.5}\text{Sb}_{0.5}$ , and GaAs are also calculated in Fig. 5.4. Except for the variations in  $E_g$ , the PDOSs do not show any apparent variations according to composition and configuration. This is presumably because the effects of composition and configuration on PDOSs decrease drastically with increasing atomic distance, and the distance between significant pairs of atoms in  $E_g$  are much farther than the nearest neighbor distance. For example, (2,2) cluster is aligned along the  $\langle 110 \rangle$  direction, and its atomic distance is 3.3 times the nearest neighbor distance, while (2,4) cluster is aligned along the  $\langle 100 \rangle$  direction, and its atomic distance is 2.3 times the nearest neighbor distance, respectively. To check whether the notable low  $E_g$  of CuPt structure is induced by local strain,  $E_g$  of GaAs and GaSb with the same bonding environment as the cations in the CuPt structure are calculated. The  $E_g$  of strained GaAs is 0.58 eV and that of strained GaSb is calculated as 0.85 eV. Though the  $E_g$  under strain is much lower than  $E_g$  of the free relaxed system for both GaAs and GaSb, a bandgap as low as CuPt cannot be achieved without mixing GaAs and GaSb.

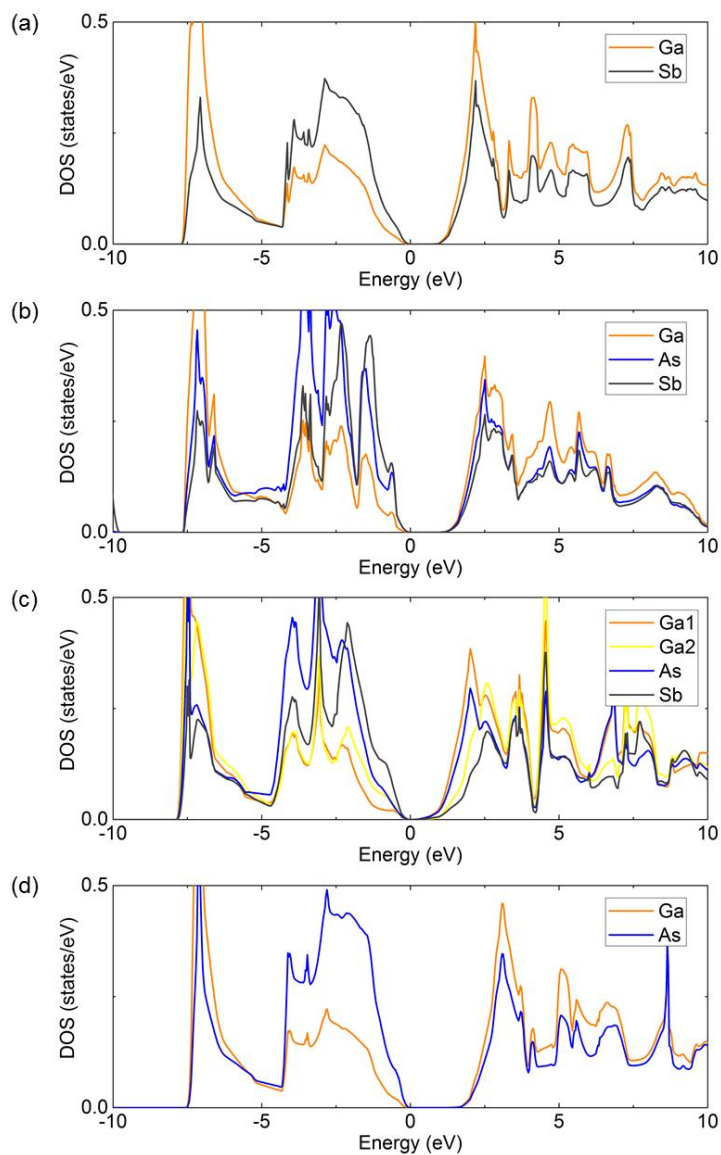


**Figure 5.4** Partial density of states (DOS) projected on atoms. (a) GaSb, (b) chalcopyrite structure, (c) CuPt structure, and (d) GaAs. Zero energy denotes the Fermi level. For CuPt structure, Ga1 indicates Ga atom having three bonds with As atoms and one bond with Sb atom, and Ga2 indicates Ga atom having one bond with As atom and three bonds with Sb atoms.

## 5.4. Average bandgap of Ga(As,Sb)

$E_{g,\sigma}$  and  $\Delta E_\sigma$  are calculated in the previous section. The last component for calculating  $\overline{E_g}$ , the  $E^{strain}$  of  $\text{GaAs}_x\text{Sb}_{1-x}$ , is also calculated as a function of  $V/V_0$  in Fig. 5.5.  $E^{strain}$  is described by the Birch-Murnaghan equation of state, as in the previous chapter. Whereas the previous chapter uses the LDA functional to demonstrate that the Birch-Murnaghan equation of state reproduces  $E^{strain}$  of Ga(As,Sb) in Fig. 4.2,  $E^{strain}$  calculated using HSE+SOC also well fitted by Birch-Murnaghan equation of state as shown in Fig. 5.5. From the fitting,  $B_0$  values are calculated as 70.8 GPa for GaAs and 56.8 GPa for GaSb. These  $B_0$  values show feasible agreements with the experimental  $B_0$  values, 74.8 GPa for GaAs and 57.0 GPa for GaSb [86], which means this calculation has high reliability.

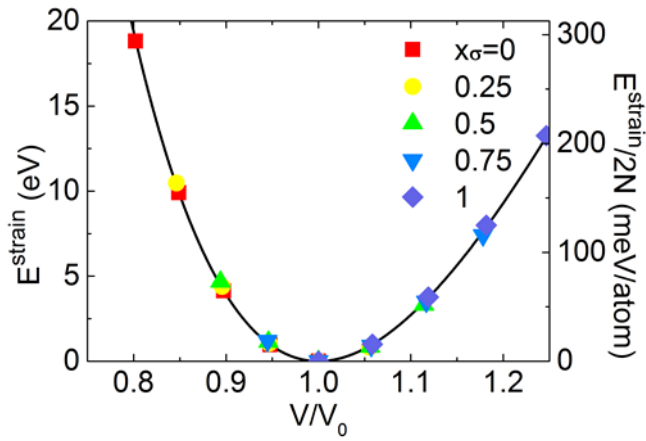


**Figure 5.5** Strain energy as a function of the relative volume  $V/V_0$ . The symbols denote the unit cell of  $\text{GaAs}_x\text{Sb}_{1-x}$  with various relative volumes, and the black curve is fitted to the Birch-Murnaghan equation of state.

It should be noted that the explicit effect of  $E^{strain}$  on an individual  $E_{g,\sigma}$  is not considered; rather, the implicit effect of  $E^{strain}$  on  $\overline{E_g}$  is included when calculating the probability that a configuration will occur, as shown in Eq. (2.9) and (2.11). Figure 5.6 (a), (b), and (c) show the probability mass function (PMF) in systems with the average compositions  $x = 0.1, 0.5,$  and  $0.9$  at 300, 600, and 900 K, respectively. The mean (average) value of  $x_\sigma$  is equal to  $x$  regardless of temperature. The difference between  $x$  and the mode of each PMF is 0.03125 ( $= 1/32$ ) or less. Mode is a term in statistics that refers most frequent event which corresponds to the  $x_\sigma$  with the highest value. Figure 5.6 (d) represents the sum of the PMF in the shaded regions of Fig. 5.6 (a–c), where the deviation of  $x_\sigma$  from  $x$  is 0.1 or less. In other words, the compositions of most configurations are concentrated near  $x$ . This is because the  $E^{strain}/2N$  in the right y-axis of Fig. 5.5 is higher than  $\Delta E_\sigma/2N$  in the x-axis of Fig. 5.2 by approximately one order of magnitude; thus, it leads most of  $x_\sigma$  to approach  $x$ , lowering the  $E^{strain}$  in  $\Delta E_\sigma^{total}$ . As the temperature increases, the peaks in Fig. 5.6 (a–c) become broader, and the sum of the probability in the shaded region decreases at each  $x$  value, as shown in Fig. 5.6 (d). Figure 5.6 (e) shows  $E_{g,\sigma}$  of the unit cell configurations calculated using DFT when  $x - x_\sigma$  are -0.1, 0, and 0.1, which correspond to  $\sim 1.02, 1,$  and  $\sim 0.98$  of  $V/V_0$ , respectively. This shows that the maximum change of  $E_{g,\sigma}$  for this variation in  $V/V_0$  is less than 0.17 eV and that  $E_{g,\sigma}$  decreases if  $x - x_\sigma$  is negative and vice versa. Therefore, in the  $\overline{E_g}$  calculation, the variation of  $E_{g,\sigma}$  by the local

strain induced by the local compositional fluctuation would compensate for each other. As a result, the change in  $\overline{E_g}$  caused by the local strain is much smaller than that caused by the configuration. Therefore, the change in  $\overline{E_g}$  by the local strain was ignored.

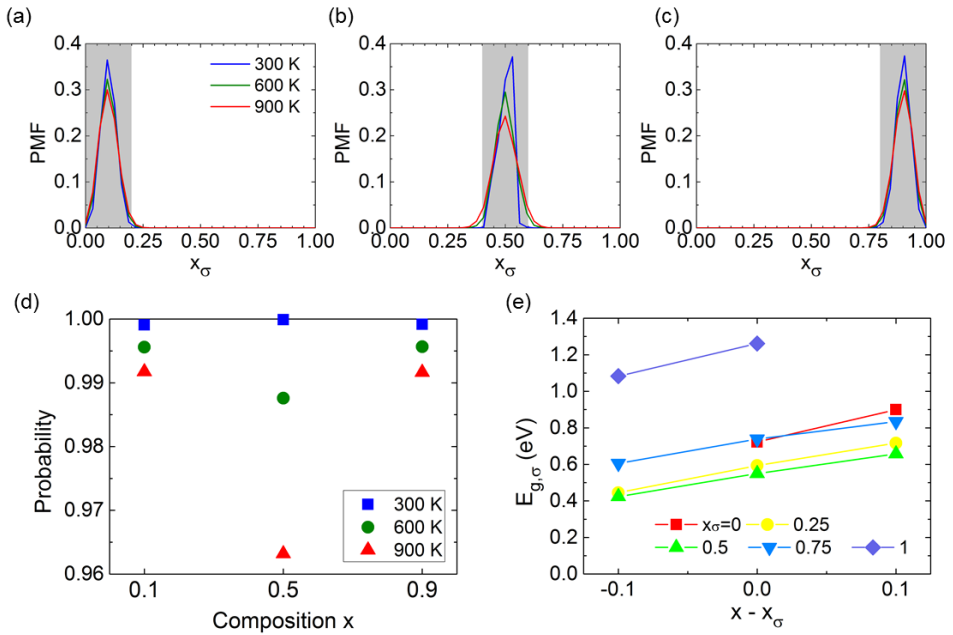


**Figure 5.6** Probability mass function (PMF) of  $x_\sigma$  and bandgap under strain. PMFs at 300, 600, and 900 K for (a) GaAs<sub>0.1</sub>Sb<sub>0.9</sub>, (b) GaAs<sub>0.5</sub>Sb<sub>0.5</sub>, and (c) GaAs<sub>0.9</sub>Sb<sub>0.1</sub>. (d) Sum of the PMFs in the shaded area where the deviation of  $x_\sigma$  from  $x$  is less than 0.1. (e) Bandgap of a hydrostatically strained unit cell with a local composition  $x_\sigma = 0, 0.25, 0.5, 0.75, \text{ and } 1$  as a function of  $x - x_\sigma$ .

Figure 5.7 shows the individual  $E_{g,\sigma}$  values and the calculated  $\overline{E}_g$  at 300, 600, and 900 K as a function of the average composition  $x$  of  $\text{GaAs}_x\text{Sb}_{1-x}$ . Each color bar indicates the 10,000 calculated values of  $E_{g,\sigma}$  for each composition using the CE method, showing a wide range of bandgap variation, such as  $\sim 0.9$  eV at  $x = 0.5$ . On the other hand,  $\overline{E}_g$  at each temperature was predicted using Eq. (2.9) and presented with solid lines. The dashed line, on the other hand, denotes the experimental bandgap [106,117]. In the GaSb-rich composition, the calculated  $\overline{E}_g$  values at 600 K and 900 K are well matched with the experimental bandgap, reproducing the well-known bandgap bowing in III-V solid solutions [106,117]. However, the discrepancy between the calculated and experimental values becomes larger as the composition becomes closer to GaAs. This can be attributed to the HSE parameters, which were adjusted to match the experimental bandgap of GaSb, as discussed in section 2.1. According to Eq. (2.9),  $P_\sigma$  of a configuration with low energy is high when the temperature is low. However, the difference between  $P_\sigma$  of configurations with different energy decreases as temperature increases. This fact, combined with the inverse relationship between  $E_{g,\sigma}$  and  $\Delta E_\sigma$  discussed in Fig. 5.2, means that  $\overline{E}_g$  at a lower temperature is higher than  $\overline{E}_g$  at a higher temperature, which implies that the bandgap bowing depends on the deposition or annealing temperature. This temperature dependence of bandgap is different from the temperature dependence of bandgap caused by the lattice thermal expansion and electron-phonon interaction [118], which can be applied to unary materials and ordered compound materials, such as Si, Ge, GaAs, and GaSb.

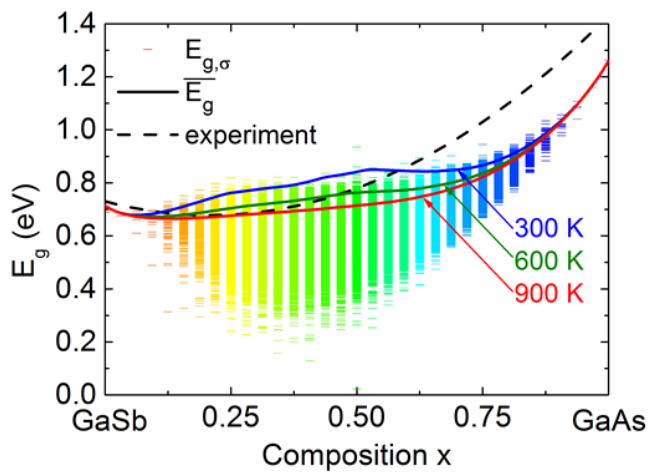


**Figure 5.7** Bandgap of  $\text{GaAs}_x\text{Sb}_{1-x}$  as a function of composition  $x$ . Bar symbols represent the bandgap of each configuration calculated using the cluster expansion method. The solid line denotes the calculated average bandgap at various temperatures, and the dashed line denotes the conventional experimental bandgap.

The calculation results in this chapter reveal that the bandgap engineering in Ga(As,Sb) solid solution by composition tuning appears unlikely to be successful because the bandgap varies significantly depending on the configuration, even within a given composition. In addition, phase separation, which occurs in various III-V materials including Ga(As,Sb) [12,69], makes bandgap engineering by composition tuning even more challenging. However, it may be possible to obtain a specific configuration by manipulating the experimental method and conditions [7,119–121]. Therefore, once a method to obtain a specific configuration is established, the tunable bandgap range will extend beyond the range obtained by controlling composition alone. For example,  $E_{g,\sigma}$  of a (111)-oriented superlattice is expected to be lower than the experimental bandgap for a given composition because this structure has a high  $SRO_{(2,2)}$  decreasing  $E_{g,\sigma}$ , and a low  $SRO_{(2,4)}$  increasing  $E_{g,\sigma}$ . This chapter provides the community with an efficient and accurate methodology to predict the properties of solid solution systems by taking into account innumerable configurations through the use of density functional theory calculations and cluster expansion, which will contribute greatly to the versatile design of properties.

## 5.5. Conclusion

The bandgap ( $E_g$ ), the mixing energy ( $\Delta E$ ) of Ga(As,Sb), and their relationship are examined in this chapter.  $E_{g,\sigma}$  and  $\Delta E_\sigma$  of 330,000 configurations are calculated by implementing a cluster expansion method with

DFT calculations to overcome the high computational cost of accurate DFT calculations. In all compositions,  $E_g$  and  $\Delta E$  vary depending on the configuration, and a configuration with a higher bandgap has lower mixing energy and vice versa. This inverse relationship between  $E_{g,\sigma}$  and  $\Delta E_\sigma$  of Ga(As,Sb) can be inferred from the sign and magnitude of the ECIs of  $E_g$  and  $\Delta E$ . This discovery can be extended to general cases: if the dominant ECIs of two properties have the same sign, the properties are proportional. Conversely, if the dominant ECIs of two properties have different signs, the properties have an inverse relationship. The correlations of  $E_{g,\sigma}$  and  $\Delta E_\sigma$  with the short-range order parameters (SRO) quantitatively demonstrate the relationship between properties, which is inferred from the sign of ECIs. The correlations show, however, that the magnitude of ECIs is not directly related to the variations of a property because the possible range of the SRO for each cluster is different. The average bandgap at a certain composition and temperature ( $\overline{E_g}$ ) of Ga(As,Sb) is also calculated using grand canonical ensemble, taking into consideration compositional and configurational fluctuation. The calculated  $\overline{E_g}$  agrees with the experimental bandgap, reproducing the bandgap bowing. Due to the inverse relationship between  $E_g$  and  $\Delta E$ ,  $\overline{E_g}$  decreases as growth or annealing temperature increases. In addition, the tunable bandgap range of Ga(As,Sb) could be extended by controlling the configuration.

# CHAPTER 6

## (Be,Mg)O SOLID SOLUTION

---

### 6.1. Introduction

As fabrication of integrated circuits approaches the scaling limit, leakage current through the thin high- $\kappa$  dielectric layer has arisen as the main obstacle to further improvement. The tunneling leakage current is determined by the physical and electrical properties of dielectric films and exponentially decreases with increases in the dielectric constant ( $\kappa$ ), bandgap ( $E_g$ ), and film thickness [122]. Since the increase in thickness is limited by the device shrinkage, there have been extensive attempts to discover new dielectric materials with both high  $\kappa$  and high  $E_g$ . However, achieving the high polarization of an ionic crystal for a given electric field requires relatively weak bonding between the cations and anions, which must be accompanied by a

lower  $E_g$  value. Due to this undesirable inverse relation between  $\kappa$  and  $E_g$ , the development of a high  $\kappa$  material has remained as a challenging task. The wurtzite (WZ) structure BeO is a feasible candidate for next-generation dielectric material owing to its high  $E_g$  (10.6 eV) and the second-highest thermal conductivity (330 W/K·m) among oxide insulators, which mitigates the potential self-heating problem [123–125]. However, its  $\kappa$  value of 6.76 is not an exception from the above-mentioned general tradeoff between the  $\kappa$  and  $E_g$ , and thus its high- $\kappa$  applications seem to have limitations.

Recently, however, *ab initio*-based high-throughput screening predicted that rock salt (RS) BeO would have an extremely high  $\kappa$  (275) as well as an  $E_g$  of 10.1 eV [122]. Also, the dynamical stability of RS BeO was identified through phonon calculations. This finding is an important exception from the general  $\kappa$  -  $E_g$  relationship, which triggered the following theoretical and experimental studies. However, it should be noted that this previous work on the simultaneous high  $\kappa$  and  $E_g$  values regarded the crystal structure of BeO as that of the high-pressure phase of RS, assuming that the RS structure retains at the atmospheric pressure. In contrast, other theoretical studies reported conflicting findings that RS BeO is dynamically unstable under atmospheric conditions [126–128]. Experimentally, the stable structure of BeO under ambient conditions is identified as WZ, and the transition to RS occurs only at extremely high pressure (over 126 GPa) [129,130]. A theoretical study predicted that this transition pressure could be reduced by high temperature [131]. Despite the suggestions that RS BeO could be a highly desirable material as high- $\kappa$  dielectrics, experimental achievement of RS BeO film has not yet

been reported under ambient conditions even as a metastable phase.

As an alternative to RS BeO in the pursuit of high- $\kappa$  materials, a  $\text{Be}_x\text{Mg}_{1-x}\text{O}$  solid solution was proposed. The well-known RS lattice of MgO enables to provide an oxygen octahedral framework for Be atoms, stabilizing the octahedral bonds in RS with a longer Be-O bond length than the tetrahedral bonds in WZ BeO [132]. A previous experiment using atomic layer deposition (ALD) reported that the RS structure forms when the content of Be ( $x$ ) in  $\text{Be}_x\text{Mg}_{1-x}\text{O}$  is lower than 0.21, while the WZ structure is achieved when  $x$  is higher than 0.3 [132]. For the RS phase, the measured  $\kappa$  and  $E_g$  were approximately 18 and 8 eV, respectively. The same authors also calculated the energetic stability of  $\text{Be}_x\text{Mg}_{1-x}\text{O}$  and confirmed that RS is more stable than WZ at  $x < 0.2$ . Other theoretical studies estimated the transition composition of the  $\text{Be}_x\text{Mg}_{1-x}\text{O}$  phase: One study predicted the transition composition as  $x = 0.11$  by calculating only the representative configurations in RS and WZ [133], and the other used the SQS method to predict that a phase transition from RS to WZ occurs at  $x = 0.17$  [134]. On the other hand, it was noted that the phase of  $\text{Be}_x\text{Mg}_{1-x}\text{O}$  could not be simply distinguished as either RS or WZ. Be atoms slightly deviate from the octahedral sites even in RS (Be,Mg)O [134], which is plausible considering the much smaller size of Be ion compared to Mg ion. In this chapter, therefore, this deviated phase, referred to as modified RS (m-RS), is further examined theoretically. Unlike the predictions of the phase stability of  $\text{Be}_x\text{Mg}_{1-x}\text{O}$ , very few calculations of the dielectric constant have been done to date, despite its crucial role for device applications. Therefore, this chapter also focuses on the evolution of the  $\kappa$  value according to the specific

arrangement of the Be and Mg ions in the m-RS structure.

In this theoretical study based on *ab initio* calculations, the phase stability, as well as the key properties required for high- $\kappa$  dielectric ( $\kappa$  and  $E_g$ ) of  $\text{Be}_x\text{Mg}_{1-x}\text{O}$ , are thoroughly examined for WZ, RS, and m-RS phases. In order to reflect various atomic arrangements in solid solution depending on the experimental conditions, temperature dependencies of the properties are investigated for various configurations. As a result of this extensive search for a phase with the highest possible  $\kappa$  value, while maintaining the high  $E_g$  value, several candidates with the superlattice-like arrangement of the BeO and MgO layers are suggested as feasible atomic configurations. These configurations are stable up to the process and operating temperatures of the relevant devices. The proposed superlattice-like configurations, therefore, are prominent candidates as next-generation high- $\kappa$  dielectric materials for semiconductor devices.

## 6.2. Computation details

*Ab initio* calculations were performed using the Vienna Ab-initio Simulation Package (VASP) [80,81]. Blöchl's projector augmented wave (PAW) approach [82,83] was used to describe the electron-core interaction. The local density approximation (LDA) was used for the exchange-correlation potential [19,85] because LDA was reported to be better than the generalized gradient approximation (GGA) for the prediction of the dielectric constant [122]. The lattice constant calculated by LDA is 1.2% smaller for RS MgO and 1.0%

smaller for WZ BeO compared to their experimental counterparts. The energy cutoff for the plane-wave basis function was 600 eV. The k-points were sampled as  $8 \times 8 \times 8$  for the RS and m-RS unit cell and  $12 \times 12 \times 8$  for the WZ unit cell. All atomic structures were fully relaxed until all forces were below 0.02 eV/Å. The initial configurations for the m-RS structure were prepared by perturbing the position of Be atoms from the ideal RS lattice sites by less than 0.15 Å.

For the calculations of energy and  $E_g$ , all configurations were randomly generated by DBmaker in the LACOS package [84] in 64-atom supercells. The mixing energy  $\Delta E$  is defined as:

$$\Delta E = E(\text{Be}_x\text{Mg}_{1-x}\text{O}) - xE_{\text{WZ}}(\text{BeO}) - (1 - x)E_{\text{RS}}(\text{MgO}) \quad (6.1)$$

, where  $x$  denotes the BeO fraction, and  $E(\text{Be}_x\text{Mg}_{1-x}\text{O})$  is the energy of  $\text{Be}_x\text{Mg}_{1-x}\text{O}$ .  $E_{\text{WZ}}(\text{BeO})$  and  $E_{\text{RS}}(\text{MgO})$  indicate the energies of WZ BeO and RS MgO, respectively.  $\Delta E$  values were obtained for the RS, WZ, and m-RS structures and represented with respect to the most stable structure of the binary oxides, WZ BeO and RS MgO.

The static permittivity tensor  $\varepsilon_{\alpha\beta}^0$  was calculated as Eq. (2.17) and Eq. (2.20) using DFPT implemented in VASP. In most relevant applications, the voltage is applied along the out-of-plane direction of thin films; hence, the only  $\kappa_{zz}$  was focused in this chapter. The Born effective charge and harmonic phonon were calculated at 0 K using density functional perturbation theory (DFPT) [29,34]. The convergence tests for phonon dispersion were carried out up to 256-atom supercells, and 64-atom supercells were shown to be sufficient.

For phonon calculations, structures were more strictly relaxed until all forces were below 0.001 eV/Å.

To predict the temperature-dependent dielectric constant, the `phq` package [37] was employed, in which the anharmonic phonon contribution was extracted from the *ab initio* molecular dynamics (AIMD) calculations. The AIMD simulations were carried out for the configurations in the 64-atom supercells using only the  $\Gamma$  point. While controlling the temperature with a Nosé-Hoover thermostat, the AIMD was performed three times at each temperature (100, 200, 300, 400, 500, and 600 K) for 100 ps with a time step of 2 fs. The temperature-dependent thermal expansion was considered by tuning the lattice constants to minimize the absolute pressure during the AIMD simulations at each temperature. Another approach, called the fluctuation method, was used to predict the temperature-dependent dielectric constant.

### 6.3. Structure stability

RS BeO is the high-pressure phase. However, the high-throughput calculation, where the high dielectric constant of RS BeO was predicted, neglected lattice contraction by pressure [122]. Figure 6.1 shows the calculated  $\kappa_{zz}$  values of RS BeO are calculated as a function of pressure. The calculated  $\kappa_{zz}$  drastically decreases as the pressure increases: from 188 at 0 GPa to 16.1 at 100 GPa (91% decrease). At the same time, the Be-O bond length, corresponding to half of the lattice parameter, decreases almost linearly from

1.794 Å at 0 GPa to 1.657 Å at 100 GPa (7.6% decrease). As the high dielectric constant of RS BeO is supposed to come from the phonon softening due to the long Be-O bond length [122], the decrease in  $\kappa_{zz}$  with increasing pressure is attributed to phonon hardening (calculated as 4.19 THz at 0 GPa and 17.6 THz at 100 GPa) caused by the shortening of the Be-O bond length. Notably, the slight decrease in the Be-O bond length by 0.021 Å (1.2%) at 10 GPa leads to a drastic decrease in  $\kappa_{zz}$  (64%), implying that even a slight shortening of the Be-O bond length results in a substantial decrease in  $\kappa_{zz}$ . Given that RS BeO is stable at extremely high pressure (over 126 GPa) [129,130] and the dielectric constant of RS BeO is drastically reduced under high pressure, RS BeO is excluded from further investigation.

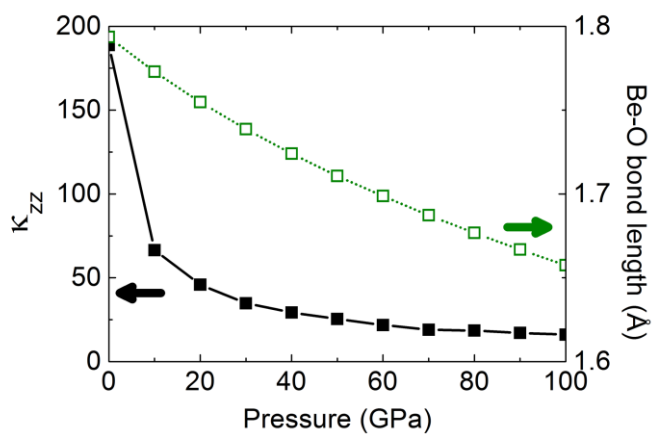


**Figure 6.1**  $\kappa_{zz}$  (black filled square with solid line) and Be–O bond length (green open square with dotted line) of RS BeO with respect to the pressure.

As an alternative to RS BeO, the solid solution,  $\text{Be}_x\text{Mg}_{1-x}\text{O}$ , is investigated. The  $x$  value is set as 0.25 considering the transition composition reported in previous studies [132–134], and the 8-atom cell, which is the smallest conventional cell in this composition, is examined. Figure 6.2 depicts several structures of BeO and corresponding phonon dispersion. The negative value in the phonon dispersion graph indicates the imaginary frequency, not the negative real value. Imaginary phonon frequency implies that energy becomes lower as the atom moves along the corresponding phonon mode and thus, a structure is dynamically unstable. All phonon frequencies of WZ  $\text{Be}_{0.25}\text{Mg}_{0.75}\text{O}$  are real, as shown in the right panel of Fig. 6.2 (a), which implies the dynamical stability of WZ  $\text{Be}_{0.25}\text{Mg}_{0.75}\text{O}$ . In contrast, the phonon dispersion of RS  $\text{Be}_{0.25}\text{Mg}_{0.75}\text{O}$  in Fig. 6.2 (b) has imaginary frequencies, indicating that the RS structure is dynamically unstable. This instability can be explained by Pauling’s first rule [135]: The ratio of the ionic radius of Be to that of O is 0.32, which means that the Be atom prefers to reside within the tetrahedral configuration (tetrahedral site in WZ lattice) rather than the octahedral configuration (octahedral site in RS lattice). In contrast, Mg atoms, for which the ratio of the ionic radius over O is 0.51, prefer to reside within the octahedral configuration of oxygen ions (octahedral site in RS). Accordingly, the octahedral configuration is formed as a base lattice by Mg atoms in RS  $\text{Be}_{0.25}\text{Mg}_{0.75}\text{O}$ , which provides too large space for Be atoms to reside. As a result, the Be-O bond length increases from 1.794 Å in RS BeO to 2.025 Å in RS  $\text{Be}_{0.25}\text{Mg}_{0.75}\text{O}$ . This large space for Be atoms triggers the Be atom to move from the center of

the octahedral site toward the oxygen ions. The resulting atomic configuration resembles the tetrahedral coordination of the Be ion with four neighboring oxygen ions. The structure containing this modified configuration is termed as the m-RS structure. Therefore, relaxation after a very slight perturbation of the Be atom induces the transition from the RS to the m-RS structure, resulting in increased dynamical stability, as shown in Fig. 6.2 (c). With the transition from RS to m-RS of  $\text{Be}_{0.25}\text{Mg}_{0.75}\text{O}$ , the bond length of Be-O decreases from 2.025 Å to 1.573 Å. This Be-O bond length in m-RS  $\text{Be}_{0.25}\text{Mg}_{0.75}\text{O}$  is even shorter than the 1.636 Å in WZ BeO, and the number of bonds for each Be atom is reduced to 3. As a result, the phonon softening effect due to the long Be-O bond length in RS can no longer be expected in m-RS, and, indeed, the  $\kappa_{zz}$  of m-RS  $\text{Be}_{0.25}\text{Mg}_{0.75}\text{O}$  is calculated to be 8.6. Since the m-RS structure is energetically and dynamically more stable than the RS structure at all compositions in the 8-atom cell and the energy difference between RS and m-RS increases as the BeO fraction increases as shown in Fig. 6.3., the RS  $\text{Be}_x\text{Mg}_{1-x}\text{O}$  structure is ruled out from further discussions.

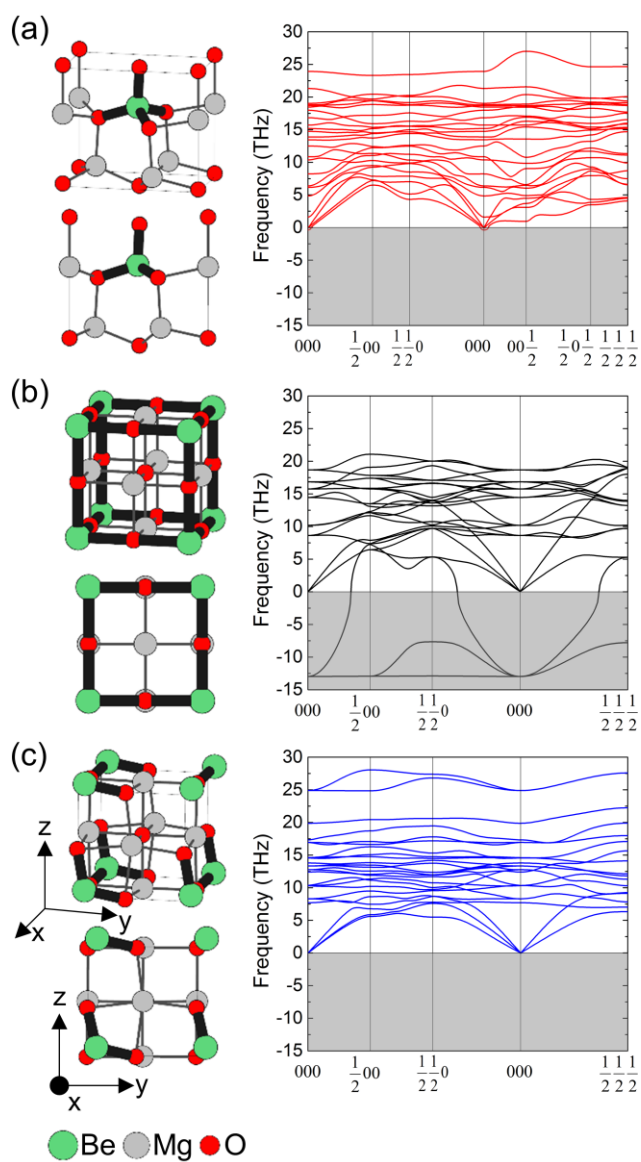


**Figure 6.2** Atomic structures and phonon dispersion of the 8-atom cell of (a) WZ, (b) RS and (c) m-RS structures of  $\text{Be}_{0.25}\text{Mg}_{0.75}\text{O}$ . Be–O bond is indicated by the thick black line.

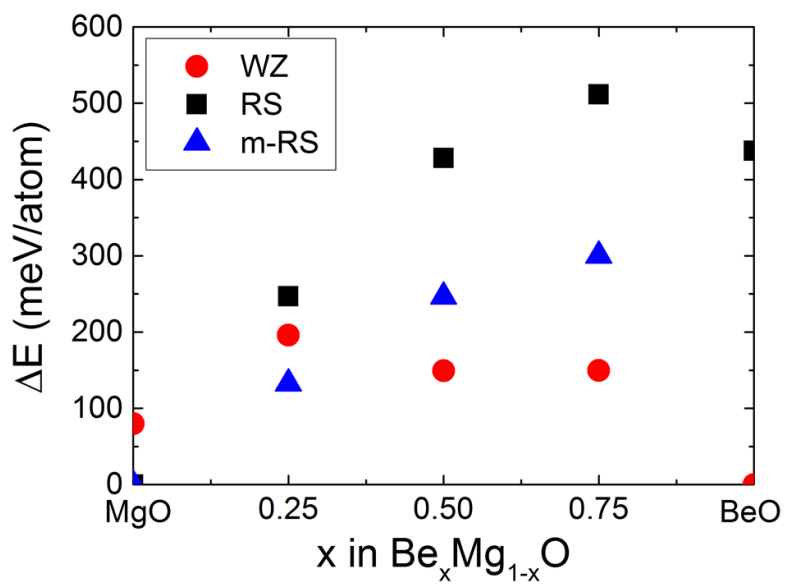


**Figure 6.3** Calculated  $\Delta E$  of WZ, RS, m-RS  $\text{Be}_x\text{Mg}_{1-x}\text{O}$  in 8-atom cell.

## 6.4. Energetics and bandgap

On the basis of diverse previous studies on composition-induced phase transition [132–134], the energetic stability and properties of various configurations in WZ and m-RS  $\text{Be}_x\text{Mg}_{1-x}\text{O}$  are examined. A total of 645 and 148 configurations are investigated for m-RS and WZ, respectively, using a 64-atom supercell with an interval of  $x$  of  $1/32$  ( $= 0.03125$ ). Since the m-RS structure cannot be maintained when  $x$  is higher than 0.5, m-RS  $\text{Be}_x\text{Mg}_{1-x}\text{O}$  is investigated only for  $x < 0.5$ . Figure 6.4 shows the mixing energy ( $\Delta E$ ) defined as Eq. (6.1) and bandgap ( $E_g$ ) of m-RS and WZ  $\text{Be}_x\text{Mg}_{1-x}\text{O}$  in the 64-atom cell as a function of the  $x$ -value. The blue and red symbols indicate the properties of individual configurations in the m-RS and WZ structure, respectively. As shown in Fig. 6.4 (a), the configuration-dependent variation in  $\Delta E$  for a given composition is not negligible. For instance, the configuration-dependent fluctuation of  $\Delta E$  at  $x = 0.25$  is  $\sim 50$  meV/atom, which is higher than the thermal energy under ambient conditions (25 meV/atom). Owing to this configuration-dependent  $\Delta E$ , the energetic stabilities of m-RS and WZ compete in the composition range  $0.25 \leq x \leq 0.3125$ , as more clearly shown in the inset of Fig. 6.4 (a). When  $x$  is higher than  $\sim 0.3$ , WZ becomes energetically more stable than m-RS. This is one explanation for the differences in transition composition reported in previous experimental and calculation studies [132–134].

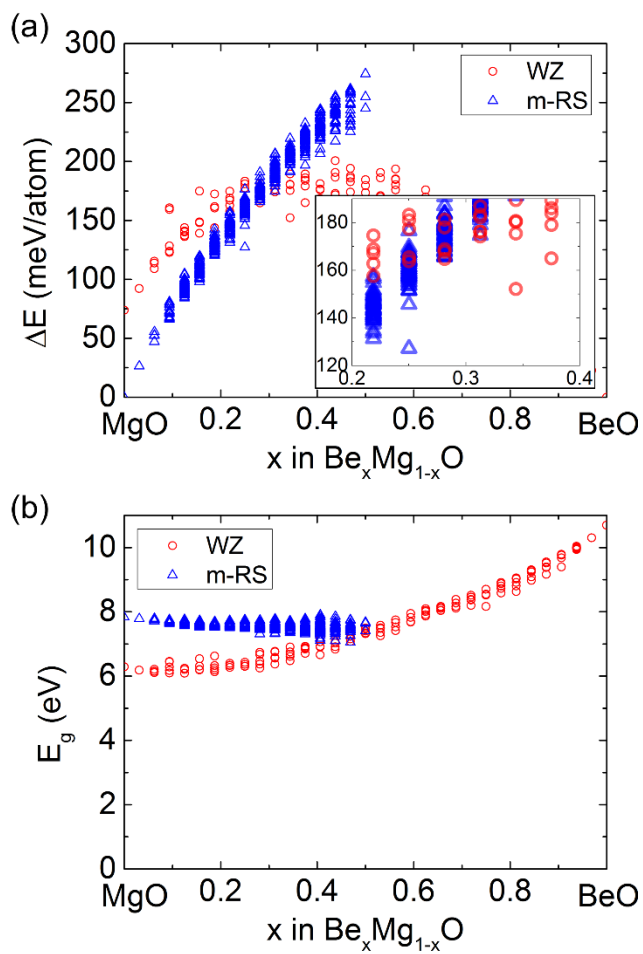


**Figure 6.4** Calculated (a)  $\Delta E$  and (b)  $E_g$  of WZ and m-RS  $\text{Be}_x\text{Mg}_{1-x}\text{O}$  in 64-atom cells.

The calculated bandgaps of the stable structures of WZ-BeO and RS-MgO are 7.9 eV and 5.0 eV, respectively. These values are  $\sim 2.8$  eV lower than the experimental bandgap of WZ-BeO, 10.6 eV [136], and RS-MgO, 7.8 eV [137], because of the well-known bandgap underestimation problem of the LDA method used in this chapter. Thus, the calculated bandgaps of  $\text{Be}_x\text{Mg}_{1-x}\text{O}$  are corrected by adding 2.8 eV, which is also the case in a previous report [133]; the results are plotted in Fig. 6.4 (b). In the composition  $x \leq \sim 0.3$ , where m-RS is more stable than WZ, the bandgap of all m-RS configurations ranges between 7.3 and 7.9 eV. The bandgaps of m-RS are always higher than those of WZ in the range  $x \leq \sim 0.3$  irrespective of the configurations. Regardless of composition and configuration, m-RS BeO has the  $E_g$  higher than the  $E_g$  of the common insulating materials, such as 7.1 eV of amorphous  $\text{Al}_2\text{O}_3$ . Because the bandgap of m-RS  $\text{Be}_x\text{Mg}_{1-x}\text{O}$  does not significantly depend on composition and configuration and is enough high to be an insulator, the following calculations are focused on the possibility of increasing  $\kappa_{zz}$  by the configuration control in m-RS  $\text{Be}_x\text{Mg}_{1-x}\text{O}$ .

## 6.5. Temperature-dependent dielectric constant

The  $\kappa_{zz}$  of the m-RS  $\text{Be}_{0.25}\text{Mg}_{0.75}\text{O}$  calculated in an 8-atom cell, as shown in Fig. 6.2 (c), is 8.6, which is as low as that of MgO. Moreover, this value is much lower than the experimentally observed dielectric constant of 18

in this composition range [132]. Therefore, the variation of a dielectric constant by configuration was further examined by using larger supercells. Because of the high computational cost for calculations of the dielectric constant,  $x$  is set to 0.25, where the m-RS phase is still more stable than the WZ phase, and the structure is expected to have a high dielectric constant. First, a relatively small supercell ( $1 \times 1 \times 2$ ) composed of 16 atoms is adopted to calculate the dielectric constant as well as the static and dynamic stability, as shown in Fig. 6.5. Total 14 configurations are allowed to be expressed within  $1 \times 1 \times 2$  supercell of m-RS  $\text{Be}_{0.25}\text{Mg}_{0.75}\text{O}$ , which are depicted in Fig. 6.5 (a). The last three configurations marked with the gray background in Fig. 6.5 (a) have imaginary phonon frequencies. Therefore, they are excluded from further consideration owing to their dynamic instability. In Fig. 6.5 (b),  $\kappa_{zz}$  is plotted as a function of Be-O bond length along the z-axis, which is referred to as apical bond length. The configurations are divided into two groups by  $\kappa_{zz}$  value (higher or lower than 14), which is mainly determined by the apical bond length: When the apical bond length is longer than 1.85 Å,  $\kappa_{zz}$  is higher than 14. Among the estimated configurations, configuration #1 shows a  $\kappa_{zz}$  value as high as 64. It is interesting to note that this configuration does not involve imaginary phonon modes, so it is dynamically stable. However, this does not necessarily mean that this configuration is readily achievable. Figure 6.5 (c) shows the relationship between  $\kappa_{zz}$  and  $dE$ , the relative energy with respect to the lowest energy configuration (configuration #11) among the 14 configurations. As shown in Fig. 6.4, the configurational dependency of energy is not negligible. Unfortunately, the configurations with low energy tend to have low  $\kappa_{zz}$  values,

whereas the configurations with high  $\kappa_{zz}$  have dE values higher than 20 meV/atom. This implies that it could be difficult to experimentally demonstrate a high- $\kappa_{zz}$  configuration. Nonetheless, the first three configurations (configurations #1, #2 and #3) in Fig. 6.5 (a) have superlattice-like arrangements of an alternate stacking of one BeO layer and three MgO layers and show relatively high  $\kappa_{zz}$  (64, 28 and 19, respectively) as plotted with distinguishable colors in Fig. 6.5 (b) and (c). These characteristic arrangements might provide an opportunity to grow films with such configurations using ALD, given the layer-by-layer growth mechanism, despite their slightly high dE values (29, 20, and 38 meV/atom, respectively). Therefore, we focus on the first three configurations in Fig. 6.5 (a).

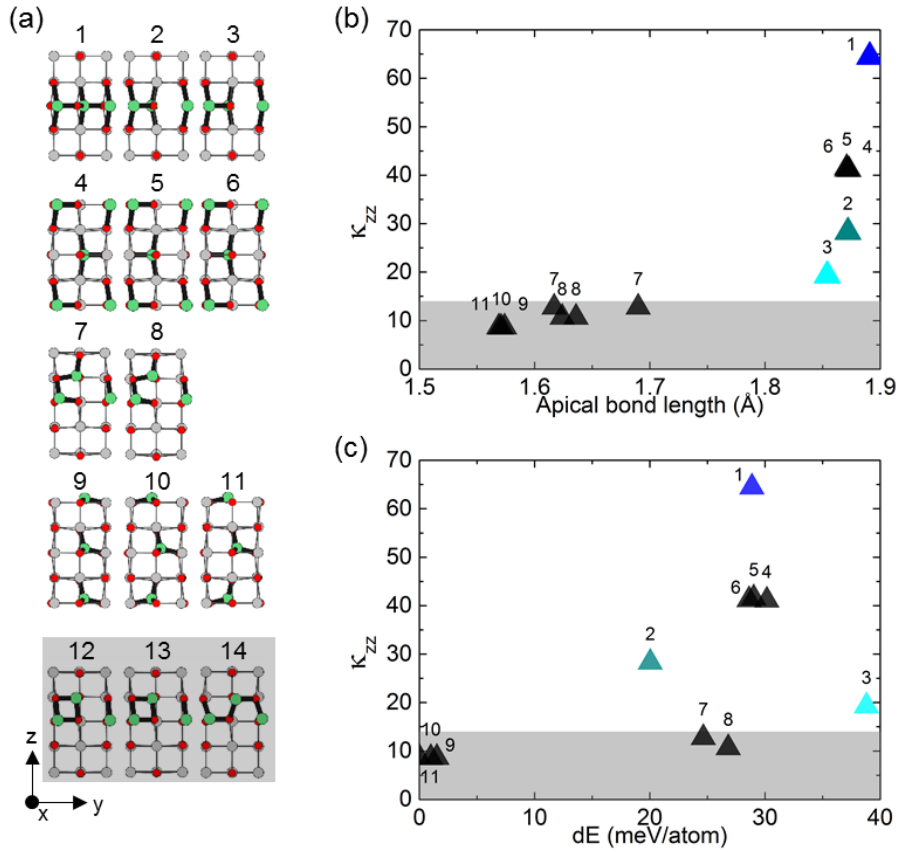


**Figure 6.5** (a) Side views of all possible configurations in  $1 \times 1 \times 2$  supercell composed of 16 atoms of m-RS  $\text{Be}_{0.25}\text{Mg}_{0.75}\text{O}$ . The last three configurations with a gray background have a negative frequency at  $\Gamma$ -point. (b)  $\kappa_{zz}$  vs. apical bond length (c)  $\kappa_{zz}$  vs.  $dE$ .  $dE$  is the relative energy of a certain configuration with respect to the lowest energy configuration (configuration #11). The symbols for configurations with superlattice-like structure are colored.

For more precise estimation, the three selected configurations obtained in  $1 \times 1 \times 2$  supercells are simply enlarged to  $2 \times 2 \times 2$  supercells without atomic relaxation, as shown in Fig. 6.6 (a-c). According to the shape of the Be-O bonds viewed from the z-direction (left panel of the atomic configuration figures), represented by thick lines, the configurations are named high- $\kappa$  zigzag-type (*HZ*) (Fig. 6.6 (a)), high- $\kappa$  armchair-type (*HA*) (Fig. 6.6 (b)), and rhombus-type (*R*) (Fig. 6.6 (c)), respectively. Unexpectedly, the phonon dispersions calculated in the  $2 \times 2 \times 2$  supercell of *HZ* and *HA* without atomic relaxation show imaginary frequencies, as shown by the phonon dispersions below the atomic configuration. These two configurations are further relaxed after a small perturbation along the atomic displacement induced by the phonon modes with the most negative eigenvalue at  $\Gamma$  point, which is 000 point in reciprocal space. Consequently, dynamically stable configurations are once again obtained, as shown in Fig. 6.6 (d) and (e). As clearly shown by the view along with the  $[1\bar{1}0]$  direction in Fig. 6.6 (d) and (e), half of the Be atoms move along the  $[001]$  direction while the other half moves along the  $[00\bar{1}]$  direction, breaking one of the previously apical Be-O bonds. This structural change results in a decrease in the coordination number of Be from 4 to 3 and a shortening of the remaining Be-O bonds. As a result, the phonon dispersions become stable, but  $\kappa_{zz}$  substantially decreases from 64 to 12 for the zigzag-type and from 28 to 13 for the armchair-type configuration. Accordingly, these configurations are named low- $\kappa$  zigzag-type (*LZ*) (Fig. 6.6 (d)) and low- $\kappa$  armchair-type (*LA*) (Fig.

6.6 (e)), respectively. Unlike the drastic decrease in  $\kappa_{zz}$ , the decrease in  $dE$  and  $E_g$  is not significant: 4.8 meV/atom and 0.3 eV for zigzag-type, and 1.5 meV/atom and  $\sim 0$  eV for armchair-type. On the other hand, even when  $R$  is relaxed in the  $2 \times 2 \times 2$  supercell, the atomic structure of  $R$  is maintained without imaginary frequency in its phonon dispersion, and  $\kappa_{zz}$  remains 19. The bond length and  $\kappa_{zz}$  of the five configurations shown in Fig. 6.6 (f) imply the explicit relation that the long apical Be-O bond is crucial for high  $\kappa_{zz}$ ; for  $HZ$ ,  $HA$ , and  $R$ , the  $\kappa_{zz}$  are 64, 28, 19 and the apical bond lengths are 1.891 Å, 1.872 Å, 1.854 Å, respectively. These bond lengths are longer than the corresponding value of 1.794 Å in RS BeO at 0 Pa (Fig. 6.1). On the contrary, the equatorial Be-O bond lengths and  $\kappa_{zz}$  do not show any clear relationship. Thus, the significant reduction in  $\kappa_{zz}$  to below 14 in  $LZ$  and  $LA$  is presumably attributed to the shortening of the apical Be-O bonds (*i.e.*, loss of phonon softening).

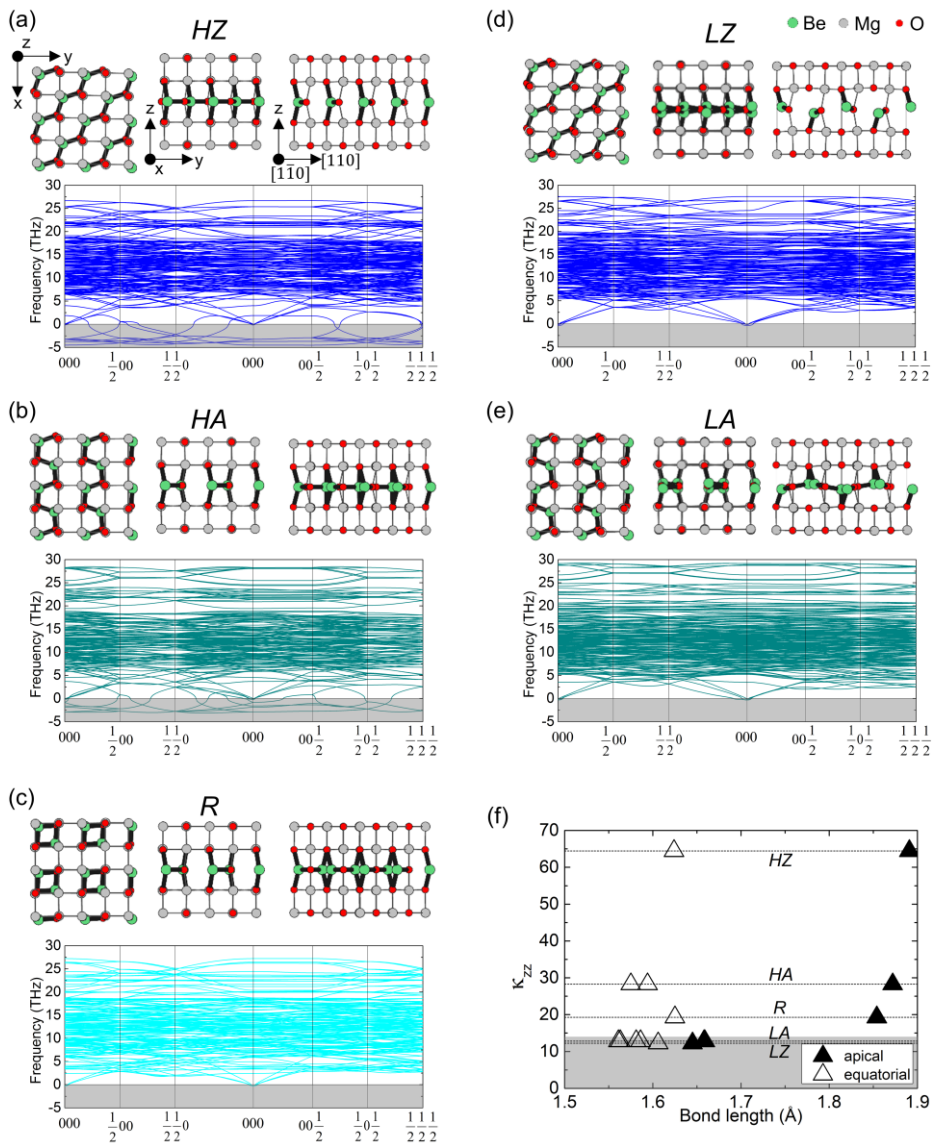


**Figure 6.6** Top view, side view, and phonon dispersion of  $\text{Be}_{0.25}\text{Mg}_{0.75}\text{O}$  in  $2 \times 2 \times 2$  supercell of (a) HZ, (b) HA, (c) R, (d) LZ, and (e) LA. (f) Be–O bond length and  $\kappa_{zz}$  for each configuration. Solid triangle indicates the apical bond length, while the open triangle indicates the equatorial bond length.

The  $\kappa_{zz}$  values of the *LZ* and *LA* configurations with stable phonons at 0 K in Fig. 6.6 (f) are slightly lower than the experimental value of 18 [132]. This discrepancy could have resulted from the different temperatures used for the *ab initio* calculation (0 K) and experiment (room temperature). Therefore, the temperature dependence of the dielectric constant is further examined by adding the anharmonic phonon effects calculated by the AIMD simulations on these three superlattice-like configurations. Figure 6.7 shows the atomic positions along the [100] direction, which are averaged over the AIMD trajectory at temperatures from 100 to 600 K in comparison with those at 0 K. According to the average atomic positions, the transition from low- $\kappa$  to high- $\kappa$  occurs in the temperature range of 200–300 K for the zigzag-type configuration in Fig. 6.7 (a), while that for the armchair-type in Fig. 6.7 (b) occurs in the range of 0 – 100 K. The dynamically unstable structure is bound to be changed into a stable structure due to the perturbation during the AIMD simulation. Thus, the transitions of zigzag-type and armchair-type from low- $\kappa$  to high- $\kappa$  imply that the high- $\kappa$  structures are dynamically stable over the transition temperature. Meanwhile, the rhombus shape in Fig. 6.7 (c) does not show any notable change up to 200 K. As the temperature increases further, *HZ* and *R* become identical to *HA* over 500 K and 200 K, respectively. All the structures are maintained within the considered superlattice-like types up to 600 K, indicating that the suggested superlattice-like structures will be useful in actual semiconductor device applications.

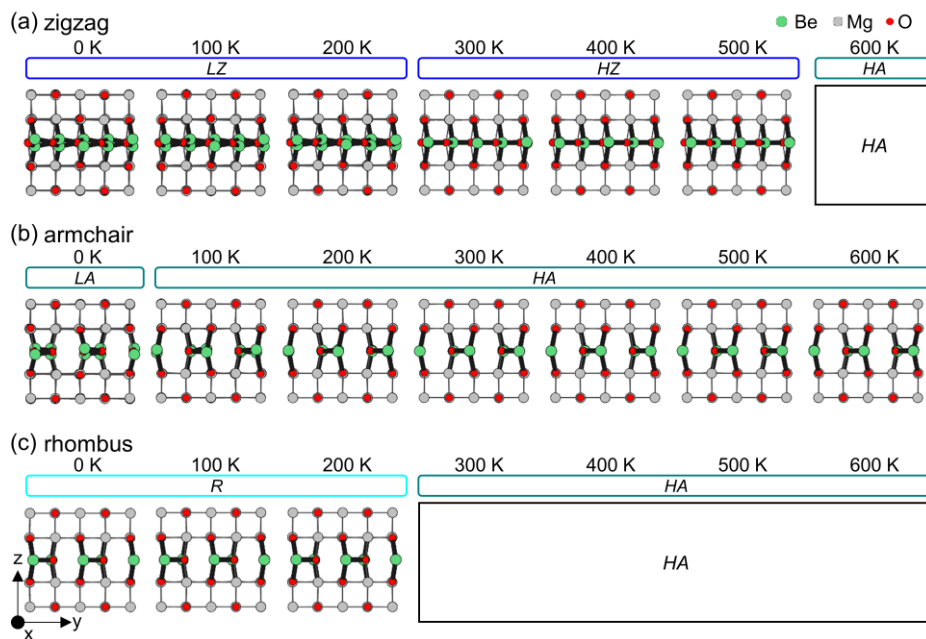


**Figure 6.7** Side views of the atomic configuration at 0 K and the average atomic position at 100, 200, 300, 400, 500, and 600 K calculated by AIMD calculations for (a) zigzag, (b) armchair, and (c) rhombus-type.

The temperature-dependent  $\kappa_{zz}$  values estimated from the structures shown in Fig. 6.7 are plotted in Fig. 6.8 (a). The  $\kappa_{zz}$  at 0 K is calculated by harmonic phonons for the configurations with stable phonons in Fig. 6.6 (c-e) (*R*, *LZ*, and *LA*), while  $\kappa_{zz}$  at non-0 K is obtained by anharmonic phonons. The  $\kappa_{zz}$  of the zigzag-type configuration abruptly changes between 200 and 300 K, while that of the armchair-type configuration changes between 0 and 100 K, which corroborate the structural transition from low- $\kappa$  to high- $\kappa$  configurations with increasing temperature as shown in Fig. 6.  $\kappa_{xx}$  and  $\kappa_{yy}$  vary within 9-12 across the entire range of calculated temperature, and are lower than  $\kappa_{zz}$ . Considering that the deposition temperature of BeO and  $\text{Be}_x\text{Mg}_{1-x}\text{O}$  by ALD is over 400 K [125,132,138] and that the transition from *R* to *HA* occurs at 200 – 300 K (Fig. 6.7), the rhombus shape is unlikely to be achieved in the experiment. Thus, the observable  $\kappa_{zz}$  may correspond to the average value between the zigzag- and armchair-type configurations because the two types have similar energetic stabilities. The average  $\kappa_{zz}$  value is 18 – 20 in the temperature range of 300 to 600 K, which is comparable to the experimental results [132]. This implies that the experimentally achieved dielectric constant of 18, which is higher than those of the end members (BeO and MgO), must be attributable to the specific bonding geometry of  $\text{Be}_x\text{Mg}_{1-x}\text{O}$  as suggested in this chapter. The  $\kappa_{zz}$  plotted in Fig. 6.8 (b) is calculated using fluctuation method using Eq. (2.22). The  $\kappa_{zz}$  in Fig. 6.8 (b) is higher than  $\kappa_{zz}$  shown in Fig. 6.8 (a), but the overall trend is in good agreement.

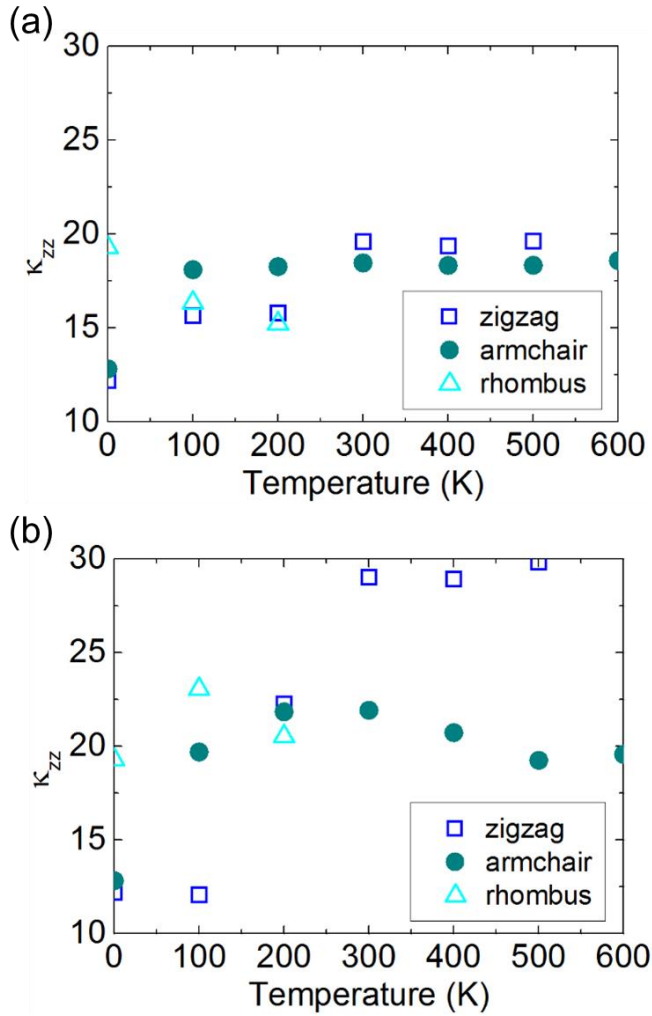


**Figure 6.8** Temperature dependency of  $\kappa_{zz}$  for  $\text{Be}_{0.25}\text{Mg}_{0.75}\text{O}$  superlattices calculated using (a) phonon frequency extracted with phq, and (b) fluctuation method.

## 6.6. Conclusion

The phase stability, bandgap, and dielectric constant of  $\text{Be}_x\text{Mg}_{1-x}\text{O}$ , a next-generation high- $\kappa$  dielectric material, are investigated by *ab initio* calculations. Be atoms located at the center of the large octahedral sites in RS  $\text{Be}_x\text{Mg}_{1-x}\text{O}$  are not stable and have a tendency to move toward the oxygen atoms, resulting in m-RS  $\text{Be}_x\text{Mg}_{1-x}\text{O}$ , in which the local structure surrounding the Be atoms resembles the tetrahedral site. The m-RS  $\text{Be}_x\text{Mg}_{1-x}\text{O}$  has a much lower  $\kappa$  value than the previously reported value (275) for RS BeO, which did not take into account the structural transition of the local atomic configuration. Due to the configuration-dependent energetic stability, the transition from the m-RS to the WZ phase is predicted to occur near  $x = 0.3$  as the  $x$ -value increases in  $\text{Be}_x\text{Mg}_{1-x}\text{O}$ . When the m-RS phase is stable, the bandgap is calculated to be in the range of 7.3 eV to 7.9 eV. The variation in the bandgap caused by compositional and configurational dependence is not significant. Among many atomic configurations with the composition  $\text{Be}_{0.25}\text{Mg}_{0.75}\text{O}$ , three configurations (zigzag-, armchair-, and rhombus-type) with superlattice-like structures composed of one BeO and three MgO layers are intensively examined, as they have the potential to show a higher  $\kappa$  value than those of pure BeO, MgO and the other configurations. At 0 K, all three structures showed  $\kappa_{zz}$  values of  $\sim 12$ , which is significantly lower than the experimentally achieved value of 18 of a film with a similar composition. As temperature increases, however, their configurations change to include longer apical Be-O bond lengths, which leads to an increase in  $\kappa_{zz}$  to over 18. These superlattice-like structures show high

thermal stability up to  $\sim 600$  K. Therefore, these structures could prove to be useful as high- $\kappa$  dielectric layers for next-generation semiconductor devices. Furthermore, this chapter suggests that the local atomic configuration of an experimental  $\text{Be}_{0.25}\text{Mg}_{0.75}\text{O}$  film with a  $\kappa$  value of approximately 18 must have a superlattice-like arrangement, which requires further experimental confirmation.

## 6.7. Appendix

In this dissertation, the temperature-dependent dielectric constant is calculated based on the fact that the dielectric constant can be calculated from the phonon dispersion using Eq. (2.17). However, it is hard to confirm that phenomenon such as degradation of dielectric constant induced by the thermal fluctuation of the dipole can be reproduced with this method. There are two other methods for calculating the temperature-dependent dielectric constant having the literature where the decrease of dielectric constant as temperature increases was reported [39,41]. One is the fluctuation method based on Eq. (2.22), and the other is the external field method based on Eq. (2.24). The external field method requires MD simulation under an electric field which is not supported by the VASP package while the MD simulation for the fluctuation field method does not require an electric field. Both methods are briefly introduced in section 2.5. The equation for the fluctuation method (Eq. (2.22)) can be derived from Eq. (2.23) as follows:

$$F_i = U_i - V\vec{P}_i\vec{E} \quad (2.23)$$

$$Z = \sum_i \exp\left(-\frac{F_i}{k_B T}\right) \quad (6.2)$$

$$\langle \vec{M} \rangle = V \langle \vec{P} \rangle = k_B T \frac{1}{Z} \frac{\partial Z}{\partial \vec{E}} \quad (6.3)$$

$$\kappa = \frac{\epsilon}{\epsilon_0} = \frac{1}{\epsilon_0} \frac{\partial \langle \vec{P} \rangle}{\partial \vec{E}} = \frac{1}{\epsilon_0 V} \frac{\partial \langle \vec{M} \rangle}{\partial \vec{E}} = \frac{k_B T}{\epsilon_0} \left[ \frac{1}{Z} \frac{\partial^2 Z}{\partial \vec{E}^2} - \frac{1}{Z^2} \left( \frac{\partial Z}{\partial \vec{E}} \right)^2 \right] = \frac{1}{\epsilon_0 V k_B T} \left[ \langle \vec{M}^2 \rangle - \langle \vec{M} \rangle^2 \right] \quad (6.4)$$

From the derivation, the reason why the variance of dipole moment is related to the dielectric constant can be understood. When the electric field is applied, the free energy of each microstate in Eq. (2.23) changes. As microstate has larger polarization, the change of free energy becomes larger. It results in a larger change of occurrence probability. Thus, a large variance of polarization along the electric field direction results in a high dielectric constant. However, it should be noted that the dielectric constant calculated from Eq. (6.4) deals with small changes in an electric field.

# BIBLIOGRAPHY

---

- [1] M. Hoffmann, S. Slesazeck, U. Schroeder, T. Mikolajick, What's next for negative capacitance electronics?, *Nat. Electron.* 3 (2020) 504–506. <https://doi.org/10.1038/s41928-020-00474-9>.
- [2] W. Jeon, Recent advances in the understanding of high-k dielectric materials deposited by atomic layer deposition for dynamic random-access memory capacitor applications, *J. Mater. Res.* 35 (2020) 775–794. <https://doi.org/DOI: 10.1557/jmr.2019.335>.
- [3] M. Ozeki, Atomic layer epitaxy of III–V compounds using metalorganic and hydride sources, *Mater. Sci. Reports.* 8 (1992) 97–146. [https://doi.org/10.1016/0920-2307\(92\)90008-O](https://doi.org/10.1016/0920-2307(92)90008-O).
- [4] M. Leskelä, M. Mattinen, M. Ritala, Review Article: Atomic layer deposition of optoelectronic materials, *J. Vac. Sci. Technol. B.* 37 (2019) 30801. <https://doi.org/10.1116/1.5083692>.
- [5] M. Lee, C.-U. Kim, Investigation on self-aligned HgTe nano-crystals induced by controlled precipitation in PbTe–HgTe quasi-binary compound semiconductor alloys, *Phys. B Condens. Matter.* 304 (2001) 267–275. [https://doi.org/https://doi.org/10.1016/S0921-4526\(01\)00535-X](https://doi.org/https://doi.org/10.1016/S0921-4526(01)00535-X).
- [6] J.K. Shurtleff, R.T. Lee, C.M. Fetzer, G.B. Stringfellow, Band-gap control of GaInP using Sb as a surfactant, *Appl. Phys. Lett.* 75 (1999)

1914–1916.

- [7] W.Y. Jiang, J.Q. Liu, M.G. So, T.S. Rao, M. Thewalt, K.L. Kavanagh, S.P. Watkins, Effect of Bi surfactant on atomic ordering of GaAsSb, *Appl. Phys. Lett.* 85 (2004) 5589–5591.  
<https://doi.org/10.1063/1.1830687>.
- [8] H. Lv, X. Liang, G. Ji, H. Zhang, Y. Du, Porous Three-Dimensional Flower-like Co/CoO and Its Excellent Electromagnetic Absorption Properties, *ACS Appl. Mater. Interfaces.* 7 (2015) 9776–9783.  
<https://doi.org/10.1021/acsami.5b01654>.
- [9] L. Nordheim, Zur elektronentheorie der metalle. I, *Ann. Phys.* 401 (1931) 607–640. <https://doi.org/10.1002/andp.19314010507>.
- [10] P. Soven, Coherent-Potential Model of Substitutional Disordered Alloys, *Phys. Rev.* 156 (1967) 809–813.  
<https://doi.org/10.1103/PhysRev.156.809>.
- [11] J. Shenoy, J.N. Hart, R. Grau-Crespo, N.L. Allan, C. Cazorla, Mixing thermodynamics and photocatalytic properties of GaP–ZnS solid solutions, *Adv. Theory Simulations.* 2 (2019) 1800146.  
<https://doi.org/10.1002/adts.201800146>.
- [12] G. Han, I.W. Yeu, J. Park, K.H. Ye, S.-C. Lee, C.S. Hwang, J.-H. Choi, Effect of local strain energy to predict accurate phase diagram of III–V pseudobinary systems: case of Ga (As, Sb) and (In, Ga) As, *J. Phys. D: Appl. Phys.* 54 (2021) 045104. <https://doi.org/10.1088/1361->

6463/abbf78.

- [13] G. Han, I.W. Yeu, K.H. Ye, C.S. Hwang, J.-H. Choi, Atomistic prediction on the composition- and configuration-dependent bandgap of Ga(As,Sb) using cluster expansion and ab initio thermodynamics, Mater. Sci. Eng. B. (n.d.) submitted.
- [14] G. Han, I.W. Yeu, K.H. Ye, S.-C. Lee, C.S. Hwang, J.-H. Choi, Atomistic prediction on the configuration-and temperature-dependent dielectric constant of  $\text{Be}_{0.25}\text{Mg}_{0.75}\text{O}$  superlattice as a high- $\kappa$  dielectric layer, J. Mater. Chem. C. 9 (2021) 851–859.  
<https://doi.org/10.1039/D0TC05071G>.
- [15] A. Sher, M. van Schilfgaarde, A.-B. Chen, W. Chen, Quasichemical approximation in binary alloys, Phys. Rev. B. 36 (1987) 4279–4295.  
<https://doi.org/10.1103/PhysRevB.36.4279>.
- [16] F. Giustino, Materials modelling using density functional theory: properties and predictions, Oxford University Press, 2014.
- [17] D.C. Mattis, Many-body Problem, The: An Encyclopedia Of Exactly Solved Models In One Dimension (3rd Printing With Revisions And Corrections), World Scientific, 1993.
- [18] W. Kohn, L.J. Sham, Self-consistent equations including exchange and correlation effects, Phys. Rev. 140 (1965) A1133.  
<https://doi.org/10.1103/PhysRev.140.A1133>.
- [19] D.M. Ceperley, B.J. Alder, Ground state of the electron gas by a

- stochastic method, *Phys. Rev. Lett.* 45 (1980) 566–569.  
<https://doi.org/10.1103/PhysRevLett.45.566>.
- [20] J.P. Perdew, K. Burke, M. Ernzerhof, Generalized gradient approximation made simple, *Phys. Rev. Lett.* 77 (1996) 3865.  
<https://doi.org/10.1103/PhysRevLett.77.3865>.
- [21] J.M. Sanchez, F. Ducastelle, D. Gratias, Generalized cluster description of multicomponent systems, *Phys. A Stat. Mech. Its Appl.* 128 (1984) 334–350. [https://doi.org/10.1016/0378-4371\(84\)90096-7](https://doi.org/10.1016/0378-4371(84)90096-7).
- [22] D. De Fontaine, Cluster Approach to Order-Disorder Transformations in Alloys, in: H. Ehrenreich, D. Turnbull (Eds.), *Solid State Phys.*, Elsevier, 1994: pp. 33–176. [https://doi.org/10.1016/s0081-1947\(08\)60639-6](https://doi.org/10.1016/s0081-1947(08)60639-6).
- [23] C.A. Wang, H.K. Choi, S.L. Ransom, G.W. Charache, L.R. Danielson, D.M. DePoy, High-quantum-efficiency 0.5 eV GaInAsSb/GaSb thermophotovoltaic devices, *Appl. Phys. Lett.* 75 (1999) 1305–1307.  
<https://doi.org/10.1063/1.124676>.
- [24] O. Jani, H. Yu, E. Trybus, B. Jampana, I. Ferguson, A. Doolittle, C. Honsberg, Effect of phase separation on performance of III-V nitride solar cells, in: *22nd Eur. Photovolt. Sol. Energy Conf.*, 2007: pp. 64–67.
- [25] N.J. Quitoriano, E.A. Fitzgerald, Relaxed, high-quality InP on GaAs by using InGaAs and InGaP graded buffers to avoid phase separation,

- J. Appl. Phys. 102 (2007) 33511. <https://doi.org/10.1063/1.2764204>.
- [26] B.N. Pantha, J. Li, J.Y. Lin, H.X. Jiang, Evolution of phase separation in In-rich InGaN alloys, Appl. Phys. Lett. 96 (2010) 232105. <https://doi.org/10.1063/1.3453563>.
- [27] L. Yang, M.T. Bulsara, K.E. Lee, E.A. Fitzgerald, Compositionally-graded InGaAs–InGaP alloys and GaAsSb alloys for metamorphic InP on GaAs, J. Cryst. Growth. 324 (2011) 103–109. <https://doi.org/10.1016/j.jcrysgro.2011.04.032>.
- [28] B. Zhang, W. Qiu, S. Chen, P. Chen, W.M. Chen, I.A. Buyanova, X. Wang, Effect of exciton transfer on recombination dynamics in vertically nonuniform GaAsSb epilayers, Appl. Phys. Lett. 114 (2019) 252101. <https://doi.org/10.1063/1.5105343>.
- [29] X. Gonze, C. Lee, Dynamical matrices, Born effective charges, dielectric permittivity tensors, and interatomic force constants from density-functional perturbation theory, Phys. Rev. B. 55 (1997) 10355–10368. <https://doi.org/10.1103/PhysRevB.55.10355>.
- [30] R.M. Sternheimer, Electronic polarizabilities of ions from the Hartree-Fock wave functions, Phys. Rev. 96 (1954) 951.
- [31] S. Baroni, P. Giannozzi, A. Testa, Green’s-function approach to linear response in solids, Phys. Rev. Lett. 58 (1987) 1861–1864. <https://doi.org/10.1103/PhysRevLett.58.1861>.
- [32] X. Gonze, Perturbation expansion of variational principles at arbitrary

- order, *Phys. Rev. A.* 52 (1995) 1086–1095.  
<https://doi.org/10.1103/PhysRevA.52.1086>.
- [33] X. Gonze, Adiabatic density-functional perturbation theory, *Phys. Rev. A.* 52 (1995) 1096–1114. <https://doi.org/10.1103/PhysRevA.52.1096>.
- [34] S. Baroni, S. de Gironcoli, A. Dal Corso, P. Giannozzi, Phonons and related crystal properties from density-functional perturbation theory, *Rev. Mod. Phys.* 73 (2001) 515–562.  
<https://doi.org/10.1103/RevModPhys.73.515>.
- [35] T. Tadano, Y. Gohda, S. Tsuneyuki, Anharmonic force constants extracted from first-principles molecular dynamics: applications to heat transfer simulations, *J. Phys. Condens. Matter.* 26 (2014) 225402.  
<https://doi.org/10.1088/0953-8984/26/22/225402>.
- [36] T. Tadano, S. Tsuneyuki, Self-consistent phonon calculations of lattice dynamical properties in cubic SrTiO<sub>3</sub> with first-principles anharmonic force constants, *Phys. Rev. B.* 92 (2015).  
<https://doi.org/10.1103/PhysRevB.92.054301>.
- [37] Z. Zhang, D.-B. Zhang, T. Sun, R.M. Wentzcovitch, phq: A Fortran code to compute phonon quasiparticle properties and dispersions, *Comput. Phys. Commun.* 243 (2019) 110–120.  
<https://doi.org/10.1016/j.cpc.2019.05.003>.
- [38] M. Neumann, Dipole moment fluctuation formulas in computer simulations of polar systems, *Mol. Phys.* 50 (1983) 841–858.

<https://doi.org/10.1080/00268978300102721>.

- [39] A. Kumar, K.M. Rabe, U. V Waghmare, Domain formation and dielectric response in  $\text{PbTiO}_3$ : A first-principles free-energy landscape analysis, *Phys. Rev. B.* 87 (2013) 024107.  
<https://doi.org/10.1103/PhysRevB.87.024107>.
- [40] C. Zhang, M. Sprik, Computing the dielectric constant of liquid water at constant dielectric displacement, *Phys. Rev. B.* 93 (2016) 144201.  
<https://doi.org/10.1103/PhysRevB.93.144201>.
- [41] A. Mattoni, C. Caddeo, Dielectric function of hybrid perovskites at finite temperature investigated by classical molecular dynamics, *J. Chem. Phys.* 152 (2020) 104705. <https://doi.org/10.1063/1.5133064>.
- [42] S.H. Wei, L.G. Ferreira, A. Zunger, First-principles calculation of temperature-composition phase diagrams of semiconductor alloys, *Phys. Rev. B.* 41 (1990) 8240–8269.  
<https://doi.org/10.1103/PhysRevB.41.8240>.
- [43] F.D. Murnaghan, The compressibility of media under extreme pressures, *Proc. Natl. Acad. Sci. U. S. A.* 30 (1944) 244–247.  
<https://doi.org/10.1073/pnas.30.9.244>.
- [44] W. Hume-Rothery, G.V. Raynor, *The structure of metals and alloys*, Institute of metals London, 1936.
- [45] J.C. Woolley, B.A. Smith, Solid Solution in  $\text{A}^{\text{III}}\text{B}^{\text{V}}$  Compounds, *Proc. Phys. Soc.* 72 (1958) 214–223. <https://doi.org/10.1088/0370->

1328/72/2/306.

- [46] M.F. Gratten, J.C. Woolley, Phase diagram and lattice parameter data for the GaAs<sub>y</sub>Sb<sub>1-y</sub> system, *J. Electron. Mater.* 2 (1973) 455–464.  
<https://doi.org/10.1007/BF02660149>.
- [47] R.E. Nahory, M.A. Pollack, W.D. Johnston Jr, R.L. Barns, Band gap versus composition and demonstration of Vegard's law for In<sub>1-x</sub>Ga<sub>x</sub>As<sub>y</sub>P<sub>1-y</sub> lattice matched to InP, *Appl. Phys. Lett.* 33 (1978) 659–661. <https://doi.org/10.1063/1.90455>.
- [48] E. Kuphal, Phase diagrams of InGaAsP, InGaAs and InP lattice-matched to (100) InP, *J. Cryst. Growth.* 67 (1984) 441–457.  
[https://doi.org/10.1016/0022-0248\(84\)90036-8](https://doi.org/10.1016/0022-0248(84)90036-8).
- [49] D. Shimura, F. Ichihashi, K. Nishitani, S. Harada, M. Kuwahara, T. Ito, M. Matsunami, S. Kimura, T. Sakai, M. Tagawa, Ultrahigh-resolution direct observation of mini-bands formed in InGaAs/AlGaAs superlattice, in: 2013 IEEE 39th Photovolt. Spec. Conf., IEEE, 2013: pp. 306–310.
- [50] H.C. Robarts, T.E. Millichamp, D.A. Lagos, J. Laverock, D. Billington, J.A. Duffy, D. O'Neill, S.R. Giblin, J.W. Taylor, G. Kontrym-Sznajd, Extreme Fermi surface smearing in a maximally disordered concentrated solid solution, *Phys. Rev. Lett.* 124 (2020) 46402.
- [51] J. Ma, H.-X. Deng, J.-W. Luo, S.-H. Wei, Origin of the failed

ensemble average rule for the band gaps of disordered nonisovalent semiconductor alloys, *Phys. Rev. B.* 90 (2014) 115201.  
<https://doi.org/10.1103/PhysRevB.90.115201>.

- [52] X. Xu, H. Jiang, Cluster expansion based configurational averaging approach to bandgaps of semiconductor alloys, *J. Chem. Phys.* 150 (2019) 034102. <https://doi.org/10.1063/1.5078399>.
- [53] A. Kyrtos, J. Glennon, A. Glasmann, M.R. O'Masta, B.-M. Nguyen, E. Bellotti, Machine-Learning-Assisted First-Principles Calculations of Strained  $\text{InAs}_{1-x}\text{Sb}_x$  Alloys for Curved Focal-Plane Arrays, *Phys. Rev. Appl.* 15 (2021) 64008.  
<https://doi.org/10.1103/PhysRevApplied.15.064008>.
- [54] R. Magri, A. Zunger, Real-space description of semiconducting band gaps in substitutional systems, *Phys. Rev. B.* 44 (1991) 8672–8684.  
<https://doi.org/10.1103/PhysRevB.44.8672>.
- [55] S. Wei, D.B. Laks, A. Zunger, Dependence of the optical properties of semiconductor alloys on the degree of long-range order, *Appl. Phys. Lett.* 62 (1993) 1937–1939. <https://doi.org/10.1063/1.109496>.
- [56] A. van de Walle, A complete representation of structure-property relationships in crystals, *Nat. Mater.* 7 (2008) 455–458.  
<https://doi.org/10.1038/nmat2200>.
- [57] B.P. Burton, S. Demers, A. van de Walle, First principles phase

- diagram calculations for the wurtzite-structure quasibinary systems SiC-AlN, SiC-GaN and SiC-InN, *J. Appl. Phys.* 110 (2011) 023507. <https://doi.org/10.1063/1.3602149>.
- [58] Y. Kumagai, Y. Soda, F. Oba, A. Seko, I. Tanaka, First-principles calculations of the phase diagrams and band gaps in CuInSe<sub>2</sub>-CuGaSe<sub>2</sub> and CuInSe<sub>2</sub>-CuAlSe<sub>2</sub> pseudobinary systems, *Phys. Rev. B.* 85 (2012) 033203. <https://doi.org/10.1103/PhysRevB.85.033203>.
- [59] J.A. Purton, N.L. Allan, M.Y. Lavrentiev, I.T. Todorov, C.L. Freeman, Computer simulation of mineral solid solutions, *Chem. Geol.* 225 (2006) 176–188. <https://doi.org/10.1016/j.chemgeo.2005.08.032>.
- [60] R. Pillarisetty, Academic and industry research progress in germanium nanodevices, *Nature.* 479 (2011) 324–328. <https://doi.org/10.1038/nature10678>.
- [61] T.F. Kuech, III-V compound semiconductors: Growth and structures, *Prog. Cryst. Growth Charact. Mater.* 62 (2016) 352–370. <https://doi.org/10.1016/j.pcrysgrow.2016.04.019>.
- [62] S. Niu, Z. Wei, X. Fang, D. Wang, X. Wang, X. Gao, R. Chen, Brief review of epitaxy and emission properties of GaSb and related semiconductors, *Crystals.* 7 (2017) 337. <https://doi.org/10.3390/cryst7110337>.
- [63] A.E. Yachmenev, S.S. Pushkarev, R.R. Reznik, R.A. Khabibullin, D.S. Ponomarev, Arsenides-and related III-V materials-based multilayered

structures for terahertz applications: Various designs and growth technology, *Prog. Cryst. Growth Charact. Mater.* (2020) 100485.  
<https://doi.org/10.1016/j.pcrysgrow.2020.100485>.

- [64] Z. Li, J. Allen, M. Allen, H.H. Tan, C. Jagadish, L. Fu, Review on III-V Semiconductor Single Nanowire-Based Room Temperature Infrared Photodetectors, *Materials (Basel)*. 13 (2020) 1400.  
<https://doi.org/10.3390/ma13061400>.
- [65] K. Ishida, Q. Ran, N. Solak, Al-P-Sb (Aluminium-Phosphorus-Antimony): Datasheet from Landolt-Börnstein - Group IV Physical Chemistry · Volume 11C1: “Non-Ferrous Metal Systems. Part 1” in *SpringerMaterials*, in: G. Effenberg, S. Ilyenko (Eds.), *Non-Ferrous Met. Syst. Part 1*, Springer-Verlag, Berlin Heidelberg, 2006: p. 154.  
[https://doi.org/10.1007/10915981\\_14](https://doi.org/10.1007/10915981_14).
- [66] R. Schmid-Fetzer, E. Fromm, M. Harmelin, H.L. Lukas, S. Maâmar, P. Perrot, Al-As-Sb (Aluminium-Arsenic-Antimony): Datasheet from Landolt-Börnstein - Group IV Physical Chemistry · Volume 11C1, in: G. Effenberg, S. Ilyenko (Eds.), *Non-Ferrous Met. Syst. Part 1*, Springer-Verlag, Berlin Heidelberg, 2006: p. 102.  
[https://doi.org/10.1007/10915981\\_8](https://doi.org/10.1007/10915981_8).
- [67] F.E.H. Hassan, A. Breidi, S. Ghemid, B. Amrani, H. Meradji, O. Pagès, First-principles study of the ternary semiconductor alloys (Ga, Al)(As, Sb), *J. Alloys Compd.* 499 (2010) 80–89.  
<https://doi.org/10.1016/j.jallcom.2010.02.121>.

- [68] N. Takenaka, M. Inoue, J. Shirafuji, Y. Inuishi, Growth of GaAs<sub>1-x</sub>Sb<sub>x</sub> crystals by steady-state liquid phase epitaxy, *J. Phys. D. Appl. Phys.* 11 (1978) L91. <https://doi.org/10.1088/0022-3727/11/5/005>.
- [69] M.F. Graton, R.G. Goodchild, L.Y. Juravel, J.C. Woolley, Miscibility gap in the GaAs<sub>y</sub>Sb<sub>1-y</sub> system, *J. Electron. Mater.* 8 (1979) 25–29. <https://doi.org/10.1007/BF02655638>.
- [70] H. Mani, A. Joullie, F. Karouta, C. Schiller, Low-temperature phase diagram of the Ga-As-Sb system and liquid-phase-epitaxial growth of lattice-matched GaAsSb on (100) InAs substrates, *J. Appl. Phys.* 59 (1986) 2728–2734. <https://doi.org/10.1063/1.336981>.
- [71] K. Ishida, T. Shumiya, T. Nomura, H. Ohtani, T. Nishizawa, Phase diagram of the Ga-As-Sb system, *J. Less Common Met.* 142 (1988) 135–144. [https://doi.org/10.1016/0022-5088\(88\)90170-1](https://doi.org/10.1016/0022-5088(88)90170-1).
- [72] E.A. Albanesi, W.R.L. Lambrecht, B. Segall, Electronic structure and equilibrium properties of Ga<sub>x</sub>Al<sub>1-x</sub>N alloys, *Phys. Rev. B.* 48 (1993) 17841–17847. <https://doi.org/10.1103/PhysRevB.48.17841>.
- [73] B.P. Burton, A. van de Walle, U. Kattner, First principles phase diagram calculations for the wurtzite-structure systems AlN–GaN, GaN–InN, and AlN–InN, *J. Appl. Phys.* 100 (2006) 113528. <https://doi.org/10.1063/1.2372309>.
- [74] Z.W. Lu, D.B. Laks, S.H. Wei, A. Zunger, First-principles simulated-annealing study of phase transitions and short-range order in

- transition-metal and semiconductor alloys, *Phys. Rev. B.* 50 (1994) 6642–6661. <https://doi.org/10.1103/PhysRevB.50.6642>.
- [75] G. Ghosh, A. van de Walle, M. Asta, First-principles calculations of the structural and thermodynamic properties of bcc, fcc and hcp solid solutions in the Al–TM (TM=Ti, Zr and Hf) systems: A comparison of cluster expansion and supercell methods, *Acta Mater.* 56 (2008) 3202–3221. <https://doi.org/10.1016/j.actamat.2008.03.006>.
- [76] J.Z. Liu, A. Zunger, Thermodynamic states and phase diagrams for bulk-incoherent, bulk-coherent, and epitaxially-coherent semiconductor alloys: Application to cubic (Ga,In)N, *Phys. Rev. B.* 77 (2008) 205201. <https://doi.org/10.1103/PhysRevB.77.205201>.
- [77] A. Silverman, A. Zunger, R. Kalish, J. Adler, Atomic-scale structure of disordered  $\text{Ga}_{1-x}\text{In}_x\text{P}$  alloys, *Phys. Rev. B.* 51 (1995) 10795–10816. <https://doi.org/10.1103/PhysRevB.51.10795>.
- [78] R. Grau-Crespo, S. Hamad, C.R.A. Catlow, N.H. De Leeuw, Symmetry-adapted configurational modelling of fractional site occupancy in solids, *J. Phys. Condens. Matter.* 19 (2007) 256201. <https://doi.org/10.1088/0953-8984/19/25/256201>.
- [79] J. Ding, J. Washburn, T. Sands, V.G. Keramidas, In/GaAs reaction: Effect of an intervening oxide layer, *Appl. Phys. Lett.* 49 (1986) 818–820. <https://doi.org/10.1063/1.97557>.
- [80] G. Kresse, J. Furthmüller, Efficiency of ab-initio total energy

calculations for metals and semiconductors using a plane-wave basis set, *Comput. Mater. Sci.* 6 (1996) 15–50. [https://doi.org/10.1016/0927-0256\(96\)00008-0](https://doi.org/10.1016/0927-0256(96)00008-0).

- [81] G. Kresse, J. Furthmüller, Efficient iterative schemes for ab initio total-energy calculations using a plane-wave basis set, *Phys. Rev. B.* 54 (1996) 11169–11186. <https://doi.org/10.1103/PhysRevB.54.11169>.
- [82] P.E. Blöchl, Projector augmented-wave method, *Phys. Rev. B.* 50 (1994) 17953. <https://doi.org/10.1103/PhysRevB.50.17953>.
- [83] G. Kresse, D. Joubert, From ultrasoft pseudopotentials to the projector augmented-wave method, *Phys. Rev. B.* 59 (1999) 1758–1775. <https://doi.org/10.1103/PhysRevB.59.1758>.
- [84] M. Chandran, Multiscale ab initio simulation of Ni-based alloys: Real-space distribution of atoms in  $\gamma + \gamma'$  phase, *Comput. Mater. Sci.* 108 (2015) 192–204. <https://doi.org/10.1016/j.commatsci.2015.06.029>.
- [85] J.P. Perdew, A. Zunger, Self-interaction correction to density-functional approximations for many-electron systems, *Phys. Rev. B.* 23 (1981) 5048–5079. <https://doi.org/10.1103/PhysRevB.23.5048>.
- [86] S.B. Zhang, M.L. Cohen, High-pressure phases of III-V zinc-blende semiconductors, *Phys. Rev. B.* 35 (1987) 7604–7610. <https://doi.org/10.1103/PhysRevB.35.7604>.
- [87] G.A. Antypas, Liquid-Phase Epitaxy of  $\text{In}_x\text{Ga}_{1-x}\text{As}$ , *J. Electrochem. Soc.* 117 (1970) 1393–1397. <https://doi.org/10.1149/1.2407329>.

- [88] C.W. Snyder, B.G. Orr, D. Kessler, L.M. Sander, Effect of strain on surface morphology in highly strained InGaAs films, *Phys. Rev. Lett.* 66 (1991) 3032–3035. <https://doi.org/10.1103/PhysRevLett.66.3032>.
- [89] D. Leonard, M. Krishnamurthy, Cm. Reaves, S.P. DenBaars, P.M. Petroff, Direct formation of quantum-sized dots from uniform coherent islands of InGaAs on GaAs surfaces, *Appl. Phys. Lett.* 63 (1993) 3203–3205. <https://doi.org/10.1063/1.110199>.
- [90] M. Borg, L. Gignac, J. Bruley, A. Malmgren, S. Sant, C. Convertino, M.D. Rossell, M. Sousa, C. Breslin, H. Riel, Facet-selective group-III incorporation in InGaAs template assisted selective epitaxy, *Nanotechnology.* 30 (2018) 84004. <https://doi.org/10.1088/1361-6528/aaf547>.
- [91] A. Bucamp, C. Coinon, J.-L. Codron, D. Troadec, X. Wallart, L. Desplanque, Buffer free InGaAs quantum well and in-plane nanostructures on InP grown by atomic hydrogen assisted MBE, *J. Cryst. Growth.* 512 (2019) 11–15. <https://doi.org/10.1016/j.jcrysgro.2019.01.033>.
- [92] S.T. Murphy, A. Chroneos, R.W. Grimes, C. Jiang, U. Schwingenschlögl, Phase stability and the arsenic vacancy defect in  $\text{In}_x\text{Ga}_{1-x}\text{As}$ , *Phys. Rev. B.* 84 (2011) 184108. <https://doi.org/10.1103/PhysRevB.84.184108>.
- [93] K. Onabe, Unstable regions in III–V quaternary solid solutions

composition plane calculated with strictly regular solution approximation, *Jpn. J. Appl. Phys.* 21 (1982) L323–L325.  
<https://doi.org/10.1143/JJAP.21.L323>.

- [94] J.-Y. Shen, C. Chatillon, I. Ansara, A. Watson, B. Rugg, T. Chart, Optimisation of the thermodynamic and phase diagram data in the ternary As-Ga-In system, *Calphad.* 19 (1995) 215–226.  
[https://doi.org/10.1016/0364-5916\(95\)00022-7](https://doi.org/10.1016/0364-5916(95)00022-7).
- [95] H. Nakamura, M. Sorai, M. Ishikawa, H. Kato, S. Yoda, K. Kinoshita, Simple thermodynamic equations to calculate driving force for  $\text{In}_x\text{Ga}_{1-x}\text{As}$  crystals which grow from their own melt, National Space Development Agency of Japan, 1999.  
<https://repository.exst.jaxa.jp/dspace/handle/a-is/46726>.
- [96] K. Ishida, H. Tokunaga, H. Ohtani, T. Nishizawa, Data base for calculating phase diagrams of III–V alloy semiconductors, *J. Cryst. Growth.* 98 (1989) 140–147. [https://doi.org/10.1016/0022-0248\(89\)90194-2](https://doi.org/10.1016/0022-0248(89)90194-2).
- [97] I. V Pentin, J.C. Schön, M. Jansen, Ab initio prediction of low-temperature phase diagrams in the Al–Ga–In–As system,  $\text{MAs–M'As}$  ( $\text{M, M' = Al, Ga or In}$ ) and  $\text{AlAs–GaAs–InAs}$ , via the global study of energy landscapes, *Phys. Chem. Chem. Phys.* 12 (2010) 8491–8499.  
<https://doi.org/10.1039/c004040c>.
- [98] K. Ishida, T. Nomura, H. Tokunaga, H. Ohtani, T. Nishizawa,

Miscibility gaps in the GaP-InP, GaP-GaSb, InP-InSn and InAs-InSb systems, *J. Less Common Met.* 155 (1989) 193–206.

[https://doi.org/10.1016/0022-5088\(89\)90228-2](https://doi.org/10.1016/0022-5088(89)90228-2).

- [99] A.S. Brown, P. Bhattacharya, J. Singh, P. Zaman, S. Sen, F. Turco, Dependence of  $\text{Al}_{0.48}\text{In}_{0.52}\text{As}$  Schottky diode properties on molecular beam epitaxial growth temperature, *Appl. Phys. Lett.* 68 (1996) 220–222. <https://doi.org/10.1063/1.116466>.
- [100] J.B. Li, W. Zhang, C. Li, Z. Du, Assessment of phase diagram and thermodynamic properties of the Al-Ga-Sb system, *J. Phase Equilibria.* 20 (1999) 316. <https://doi.org/10.1361/105497199770335839>.
- [101] K. Mukherjee, A.G. Norman, A.J. Akey, T. Buonassisi, E.A. Fitzgerald, Spontaneous lateral phase separation of AlInP during thin film growth and its effect on luminescence, *J. Appl. Phys.* 118 (2015) 115306. <https://doi.org/10.1063/1.4930990>.
- [102] L.M. Foster, A Lattice Parameter Criterion for Miscibility Gaps in the III – V and II – VI Pseudobinary Solid Solutions, *J. Electrochem. Soc.* 121 (1974) 1662–1665. <https://doi.org/10.1149/1.2401764>.
- [103] A. Franceschetti, S. V Dudiy, S. V Barabash, A. Zunger, J. Xu, M. Van Schilfgaarde, First-principles combinatorial design of transition temperatures in multicomponent systems: the case of Mn in GaAs, *Phys. Rev. Lett.* 97 (2006) 47202. <https://doi.org/10.1103/PhysRevLett.97.047202>.

- [104] A. Franceschetti, A. Zunger, The inverse band-structure problem of finding an atomic configuration with given electronic properties, *Nature*. 402 (1999) 60–63. <https://doi.org/10.1038/46995>.
- [105] Y. Wang, L. Wang, X. Zhang, X. Liang, Y. Feng, W. Feng, Two-dimensional nanomaterials with engineered bandgap: Synthesis, properties, applications, *Nano Today*. 37 (2021) 101059. <https://doi.org/10.1016/j.nantod.2020.101059>.
- [106] R.E. Nahory, M.A. Pollack, J.C. DeWinter, K.M. Williams, Growth and properties of liquid-phase epitaxial  $\text{GaAs}_{1-x}\text{Sb}_x$ , *J. Appl. Phys.* 48 (1977) 1607–1614. <https://doi.org/10.1063/1.323841>.
- [107] J. Heyd, G.E. Scuseria, M. Ernzerhof, Hybrid functionals based on a screened Coulomb potential, *J. Chem. Phys.* 118 (2003) 8207–8215. <https://doi.org/10.1063/1.1564060>.
- [108] Y.-S. Kim, M. Marsman, G. Kresse, F. Tran, P. Blaha, Towards efficient band structure and effective mass calculations for III-V direct band-gap semiconductors, *Phys. Rev. B*. 82 (2010) 205212. <https://doi.org/10.1103/PhysRevB.82.205212>.
- [109] M. Wang, G.-B. Liu, H. Guo, Y. Yao, An efficient method for hybrid density functional calculation with spin–orbit coupling, *Comput. Phys. Commun.* 224 (2018) 90–97. <https://doi.org/10.1016/j.cpc.2017.11.010>.
- [110] F. Viñes, O. Lamiel-García, K. Chul Ko, J. Yong Lee, F. Illas,

Systematic study of the effect of HSE functional internal parameters on the electronic structure and band gap of a representative set of metal oxides, *J. Comput. Chem.* 38 (2017) 781–789.

<https://doi.org/10.1002/jcc.24744>.

[111] Y. Iwamura, T. Takeuchi, N. Watanabe, Temperature dependence of solid-vapor compositional relation in epitaxial growth of GaAs<sub>x</sub>Sb<sub>1-x</sub> by low-pressure metalorganic chemical vapor deposition, *J. Cryst. Growth.* 145 (1994) 82–86. [https://doi.org/10.1016/0022-0248\(94\)91032-4](https://doi.org/10.1016/0022-0248(94)91032-4).

[112] K.D. Moiseev, V. V Romanov, T.I. Voronina, T.S. Lagunova, M.P. Mikhailova, Y.P. Yakovlev, Type II GaAs<sub>x</sub>Sb<sub>1-x</sub>/InAs (x), *J. Cryst. Growth.* 310 (2008) 4846–4849. <https://doi.org/10.1016/j.jcrysgro.2008.07.023>.

[113] H. Xie, H. Liu, S. Chen, T. Han, S. Wang, Electrical performance of InAs/GaAs<sub>0.1</sub>Sb<sub>0.9</sub> heterostructure junctionless TFET with dual-material gate and Gaussian-doped source, *Semicond. Sci. Technol.* 35 (2020) 095004. <https://doi.org/10.1088/1361-6641/ab9b01>.

[114] J.M. Cowley, X-Ray Measurement of Order in Single Crystals of Cu<sub>3</sub>Au, *J. Appl. Phys.* 21 (1950) 24–30. <https://doi.org/10.1063/1.1699415>.

[115] K. Pearson, Notes on Regression and Inheritance in the Case of Two Parents, in: *Proc. R. Soc. London, Royal Society (Great Britain)*,

London, 1895: pp. 240–242.

- [116] S.-H. Wei, S.B. Zhang, A. Zunger, Band structure and stability of zinc-blende-based semiconductor polytypes, *Phys. Rev. B.* 59 (1999) R2478. <https://doi.org/10.1103/PhysRevB.59.R2478>.
- [117] M.B. Thomas, W.M. Coderre, J.C. Woolley, Energy gap variation in  $\text{GaAs}_x\text{Sb}_{1-x}$  alloys, *Phys. Status Solidi.* 2 (1970) K141–K143. <https://doi.org/10.1002/pssa.19700020332>.
- [118] R. Lukic-Zrnica, B.P. Gorman, R.J. Cottier, T.D. Golding, C.L. Littler, A.G. Norman, Temperature dependence of the band gap of GaAsSb epilayers, *J. Appl. Phys.* 92 (2002) 6939–6941. <https://doi.org/10.1063/1.1517746>.
- [119] H.R. Jen, M.J. Cherng, G.B. Stringfellow, Ordered structures in  $\text{GaAs}_{0.5}\text{Sb}_{0.5}$  alloys grown by organometallic vapor phase epitaxy, *Appl. Phys. Lett.* 48 (1986) 1603–1605. <https://doi.org/10.1063/1.96830>.
- [120] Y. Ihm, N. Otsuka, J. Klem, H. Morkoc, Ordering in  $\text{GaAs}_{1-x}\text{Sb}_x$  grown by molecular beam epitaxy, *Appl. Phys. Lett.* 51 (1987) 2013–2015. <https://doi.org/10.1063/1.98277>.
- [121] G.B. Stringfellow, Ordered structures and metastable alloys grown by OMVPE, *J. Cryst. Growth.* 98 (1989) 108–117. [https://doi.org/10.1016/0022-0248\(89\)90191-7](https://doi.org/10.1016/0022-0248(89)90191-7).
- [122] K. Yim, Y. Yong, J. Lee, K. Lee, H.-H. Nahm, J. Yoo, C. Lee, C.S.

- Hwang, S. Han, Novel high- $\kappa$  dielectrics for next-generation electronic devices screened by automated ab initio calculations, *NPG Asia Mater.* 7 (2015) e190. <https://doi.org/10.1038/am.2015.57>.
- [123] G.A. Slack, S.B. Austerman, Thermal Conductivity of BeO Single Crystals, *J. Appl. Phys.* 42 (1971) 4713–4717. <https://doi.org/10.1063/1.1659844>.
- [124] H.S. Shin, J.H. Yum, D.W. Johnson, H.R. Harris, T.W. Hudnall, J. Oh, P. Kirsch, W.-E. Wang, C.W. Bielawski, S.K. Banerjee, J.C. Lee, H.D. Lee, Low interface defect density of atomic layer deposition BeO with self-cleaning reaction for InGaAs metal oxide semiconductor field effect transistors, *Appl. Phys. Lett.* 103 (2013) 223504. <https://doi.org/10.1063/1.4833815>.
- [125] S.M. Lee, J.H. Yum, S. Yoon, E.S. Larsen, W.C. Lee, S.K. Kim, S. Shervin, W. Wang, J.-H. Ryou, C.W. Bielawski, J. Oh, Atomic-Layer Deposition of Single-Crystalline BeO Epitaxially Grown on GaN Substrates, *ACS Appl. Mater. Interfaces.* 9 (2017) 41973–41979. <https://doi.org/10.1021/acsami.7b13487>.
- [126] M.B. Sahariah, S. Ghosh, Dynamical stability and phase transition of BeO under pressure, *J. Appl. Phys.* 107 (2010) 83520. <https://doi.org/10.1063/1.3359706>.
- [127] Z.-C. Guo, F. Luo, G.-F. Ji, L.-C. Cai, Y. Cheng, Phase transition, dynamical and electronic properties of BeO: First-principles

- investigations, *Phys. B Condens. Matter.* 438 (2014) 60–64.  
<https://doi.org/10.1016/j.physb.2014.01.008>.
- [128] K.-L. Wang, S.-P. Gao, Phonon dispersions, band structures, and dielectric functions of BeO and BeS polymorphs, *J. Phys. Chem. Solids.* 118 (2018) 242–247.  
<https://doi.org/10.1016/j.jpcs.2018.03.013>.
- [129] Y. Mori, T. Ikai, K. Takarabe, A.L. Ruoff, The phase transition of BeO under high pressure, *Phot. Fact. Act. Rep.* (2003) 215.
- [130] Y. Mori, N. Niiya, K. Ukegawa, T. Mizuno, K. Takarabe, A.L. Ruoff, High-pressure X-ray structural study of BeO and ZnO to 200 GPa, *Phys. Status Solidi.* 241 (2004) 3198–3202.  
<https://doi.org/10.1002/pssb.200405247>.
- [131] U.D. Wdowik, Structural stability and thermal properties of BeO from the quasiharmonic approximation, *J. Phys. Condens. Matter.* 22 (2010) 45404. <https://doi.org/10.1088/0953-8984/22/4/045404>.
- [132] W.C. Lee, S. Kim, E.S. Larsen, J.-H. Choi, S.-H. Baek, M. Lee, D.-Y. Cho, H.-K. Lee, C.S. Hwang, C.W. Bielawski, S.K. Kim, Atomic engineering of metastable BeO<sub>6</sub> octahedra in a rocksalt framework, *Appl. Surf. Sci.* 501 (2020) 144280.  
<https://doi.org/10.1016/j.apsusc.2019.144280>.
- [133] S.-W. Zheng, G.-H. Fan, S.-T. Li, T. Zhang, C. Su, Energy band properties and phase stability of Be<sub>1-x</sub>Mg<sub>x</sub>O alloy, *Acta Phys. Sin.* 61

(2012) 237101. <https://doi.org/10.7498/aps.61.237101>.

- [134] L. Su, Y. Zhu, D. Yong, M. Chen, X. Ji, Y. Su, X. Gui, B. Pan, R. Xiang, Z. Tang, Wide range bandgap modulation based on ZnO-based alloys and fabrication of solar blind UV detectors with high rejection ratio, *ACS Appl. Mater. Interfaces*. 6 (2014) 14152–14158. <https://doi.org/10.1021/am503427u>.
- [135] L. Pauling, The principles determining the structure of complex ionic crystals, *J. Am. Chem. Soc.* 51 (1929) 1010–1026. <https://doi.org/10.1021/ja01379a006>.
- [136] D.M. Roessler, W.C. Walker, E. Loh, Electronic spectrum of crystalline beryllium oxide, *J. Phys. Chem. Solids*. 30 (1969) 157–167. [https://doi.org/10.1016/0022-3697\(69\)90348-5](https://doi.org/10.1016/0022-3697(69)90348-5).
- [137] O.E. Taurian, M. Springborg, N.E. Christensen, Self-consistent electronic structures of MgO and SrO, *Solid State Commun.* 55 (1985) 351–355. [https://doi.org/10.1016/0038-1098\(85\)90622-2](https://doi.org/10.1016/0038-1098(85)90622-2).
- [138] S.M. Lee, Y. Jang, J. Jung, J.H. Yum, E.S. Larsen, S.Y. Lee, H. Seo, C.W. Bielawski, H.-D. Lee, J. Oh, Crystalline BeO Grown on 4H-SiC via Atomic Layer Deposition: Band Alignment and Interface Defects, *ACS Appl. Electron. Mater.* 1 (2019) 617–624. <https://doi.org/10.1021/acsaelm.9b00098>.

## ABSTRACT IN KOREAN

---

유사이성분계는 원하는 물성을 얻기 위해 널리 사용되어 왔다. 유사이성분계가 고용체 상태일 때는 대개 조성을 조절함으로써 유사이성분계의 물성을 조정해왔다. 최근에는 원자배열을 조절하는 방법들이 발전하면서 배열에 따라 크게 바뀌는 에너지, 밴드갭, 유전율과 같은 특성들을 배열의 관점에서 조사해볼 필요성이 커지고 있다. 이 논문에서는 트랜지스터에 사용될 후보 물질들인 Ga(As,Sb), (In,Ga)As, (Be,Mg)O 의 배열과 조성에 의존하는 물성에 대하여 이론적으로 연구하였다.

그러나 유사이성분계가 가질 수 있는 엄청난 수의 배열들은 유사이성분계, 특히 고용체 형태의 유사이성분계를 이론적으로 연구하는 것을 어렵게 만드는데, 이를 배열 문제라고 부른다. 배열 문제를 해결하고 고용체의 물성을 계산하기 위해 효율적이고 정확한 계산 방법을 제시하였다. 이는 (1) 밀도범함수이론(DFT)를 활용하여 많은 배열들의 에너지를 포함한 물성들을 계산하고, (2) DFT 데이터를 바탕으로 클러스터전개모형을 세워 DFT 만으로는 계산하기 힘든 막대한 배열 및 조성 공간을 탐색할 수 있게 된 후, (3) 전체 시스템을 많은 수의 미시상태들로 다룰 수 있는 통계열역학을 활용하여 평균 물성을 구하는 방법이다. 통계열역학 부분에서는 조성변동을 허용하며 연속된 조성을 다룰 수 있게

해주어 더 현실적인 모사를 할 수 있는 대정준 앙상블을 사용하였다.

제시한 방법이 새로운 물질에 적용할 수 있음을 확인하기 위해 Ga(As,Sb)와 (In,Ga)As 의 상태도와 Ga(As,Sb)의 밴드갭을 실험 문헌들과 비교하여 방법론을 검증하였다. 그 과정에서 대정준 앙상블을 사용할 때는 국부 조성 변동에 의해 발생하는 미시상태 간의 격자불일치로 인한 국부 변형이 고려하여야만 실제 나타나는 현상을 모사할 수 있음을 찾아내고 수학적으로 증명하였다. Ga(As,Sb)의 배열들에 대한 계산을 통해 조성과 배열을 모두 조절할 시 조성만을 조절하였을 때보다 더 넓은 밴드갭을 얻을 수 있다는 사실을 확인하였다. 또한, Ga(As,Sb)에 밴드갭과 에너지 사이의 역관계가 있음을 확인하였고, 문헌들에 나와있는 유효 클러스터 상호작용 계수(ECI)로부터 밴드갭과 에너지 사이의 역관계가 다른 물질에서도 나타날 것임을 예측하였다.

고유전율 물질로 사용될 후보 물질인 (Be,Mg)O 에 대해서는 고유전율 물질에 요구되는 높은 유전율과 높은 밴드갭을 얻기 위하여 계산을 수행하였다. 작은 셀에 대한 DFT 계산으로 (Be,Mg)O 는 Be 원자가 암염구조에서 제자리를 약간 벗어나서 수정된 암염구조가 되면 암염구조보다 더 안정함을 확인하였다. 많은 배열들에 대한 DFT 계산을 통해 수정된 암염구조인 (Be,Mg)O 의 유전율은 배열에 따라 크게 바뀌는 반면 밴드갭은

배열에 관계없이 높은 것을 확인하였다. 따라서 높은 유전율을 갖는 배열을 찾는 방식으로 연구를 진행하였고, 그 결과 ALD 를 이용해 증착할 수 있는 초격자 구조를 갖는 배열들이 300 K 이상의 온도에서 높은 유전율을 가지게 될 것임을 확인하였고, 이는 긴 수직 방향으로의 Be-O 결합길이를 통하여 설명할 수 있었다.

이번 학위 논문에서는 계산하기 어렵다고 알려진 유사이성분계를 배열을 관점에서 연구하였다. 이를 위해 개발한 유사이성분계 시뮬레이션하기 위한 방법은 다른 유사이성분계의 물성을 예측하고 조절하는데 많은 도움이 될 수 있을 것이며, 기존에는 유사이성분계의 물성을 조성으로만 조정하였지만 배열과 조성을 모두 조절한다면 얻을 수 있는 물성의 범위가 훨씬 넓어짐을 확인한 것은 배열 조절을 통한 물성 연구에 중요한 밑거름이 될 것이다.